



UNIVERSITY OF LEEDS

Numerical Simulations of Dusty Colliding Wind Binaries



Joseph Eatson
University of Leeds
School of Physics and Astronomy

Submitted in accordance with the requirements for the degree of

Doctor of Philosophy

February, 2022

To my Mum, without her help these past 26 years there's no way I would have
gotten this far.

I'll pay you back I promise.

*“Space is **big**. Really big. You just won’t believe how vastly, hugely, mind-bogglingly big it is. I mean, you may think it’s a long way down the road to the chemist’s, but that’s just peanuts to space.”*

DOUGLAS ADAMS
The Hitchhiker’s Guide to the Galaxy

*“I am aware that quoting Douglas Adams in
an astrophysics thesis is an absolutely
enormous cliché, but I want to do it anyway.”*

ME
This Thesis

Acknowledgements

If you're reading this ahead of time and wondering where you are, don't worry, I'm getting to you, just writing the thesis first!

I suppose a good place to start when thanking people in a thesis is to start with family. To my mum, when I asked you to for help funding my doctoral degree, you said yes, instantly, and without hesitation, considering all you have done and sacrificed for me throughout my life, your agreeing to help was another act of kindness that I can barely repay (trust me, I've done the maths). You've been there for me, every step of the way, I could not ask for a more wonderful mum, and I hope I can make you proud.

I also owe a debt to my supervisor, Dr. Julian Pittard, you've gone above and beyond when it came to my supervision, you've solved bugs, found mistakes and gotten me out of a jam more times in this project than I can count. I'm still amazed how you can rattle off a paper or three from memory when I've come into your office asking questions about a very specific part of my work. Honestly, how do you do that? It's very impressive.

No good thesis¹ wouldn't be complete without a commitment to the authors friends. I first met some of you on the literal first day of my undergraduate degree, it's really quite incredible how you've all tolerated my nonsense for so long. From essentially forcing my way into Rob's house so I could cook some disastrous fried chicken, to playing *Super Smash Bros.* all night long on its release day, to watching trashy movies over the internet at the height of a global pandemic, these are moments I'll treasure for the rest of my life. In particular, those who are still in Leeds, Rob, Matt, Kelsie, Alex and Sam; as well as those who aren't, Martin, Caz, Andy, and Devon. Thank you all, for filling my life with joy this past decade. To my partner Pruthvi, I cannot stress how unlikely it is that the two of us even met - two people finding and falling for each other on the more esoteric circles of the internet is like two particles colliding in the tenuous interstellar medium, if you'll excuse the extremely trite metaphor. You've been loving, kind, helpful, and the most wonderful partner anyone could ask for. I truly am blessed to know you and love you.

I would also like to thank the fantastic team at Leeds' ARC High Performance Computing department, considering the bulk of this work involves many 3D numerical simulations my use of ARC 4's compute nodes can be described as somewhere

¹Though the quality of this one is debatable.

from “excessive” to “taking the piss”. I also apologise for running my earlier simulations on the login nodes for multiple days, I swear it was an accident.

I would also like to thank two figures from my formative years for inspiring me. The first is my 9th year Physics teacher, Isobel Why, who re-kindled my interest in the field, she was the finest teacher I ever had, turning me from an underachieving student to a keen and committed aspiring physicist. She truly had faith in all of her students, and pushed them far beyond what they thought themselves capable of. Whilst she left teaching shortly after that year, I will never forget her impact on my life and my work. Another is quite indirect, but still important, I would be amiss to thank Winchell “Nyrath” Chung, curator of the website [Atomic Rockets](#)¹. Winchell’s work is perhaps one of the most complete and exhaustive archive of real life and fictional rocketry and space exploration resources - whilst I haven’t called on his work much during my career in astrophysics, I pored over this website when I was younger (perhaps reading it more thoroughly than any of my course textbooks). It was fascinating, insightful and inspiring not only to me, but thousands of readers; the number of projects, from hard SFF novellas to honest-to-goodness research proposals hinge on his tireless efforts to catalogue humankind’s exploration of space in both reality and fiction. I learned of his cancer diagnosis whilst writing this thesis, and it cut me to my core, without his work I don’t think I would have turned a fascination with space into a lifelong passion. Thank you so much, both of you, you may not realise it, you may not ever read this, but you changed my life.

Finally, I would like to thank Leandro Panizzon and his wife, Margarita, though Methylphenidate was originally synthesised by him to treat her low blood pressure, it also works quite well for dragging my attention-deficit disorder riddled brain through this PhD.

¹http://projectrho.com/public_html/rocket/

Abstract

CONTENTS

1	Introduction & Motivation	1
1.1	Dust Formation in Colliding Wind Binary Systems	2
1.2	Motivation	2
1.3	Thesis Structure	2
2	Background	3
2.1	Early-Type Stars	4
2.1.1	Formation	5
2.1.2	The p-p & CNO fusion cycles	6
2.1.3	Stellar winds	7
2.1.4	Evolved main sequence stars	13
2.1.5	Wolf-Rayet stars	14
2.2	Interstellar Dust	16
2.2.1	Dust composition	20
2.2.2	Radiation processes in interstellar dust	20
2.2.3	The importance of interstellar dust	21
2.3	Colliding Wind Binary Systems	22
2.3.1	History of CWB observation	22
2.3.2	The Wind Collision Region	23
2.3.3	Cooling in the WCR	27
2.3.4	Dust formation in CWB systems	33
2.3.5	Important WCd systems	36
2.3.6	WR+WR systems	40

CONTENTS

3 Methodology & Numerical Simulation	43
3.1 The History & Mathematics of Numerical Simulations	44
3.2 The Purpose of Numerical Simulations	46
3.3 Computational Hydrodynamics	48
3.3.1 Comparison of hydrodynamical methods	48
3.3.2 The MG hydrodynamical code	48
3.4 The Athena++ hydrodynamical code	49
3.5 Mesh Refinement	52
3.6 Datatypes & visualisation	54
3.7 Simulating CWB systems	55
3.7.1 Assumptions	55
3.7.2 Wind propagation & refinement	56
3.7.3 Cooling in numerical simulations	57
3.7.4 Model implementation	66
3.8 The BODMAS Adverted Scalar Dust Model	71
3.8.1 BODMAS features	71
3.8.2 Implementation	71
3.8.3 Contemporary dust Models	72
3.8.4 Future dust models	73
4 An exploration of dust formation within WCd systems	77
4.1 Introduction	78
4.2 Methodology	81
4.2.1 Gas and dust cooling	84
4.2.2 Numerical modelling of dust through advected scalars	87
4.3 Model Parameters	90
4.3.1 Cooling mechanisms	91
4.3.2 Wind momentum ratio	91
4.3.3 Separation distance	92
4.3.4 Data collection	93
4.4 Results	94
4.4.1 Mass loss rate variation	97
4.4.2 Terminal velocity variation	101
4.4.3 Separation variation	105

CONTENTS

4.5	Conclusions	107
4.5.1	Wind mixing within the WCR	107
4.6	Summary	107
4.7	Acknowledgements	108
5	Exploring dust formation in WR140	109
5.1	Introduction	110
5.2	Methodology	112
5.2.1	Radiative cooling	114
5.2.2	Dust model	115
5.3	System parameters	118
5.3.1	WR140 parameters	120
5.3.2	Simulation parameters	121
5.3.3	Data collection	122
5.4	Results and Conclusions	124
5.4.1	Instabilities	126
5.4.2	Influence of varying wind velocity on dust production	128
5.5	Summary	129
5.6	Acknowledgements	132
6	Final Notes and Conclusions	133
6.1	Conclusions	134
6.1.1	Causes of dust formation in WCd systems	134
6.1.2	The role of eccentricity in dust formation	134
6.2	Future Study	134
6.2.1	More complex models	134
6.2.2	Further simulations of observed systems	134
6.2.3	Radiative transfer	134
6.2.4	WR+WR systems	134
6.2.5	Next generation telescopes	134
6.3	Other Observations	134
6.3.1	<i>How I Learned to Stop Worrying and Love Numerics</i>	134
6.3.2	Join the physics department, see the world	134
6.3.3	Paul Erdős was probably onto something	134

CONTENTS

6.3.4	Carinae Strain: PhD research in a time of pandemic	134
6.3.5	WR 104 as a local GRB candidate	134
6.4	Research software acknowledgements	134
A	Astrophysical Shocks	137
B	Software Carpentry	139
B.1	Amdahl’s Law	140
B.2	Version Control	140
References		141

LIST OF FIGURES

2.1	Reaction rates at the center of the sun	8
2.2	ρ_w comparison of main sequence winds	10
2.3	Planck's law radiance comparison with resonance lines	11
2.4	Radiative line driving velocity and density profile	13
2.5	<i>M1-67 nebula around WR 124 (Marchenko et al., 2010)</i>	15
2.6	Grain lifetime comparison	18
2.7	<i>A diagram of the Wind Collision Region (Eichler & Usov, 1993)</i>	24
2.8	Comparison of wind momentum ratio, η , on WCR struture	25
2.9	Wind shock fraction, as a function of η	27
2.10	WC & solar abundance plasma cooling curves	28
2.11	Dust cooling vs. plasma cooling	29
2.12	H_{el} and H_{coll} comparison	32
2.13	L' photometry of episodic dust making stars	35
2.14	<i>Multiwavelength image of WR98a (Monnier et al., 2007)</i>	36
2.15	<i>Spiral structure of WR104 (Soulain et al., 2018)</i>	38
2.16	<i>VLT image of Apep (Callingham et al., 2019)</i>	41
3.1	Initial conditions of a Riemann problem	44
3.2	Adaptive mesh refinement comparison	52
3.3	Comparison of dust and plasma cooling rates in post-shock environment	60
3.4	h_e integration accuracy comparison	61
3.5	Dust lookup table methods comparison	63
3.6	Electron transparency method accuracy - h_e	64
3.7	Electron transparency method accuracy - H_{el}/H_{coll}	65

LIST OF FIGURES

3.8	Electron transparency method accuracy - Λ_d	65
3.9	Ionisation fraction for OB and WC stars	66
3.10	Cooling sub-step method evolution comparison	68
3.11	Cooling sub-step method accuracy comparison	70
3.12	<i>Radiative transfer images of WR98a (Hendrix et al., 2016)</i>	75
4.1	Static mesh refinement example	83
4.2	WR and OB $\Lambda(T)$ cooling curves	85
4.3	OB and WR electron-ion ratios	86
4.4	Comparison of electron transparency methods.	88
4.5	Comparison of dust formation rates with cooling methods	95
4.6	Comparison of dust and plasma cooling rates in post-shock environment	95
4.7	Instabilities due to cooling	96
4.8	Density comparison of simulations with differing radiative processes	97
4.9	Temperature comparison of simulations with differing radiative processes	97
4.10	Wind mixing due to radiative methods	98
4.11	<code>Baseline</code> simulation z , full extent	98
4.12	Dust production rate for simulations varying mass loss rate	99
4.13	Comparison of the dust production rate for simulations varying the wind terminal velocity	100
4.14	Dust density comparison of terminal velocity varying systems	102
4.15	OB terminal velocity wind dust comparison	103
4.16	Wind colour comparison of $\eta = 0.04$ winds	104
4.17	Comparison of dust density in simulations with strong secondary wind	104
4.18	Dust formation rate versus binary separation distance	105
4.19	A comparison of the structures of simulations varying d_{sep}	106
5.1	Simulation orbital trajectories of WR140 WC7 and O5 stars	122
5.2	Numerical grid of the WR140 system simulation, static mesh refinement was used to increase the resolution around the orbital path from $0.95 \leq \Phi \leq 1.10$. The orbital path of both stars are overlaid onto this numerical grid. While the stars in the system can be within cells that are not fully refined, if there is insufficient resolution the stars begin to break down. As such the stars are typically in the 3 rd or 4 th level.	123

LIST OF FIGURES

- 5.3 A graph of the dust production rate in the WCR over the orbital phase $0.95 \leq \Phi \leq 1.10$. The dust production rate sharply increases as the stars pass their closest approach. Afterwards, the dust production rate begins to falter and slow, due to weaker wind collision effects via the separation distance and radial velocity. 124
- 5.4 A graph of the overall dust mass in the simulation of WR140 over the orbital phase $0.95 \leq \Phi \leq 1.10$. The amount of dust quickly reduces after periastron due to a decreased dust formation rate (Fig. 5.3), as well as dust advecting off of the numerical grid. 125
- 5.5 Gas density in a simulation of the WR140 system shortly before, during, and shortly after periastron. The simulation becomes rapidly dominated by instabilities a short while after periastron. However, these instabilities persist despite the system behaving adiabatically at a similar orbital separation distance prior to periastron. This suggests that the radiative behaviour of the post-shock WCR is due to multiple factors, other than dust at varying d_{sep} 126
- 5.6 Dust density in a simulation of the WR140 system shortly before, during, and shortly after periastron. Dust formation occurs as a direct result of the formation of thermal and KH instabilities in the post-shock WCR. 127
- 5.7 Wind “colour” in a simulation of the WR140 system shortly before, during, and shortly after periastron. With 1 representing a pure WR wind and 0 representing a pure OB wind. We find that the wind undergoes more mixing during and after periastron. 127
- 5.8 Radial velocity 130
- 5.9 Graph of the wind velocity of the WC7 and O4-5 stars in the WR140 system as a function of distance from the stellar surface due to radiative line driving. The dashed lines represent the distance to the WCR at periastron for each star. During periastron passage the WC7 wind is travelling at approximately its terminal velocity before collision, while the O4-5 companions wind is travelling at $\sim 84\%$ of terminal velocity before coming into contact with the WCR. CAK parameters were estimated to be $k = 0.37$, $\alpha = 0.60$ for the O4-5 star and $k = 0.48$, $\alpha = 0.57$ for the WC7 star. 131

LIST OF FIGURES

LIST OF TABLES

2.1	Comparison of fusion process reaction rates	6
2.2	Stellar wind comparison	9
2.3	Cooling processes at various temperature ranges	27
2.4	Numer of confirmed WCd systems	33
2.5	Wind properties of systems considered for simulation	36
2.6	Orbital properties of systems considered for simulation	36
3.1	Time elapsed	50
3.2	Dust cooling calculation comparison	64
3.3	Cooling method accuracy comparison	69
3.4	Cooling method performance comparison	70
4.1	Abundances by mass used for OB and WR stars	84
4.2	Wind properties of the baseline system.	91
4.3	Baseline system orbital properties.	91
4.4	Cooling series simulation parameters.	91
4.5	Terminal velocity series wind parameters	92
4.6	Parameters of simulations varying the separation distance, d_{sep} , between the stars.	93
4.7	Average rate of dust production for the set of different radiative simulations. $\dot{M}_{\text{d},\text{max}}$ is the maximum expected dust formation rate (Eq. 4.20).	99
4.8	Average rate of dust production for the mass loss rate simulation set.	100
4.9	Average rates of dust production for the terminal velocity simulation set.	103
4.10	Average rates of dust production for the separation distance simulation set. The stellar parameters are the same as in the <code>baseline</code> model, which has a $d_{\text{sep}} = 4.0 \text{ AU}$	106

LIST OF TABLES

5.1	Number of confirmed WCd systems	111
5.2	Grain critical energy	118
5.3	WR140 system parameters	120
5.4	Abundances by mass used for OB and WR stars	120
5.5	Advect ed scalar yields from WR140 simulation	124

Abbreviations

List of common abbreviations, if an abbreviation is important enough to warrant a section in this thesis, the section will be referenced.

BODMAS	Binary Orbit Dust Model with Accretion and Sputtering	Section 3.8
CAK	Castor, Abbott & Klein (1975) theory & Section 2.1.3	
CWB	Colliding Wind Binary	Section 2.1
GMC	Giant Molecular Cloud	Section 2.1
ISM	Interstellar Medium	Section 2.1
KH	Kelvin-Helmholtz	2.1
LBV	Luminous Blue Variable	Section 2.1
OB	O or B type star	Section 2.1
RSG	Red Supergiant	Section 2.1
WC	WR Carbon Phase	Section 2.1.5
WCd	Dust forming WC star	Section 2.3.4
WCR	Wind Collision Region	Section 2.3.2
WN	WR Nitrogen Phase	Section 2.1.5
WO	WR Oxygen Phase	Section 2.1.5
WR	Wolf-Rayet	Section 2.1.5
JIT	Just In Time	Section 3.6

Common Symbols

List of common symbols, if symbol requires a derivation, the appropriate equation within this thesis will be referenced. If the symbol is a unit, the value in CGS units will be provided instead.

a	Grain radius	Section 2.2
C	Courant-Friedrichs-Lowy condition	
f	Wind shock fraction	Eq. 2.18
h_e	Electron transparency	Section 2.3.3
H_{coll}	Grain heating rate due to ions	
H_{el}	Grain heating rate due to electrons	
i	Inclination	
L_\star	Stellar luminosity	
M_\star	Stellar mass	
\dot{M}	Mass loss rate	
v_∞	Wind terminal velocity	
z	Dust-to-gas mass ratio	
β	Electron ion ratio	
η	Wind momentum ratio	
$\Lambda(T)$	Plasma Cooling function	
$\Lambda_d(h, a, T)$	Dust cooling function	
ξ	Grain sticking efficiency	Eq. 2.16
θ_c	WCR conic opening angle	Eq. 2.1
τ_{KH}	Kelvin-Helmholtz timescale	Eq. 2.1
τ_{ff}	Free-fall timescale	Eq. 2.2
τ_{cool}	Cooling timescale	Eq. 2.21
τ_{esc}	Escape timescale	Eq. 2.22
μ	Mean molecular mass	
κ	Sub-timestep fraction	Eq. 3.16
χ	Cooling parameter	Eq. 2.23
σ	Stefan-Boltzmann constant	$5.670 \times 10^{-5} \text{ erg cm}^{-2} \text{ s}^{-1} \text{ K}^{-4}$
M_\odot	Solar mass	$1.988 \times 10^{33} \text{ g}$
$M_\odot \text{ yr}^{-1}$	Solar mass per year	$6.301 \times 10^{25} \text{ g s}^{-1}$
L_\odot	Solar luminosity	$3.828 \times 10^{33} \text{ erg s}^{-1}$
R_\odot	Solar radius	$6.957 \times 10^{10} \text{ cm}$
AU	Astronomical Unit	$1.496 \times 10^{13} \text{ cm}$
pc	Parsec	$3.086 \times 10^{18} \text{ cm}$

“Warm”	Warm temperature regime	$10^4\text{-}10^5\text{ K}$ ¹
--------	-------------------------	--

¹Personal preference

LIST OF TABLES

CHAPTER 1

Introduction & Motivation

1. INTRODUCTION & MOTIVATION

1.1 Dust Formation in Colliding Wind Binary Systems

1.2 Motivation

1.3 Thesis Structure

CHAPTER 2

Background

2. BACKGROUND

2.1 Early-Type Stars

The term Early-type stars is quite possibly the epitome of bad naming conventions in astrophysics, it's a very old term, coming from the dawn of astrophysics itself, quite opaque as to what it means, and also by definition *completely wrong*. In fact it is one of the most wrong pieces of terminology I can think of.¹ The first generation of astrophysicists found themselves asking very important questions such as “what even *are* stars?” and “what possible mechanism can allow a star to burn for so long?” Each of these questions was rather pressing for the burgeoning field, and the scientific community was aching for an answer.

Of course, like all pressing questions of the 19th century, it fell to Lord Kelvin to provide a convincing but incorrect answer. Kelvin assumed that gravitational collapse was the mechanism for a stars long-term heating, with younger, “early” type stars shining the brightest. Not only was the mechanism incorrect, but typically older main sequence stars are more luminous than their younger counterparts of a similar mass! However, as is the case with astrophysical terminology, the term stuck, to the confusion of many young astrophysicists. Instead, we now know that stars produce their energy through fusion. These reactions vary from sub-stellar deuterium and lithium burning, to main sequence p-p & CNO hydrogen burning processes, and finally to the triple- α and other exotic fusion processes for evolved massive stars. The more massive the star the greater the internal pressure, allowing for more exotic fusion processes. The bigger a star, the greater the core pressure and temperature, as all fusion reactions are highly dependent on temperature, stars with only a few dozen solar masses are thousands of times more luminous than our sun, but only live a fraction of the time (Carroll & Ostlie, 2014).

High-mass stars, of course, are the most luminous and short lived of stars. These stars have luminosities in the range of $10^4 L_\odot$ and lifespans on the order of 10 Myr, less than 0.1% of the lifespan of our sun. The adage of a candle burning twice as bright and lasting half as long doesn't quite express the differences between high-mass stars and low-mass stars, it would instead be better to compare a candle and a stick of dynamite. We define high-mass stars as stars that are sufficiently massive to undergo carbon fusion near the end of their lives. Defining high-mass as stars are predominantly driven by the CNO cycle or late-life helium burning can include intermediate mass stars, which form degenerate cores and evolve into white dwarfs. By

¹Aside from astrophysicists calling something “warm”, of course. That can quite literally mean anything from 10 to 10,000 Kelvin, depending on who you ask, what they’re writing about, or how they’re feeling at that particular moment. In fact, I’ll probably end up falling into this same trap somewhere in this thesis as well!

this definition, a high-mass star has a mass $> 8 M_{\odot}$, which includes stars in the O-type and some B-subtype (B0 and B1) classes in the Harvard classification system (Ward-Thompson & Whitworth, 2011, p. 143).

2.1.1 Formation

All stars form from the collapse of giant molecular clouds (GMCs), enormous, cold clouds containing truly staggering amounts of gas, the largest of which are on the order of a few parsecs across, and contain $10^4 M_{\odot}$ of future star-stuff. In order to create a star from this cloud, you must first perturb it, which is easier said than done, but can be induced by stellar winds from nearby stars, and shock-waves from supernovae (Bodenheimer, 2011, Ch. 3). As the cloud collapses, energy is radiated through emission line processes, which lowers the radius of thermostatic equilibrium. As the GMC collapses further it begins to fragment, forming the molecular clumps and cloud cores that will eventually condense into protostars. As one of these fragments condenses, forming a protostellar core, it can be described in the form of a series of timescales. First, the Kelvin-Helmholtz (KH) timescale¹, τ_{KH} , which is the time required for the protostellar core to radiate away its kinetic energy:

$$\tau_{\text{KH}} \approx \frac{GM_{\star}^2}{R_{\star}L_{\star}}, \quad (2.1)$$

where G is the gravitational constant, R_{\star} is the protostellar core mass, R_{\star} is the radius of the core and L_{\star} is the core luminosity. The other timescale is the free-fall timescale, τ_{ff} , which is the time taken for a molecular cloud to fully collapse onto the core, given by the equation:

$$\tau_{\text{ff}} \approx \sqrt{\frac{3\pi}{32G\rho_{\star}}} \quad (2.2)$$

where ρ_{\star} is the mean density of the collapsing cloud. The equation of motion for this system is:

$$\frac{d^2r}{dt^2} = -\frac{GM_{\star}}{r^2}, \quad (2.3)$$

for any point with radius r from the centre in the cloud, assuming spherical symmetry (Ward-Thompson & Whitworth, 2011, p. 96). In the case of a massive star, the KH timescale is

¹The idea of gravitational contraction as expounded by Lord Kelvin does in fact apply to stars, just not with regards to how their energy is produced.

2. BACKGROUND

Process	Reaction rate	Energy released per nucleon	Significant in
p-p	$\epsilon \propto T^{3.5}$ at 5×10^6 K	6.54 MeV	Low-mass stars
CNO	$\epsilon \propto T^{18}$ at 10^6 K	6.18 MeV	High-mass stars
3α	$\epsilon \propto T^{40}$ at 10^8 K	0.61 MeV	Post-main-sequence high-mass stars

Table 2.1: A comparison of reaction rates and released energy for the p-p chain reaction, CNO reaction and triple-alpha reaction. Whilst the 3α reaction has a much higher temperature dependence for the reaction, it requires much higher pressures, and produces considerably less energy per nucleon. These factors contribute to the high luminosities and short lifespans of high-mass stars.

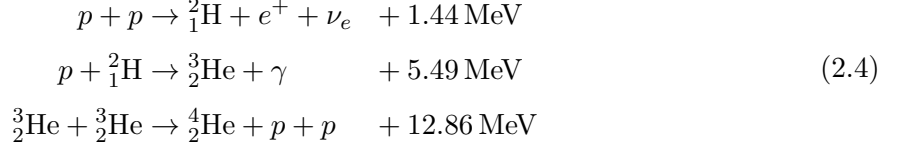
significantly shorter than the free-fall timescale ($\tau_{\text{KH}} \ll \tau_{\text{ff}}$), meaning that the material at the center of the collapsing cloud begins to fuse. This burgeoning star begins to drive the weakly gravitationally coupled collapsing material away due to its sheer luminosity, driving this material outwards, causing it to accrete and shock material within the GMC (Bodenheimer, 2011, Ch. 5).

As more massive cores collapse, they are more prone to fragmentation, the angular velocity of the fragments can cause them to begin orbiting one another, eventually forming a binary of multiple star system. Close binary systems can also form by way of fragmentation in the protostellar disk. Due to this fragmentation it has been observed that roughly 2/3^{rds} of all main sequence stars are found to be in a multiple system (Ward-Thompson & Whitworth, 2011, p. 113), with approximately 20% of stars in close binary orbits. However, in the case of massive stars, this value is significantly higher, with $> 82\%$ of stars with masses $> 16 M_\odot$ being found to be in a close binary system (Chini et al., 2012). As such, the environment within an OB association is one of many tight knit groups of young stars, which are disrupting the local area¹.

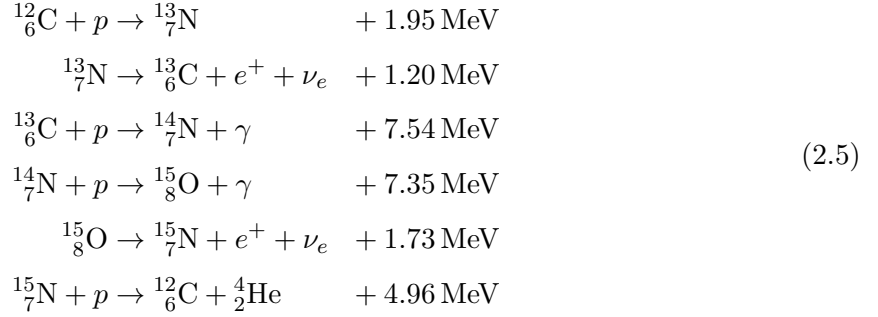
2.1.2 The p-p & CNO fusion cycles

As we have previously discussed, the KH mechanism is not the driving force behind the generation of energy in a star. Instead, we must briefly discuss the various nuclear fusion processes, in order to understand why massive stars are so luminous, as well as how their lives end. Nuclear fusion in stars was first proposed by Eddington (1920), though the exact process continued to be a mystery for nearly 2 decades, when Bethe (1939) discovered the p-p fusion reaction chain that drives approximately 90% of the energy generation of the sun. The p-p fusion chain dominates energy generation for stars between $0.08 M_\odot \lesssim M_\star \lesssim 1.3 M_\odot$, and releases energy by fusing protons into helium in a particularly direct manner:

¹This is similar to the environments around student areas, such as Hyde Park and Headingley.



However, whilst the reaction is particularly efficient, due to its high energy production per nucleon (Table 2.1), the reaction rate has a poor temperature dependence of $\epsilon \propto T^{3.5}$. In more massive stars, with core temperatures on the order of 10^8 K, the extreme luminosities we observe would simply not be present. As such, we can infer that the actual mechanisms underpinning fusion in intermediate and high-mass stars are much more energetic and temperature dependent. Above a stellar mass of $1.3M_\odot$ pressures and temperatures within a stellar core favour the fusion of hydrogen into helium through the catalytic CNO cycle, instead of the more direct p-p fusion process:



The CNO I cycle, as included, was also proposed by Bethe (1939), and has a markedly higher temperature dependence on the reaction rate, $\epsilon \propto 10^{18}$ (Wong, 1998, Ch. 10). The incredible densities at the cores of high-mass stars therefore result in a reaction rate orders of magnitude higher than the sun. This results in a convective core surrounded by a radiative envelope, and is the driving force behind the incredible observed luminosities of high-mass stars as they convert hydrogen to helium at an astounding rate (Salaris & Cassisi, 2005, Ch. 5).

2.1.3 Stellar winds

The luminosities and temperatures of high-mass stars also drive extremely fast stellar winds through radiative line driving. These winds are on the order of 10^{10} times stronger than winds from stellar-mass stars, and punch holes clean into the interstellar medium (ISM), forming wind-driven bubbles and champagne cork flows, as well as perturbing GMCs, allowing for further star

2. BACKGROUND

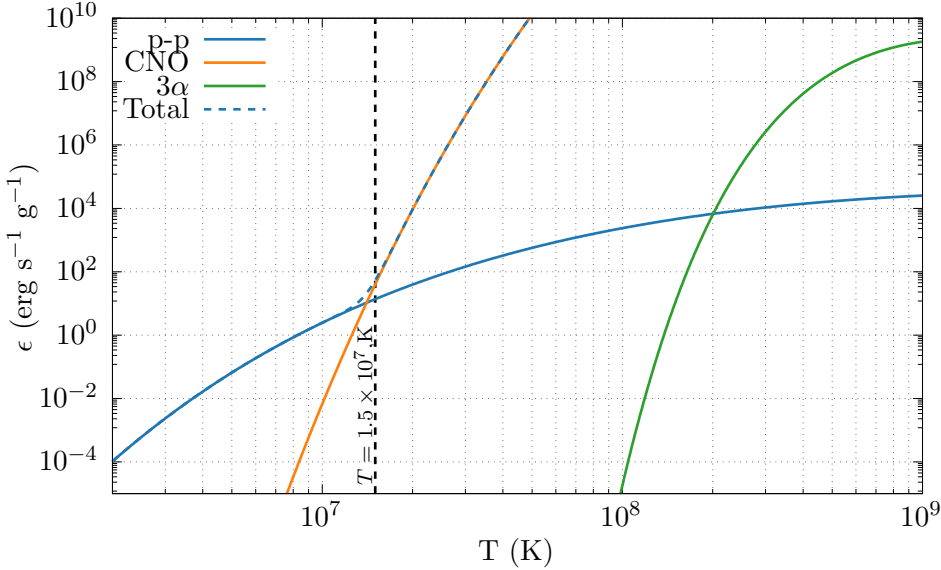


Figure 2.1: Reaction rates from p-p, CNO and triple- α fusion processes at the centre of the sun. At the solar core temperature of 1.5×10^7 K only 10% of the energy produced from fusion is through the CNO cycle. At higher internal temperatures the CNO cycle rapidly becomes dominant due to its stronger temperature dependence. The 3α process does not occur in the solar core, but becomes the dominant fusion process in high-mass stars leaving the main sequence. Solar abundances and a core density of 150 g cm^{-3} are assumed.

formation.

The study of stellar winds, of course, is quite hard from our vantage point on earth. Sampling the winds themselves is difficult due to the vast, inconvenient distances involved in sending a probe to collect the rarefied material from our stellar neighbourhood. Additionally, the bubble blown from our own suns stellar wind makes collection even more difficult, leaving the heliosphere is no easy feat either, just ask the Voyager probes. We instead derive the properties of these extrasolar winds from spectrography, with the adsorption and emission spectra of the winds betraying their composition. The velocity of these winds can be determined in much the same manner, through the Doppler shift of these emission lines. Early observations of stellar winds centred around the star P Cygni, the earliest known example of an evolved Luminous Blue Variable (LBV) star. the presence of peaks and troughs in the profile of a spectral line such as H- α was the cause of some scientific curiosity. This effect could only be explained by the presence of a shell rapidly expanding away from the star. The troughs of this emission line corresponded to a blue-shifted adsorption lobe, from radiation passing through this shell, while the emission line itself corresponded to the expanding shell itself (Beals, 1929; Lamers & Cassinelli, 1999). Observations of other stars typified this event, it was found that every star had a stellar wind,

though the speed and quantity of the ejected material could vary by many orders of magnitude.

In the simplest terms, we can describe a stellar wind as a spherical outflow from a star. We can describe this outflow in terms of its mass loss rate, \dot{M} , the amount of material ejected from the star, as well as its terminal velocity, v_∞ , or the maximum velocity a wind can obtain from its driving mechanism. We can use these to determine a profile of the density of a stellar wind as a function of its distance, r , from the star

$$\rho_w = \frac{\dot{M}}{4\pi v_\infty r^2}, \quad (2.6)$$

where the star is a point source. Whilst this barest description can give us some insight into how a wind behaves, we should discuss the driving mechanisms behind these winds, as well as the more complex models we use to describe them.

Driving mechanisms

Classification	\dot{M}	v_∞	Mechanism
	$M_\odot \text{ yr}^{-1}$	km s^{-1}	
Sun	10^{-14}	400	Thermal heating
PMS	$10^{-4} - 10^{-7}$	200-500	Rotation & magnetic fields
Red Giant	$10^{-7} - 10^{-9}$	30	Radiation pressure on dust grains
OB Star	$10^{-7} - 10^{-8}$	2,500	Radiation pressure & line driving
Wolf-Rayet	10^{-5}	1,500	Radiation pressure & line driving

Table 2.2: Comparison of stellar winds emitted from various classification of star.

Low-mass main sequence stars, compared to other classes of star, have supersonic ($\sim 400 \text{ km s}^{-1}$) winds that are relatively thin, with a mass loss rate of $10^{-14} M_\odot \text{ yr}^{-1}$. This results in a wind density profile orders of magnitude lower than other types of star, based on Eq. 2.6 (Fig. 2.2). The reason for this comparatively feeble outflow is the driving mechanism. The corona in stars with a convective envelope is approximately 3 orders of magnitude hotter than the stars photosphere, this hot corona exerts pressure on gas trapped within it, causing it to be expelled from the star. As this method is thermally driven, and does not expel gas from the envelope directly, this explains the comparative weakness. In fact, winds from red dwarfs are found to be markedly denser, but the mechanisms behind the driving force are less well understood. As low-mass stars evolve and leave the main sequence, swelling into red giants, the surface gravity of the star decreases dramatically. Furthermore, as the star expands and cools, dust condenses

2. BACKGROUND

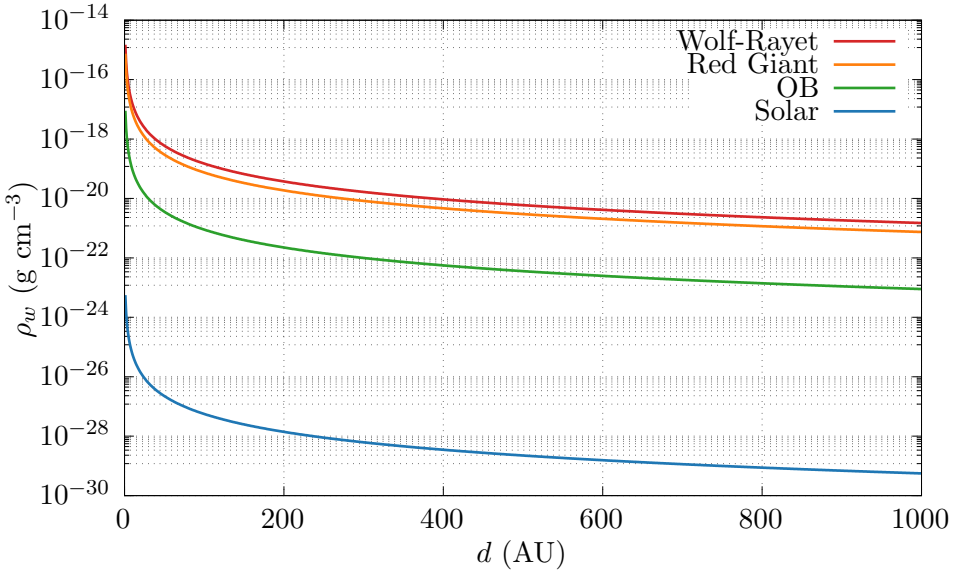


Figure 2.2: Comparison of the densities of various main sequence winds using the parameters specified in table 2.2, wind densities are estimated using the smooth wind approximation described in equation 2.6.

and forms in the photosphere. These dust grains adsorb photons more readily than ions and atoms through Thompson scattering, and can adsorb a broad range of wavelengths due to their size. Radiation pressure then drives these dust grains away, if the gas is sufficiently coupled to the wind this is driven away too, in the form of a dense, optically thick, barely supersonic wind (Lamers & Cassinelli, 1999, Ch. 5). The mass loss rates of these stars are extremely high, no lower than $10^{-7} \text{ M}_\odot \text{ yr}^{-1}$ and as high as $10^{-5} \text{ M}_\odot \text{ yr}^{-1}$ but have velocities on the order of $10 - 100 \text{ km s}^{-1}$.

By the 1970s the winds of early-type stars had been categorised, finding mass loss rates between 10^{-8} to $10^{-5} \text{ M}_\odot \text{ yr}^{-1}$ and wind velocities of 600 to $3,500 \text{ km s}^{-1}$. Additionally, it was found that the mass loss rate of these stars was approximately proportional to the luminosity ($\dot{M}_* \propto L_*^{1.1}$) (Cassinelli, 1979). This strongly suggested that the driving mechanism of these winds was based on radiation pressure, though thompson scattering would not be a sufficiently efficient process to drive winds of this magnitude. Furthermore, coronal heating and dust driving mechanisms were not possible, due to a lack of a convective envelope and lack of significant dust build up in the envelope, respectively.

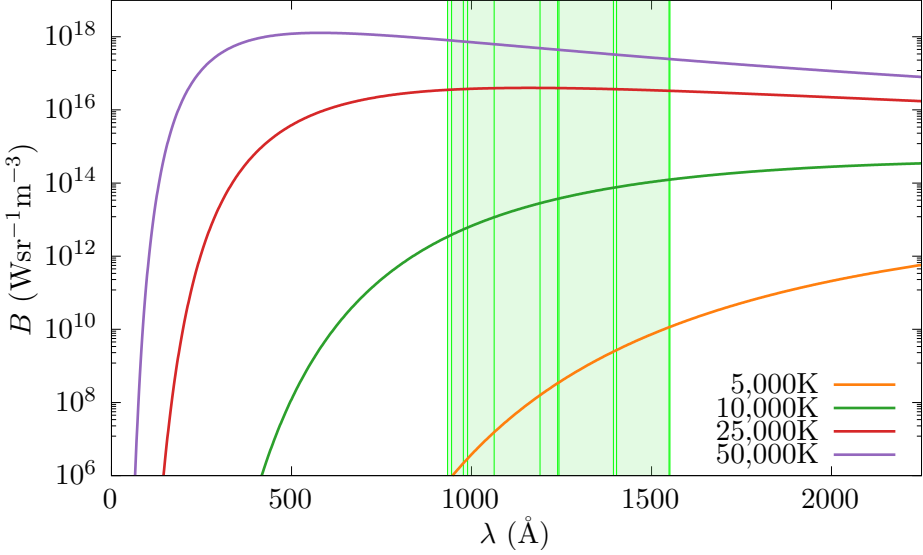


Figure 2.3: Spectral radiance against wavelength for black body objects at various effective temperatures, T_{eff} , a series of wavelengths corresponding with important resonance lines in Table 1 of Lucy and Solomon (1970) have been included. As temperature increases the spectral radiance at resonance line wavelengths dramatically increases, with a minimum of 6 orders of magnitude difference between the effective temperatures of a solar equivalent main sequence star and an O-type main sequence or Wolf-Rayet star.

Line-driven wind theory

Instead, wind driving through resonance lines was proposed. A photon with an energy equal to the excitation energy of an emission line of an ion in the wind is adsorbed, exciting the ion. This ion then de-excites over a timescale of 10^{-8} s, emitting a photon at a random angle relative to the radial direction relative to the star, α . This emission of a photo produces a recoil force on the ion, resulting in a change in the radial velocity, Δv_r , such that:

$$\Delta v_r = v_r'' + v_r' - v_r = \frac{\hbar\nu_0}{mc} (1 - \cos \alpha), \quad (2.7)$$

where v_r' is the ions radial velocity after the photon adsorption, v_r'' is the ions radial velocity after photon emission and ν_0 is the frequency of the resonating photon. Compared to Thompson scattering, resonance lines are 6 orders of magnitude more opaque, making it a much more efficient process (Lamers & Cassinelli, 1999, Ch. 8). This driving force occurs more readily with elements with a large number of resonant lines, heavier ions such as C, N, O and Fe group elements adsorb the photons. Lighter elements such as H and He are instead carried along via

2. BACKGROUND

Coulomb forces, coupled to the heavier elements so long as the medium is sufficiently dense.

But why is this effect not observed in lower mass stars? Firstly, resonance lines in heavier elements are comparatively high energy, requiring For instance, the C III resonance line has an energy of 12.69 eV, therefore a photon requires a wavelength of 977 Å in order to be adsorbed (Fig. 2.3). Secondly, photons would only be adsorbed over a narrow range of frequencies. This would inhibit efficient momentum transfer from UV photons without Doppler shift, as the outflow from the star has a distribution of radial velocities this results in a greater chance of resonance line adsorption. If we were to observe the outflow of a massive wind we would therefore see a relatively low velocity component of the wind close to the star; once the wind reaches a certain critical velocity. At a certain point we would observe a significant and rapid increase in the velocity of the wind, as the influence on adsorption due to Doppler shift results in the wind becoming much more opaque to UV photons. Eventually we would observe the wind reaching a terminal velocity, due to a decrease in photon flux from the inverse square law and the outflow becoming more diffuse as it spreads away from the star (Maciel, 2014, Ch. 10). This can be seen in Fig. 2.4, where the velocity increases sharply at a distance $(R/R_\star) - 1 > 10^{-3}$ as the wind begins to rapidly accelerate away from the star as opacity increases - with a corresponding decrease in wind density.

Theories of radiation pressure being the main driving force for massive stars was first considered by astronomers in the early 20th century, and was first proposed by Saha (1919). Later, Milne (1926) who predicted that after an initial acceleration phase from an ions emission lines, Doppler shift would be sufficient for continuum photons frequencies to match the resonant lines - causing a much greater impulsive force. Early calculations of the force on stellar winds due to resonance lines by Lucy and Solomon (1970) found initial estimates for the mass loss rate based on a series of resonance line in the C, N, Si and S species of ions. However, these were found to underestimate the mass loss by approximately two orders of magnitude. This is in part due to the models simplicity, due to limitations in both computing power and available data, as the force due to interaction of resonance lines with continuum photons were considered. The first major breakthrough was with more complex models demonstrated by Castor, Abbott and Klein (1975; CAK). The CAK model computed line forces from all emission lines in the C III ion, after estimating the line force from other ions by scaling the results of this calculation an estimate of mass loss rates for hot stars was calculated to within a factor of 3 of observational results. A much more complex emission line model developed by Abbott (1982) involved the calculation of the force from a startling 250,000 lines, however, this was found to be less accurate than the

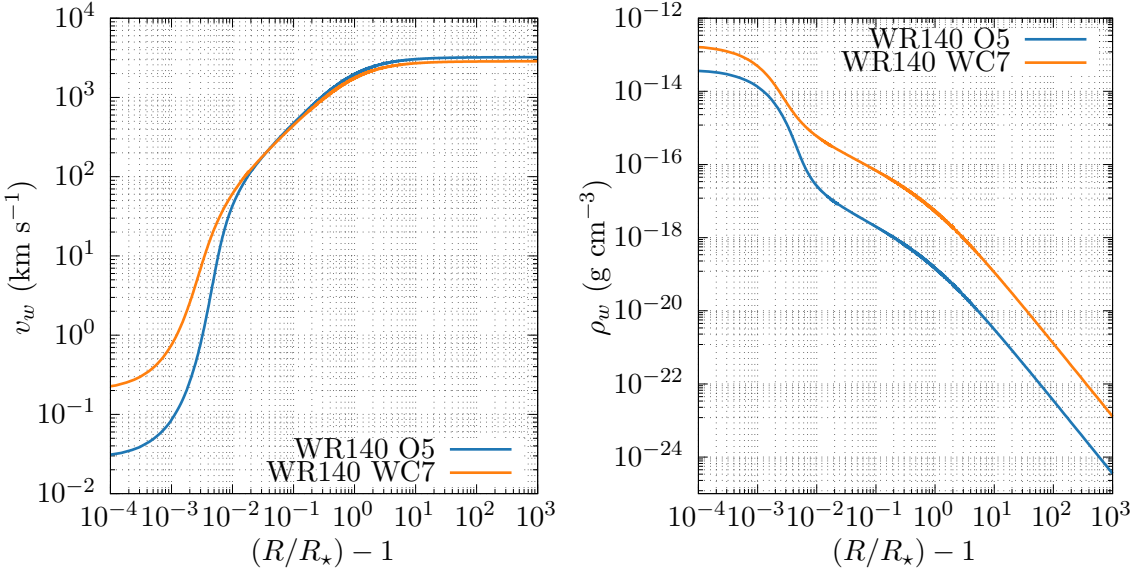


Figure 2.4: Velocity and density profiles of the WR and OB stars in the WR140 system. Acceleration is gradual until $(R/R_\star) - 1 > 10^{-3}$, where wind opacity drastically increases due to Doppler shift. The model uses the Castor, Abbott and Klein formalism, with the CAK parameters of the stars estimated to be $k = 0.37$, $\alpha = 0.60$ for the O4-5 star and $k = 0.48$, $\alpha = 0.57$ for the WC7 star.

original CAK model! This led to improvements on the approximations and assumptions made by the CAK model, namely the finite disk correction factor (Friend & Abbott, 1986; Pauldrach et al., 1986).

2.1.4 Evolved main sequence stars

Unfortunately for massive stars, pesky fundamental laws such as the conservation of energy come into play. With only an order of magnitude or two of additional mass more than our sun and shining 10^4 times as brightly, this curtails the life of the brightest stars to lifespans not much more than 10^7 years. If we define a galactic year as the time it takes for a star to orbit the Milky Way, these poor stars don't even make it to their first birthdays, which is quite sad really.¹

As the available hydrogen begins to become depleted, the lowering reaction rates force the star to shrink, this raises the internal temperature until the core begins to burn helium through the triple- α process:

¹Continuing this analogy our sun can drink, might have voted if they felt like it, and may be racking up vast quantities of student debt.

2. BACKGROUND



The sudden spike in energy radiating from the core shifts the calculus of hydrostatic equilibrium in the favour of outward forces, causing the star to rapidly expand in the form of a Red Supergiant or Luminous Blue Variable (Ryan & Norton, 2010). During this phase the energy output of the star is even greater, with a timescale of $\sim 10^6$ years, this is only temporarily prolonging the life of the star, which will inevitably begin burning heavier and heavier elements, faster and faster. Once the star starts producing iron its fate is sealed, the star stops fusing, and collapses, annihilating itself in the form of a supernova and leaving behind a remnant of its core in the form of a neutron star or black hole (Ward-Thompson & Whitworth, 2011).

Whilst the stars end is as inevitable as it is violent, the intermediate stage as the star leaves the main sequence is in itself extremely interesting, and for the context of this thesis, no product of this stage is more interesting than the Wolf-Rayet.

2.1.5 Wolf-Rayet stars

As we now know, Wolf-Rayets¹ are evolved forms of O-type stars, and are a short lived component of the life-cycle of massive stars, typically lasting for around 5×10^5 years (Crowther, 2007). Despite this relatively transient length of this stage, the influence of a WR star on its local medium is extremely outsized. WR stars in particular are known for having dense, fast winds, typically between 2 and 3 orders of magnitude than their main sequence O-type progenitors, with mass loss rates on the order of $10^{-5} M_{\odot} \text{ yr}^{-1}$ and wind velocities of $1.5 \times 10^3 \text{ km s}^{-1}$. This extremely dense wind is driven by the highly energetic helium burning core, which is luminous enough as to drive away the outer layers of the stars envelope, exposing the core. The observed spectroscopic lines are due to heating of the envelope from the core, which is enriched with by-products of hydrogen and helium burning, the lack of hydrogen lines is due to the stars evolved nature, as all the hydrogen has been burned, there is simply nothing left to observe!

Wolf-Rayet stars can be subcategorised through spectroscopic observation, which indicates enrichment in a particular element, the 3 major sub-types, WN, WC and WO are defined by their strong nitrogen, carbon and oxygen lines respectively. The important distinction between

¹Abbreviated to WR.

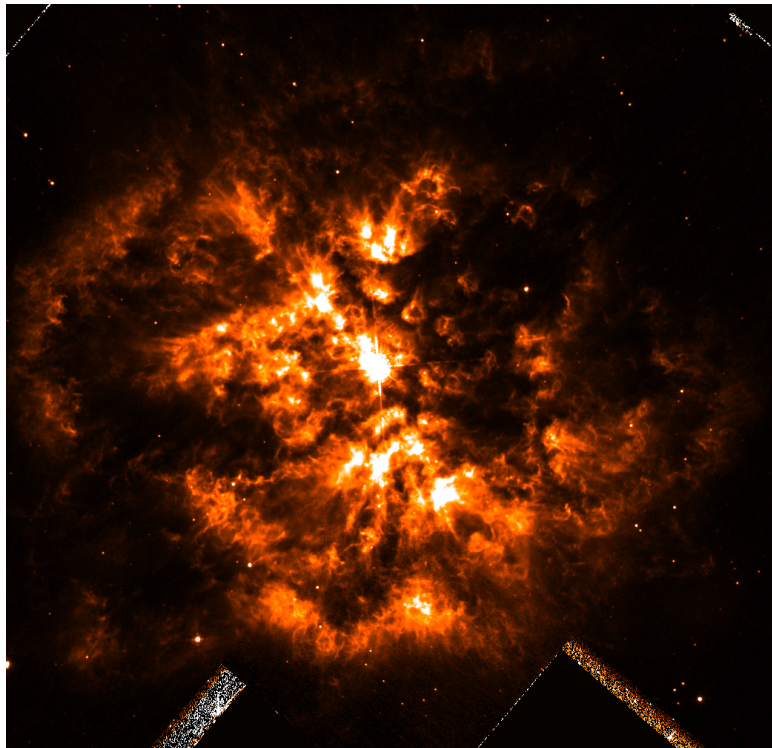


Figure 2.5: Reduced Hubble WFPC2 data of the WN star WR 124, its extreme mass loss is currently producing the ejecta nebula M1-67 (Marchenko et al., 2010).

WN and WC/WO stars is that WN stars are enriched through hydrogen burning, whilst WC and WO are enriched through the by-products of helium burning (Vink, 2015).

As a Wolf-Rayet continues to lose its envelope, additional products of fusion processes are dredged up from the centre of the star. In the case of the WN sub-type, the broad nitrogen lines correspond to the outer layer of the envelope, enriched through the CNO process; after this outer envelope is cast off, the remainder of the envelope exhibits carbon and oxygen lines, indicating enrichment from the triple- α process. Finally, the star evolves further and the innermost region of the envelope is revealed, observed as the strong oxygen lines of a WO sub-type (Neugent & Massey, 2019; Oswalt & Barstow, 2013).

As an O-type star transitions to a Wolf-Rayet, it typically undergoes an intermediary LBV or RSG stage as helium burning begins, this is mass dependent, with the various transitional states described by Crowther, 2007:

2. BACKGROUND

$O \rightarrow LBV/RSG \rightarrow WN(\text{H-poor}) \rightarrow WC \rightarrow SN\ 1b$, for $25\ M_{\odot} < M_{\text{WR}} < 40\ M_{\odot}$

$O \rightarrow LBV \rightarrow WN(\text{H-poor}) \rightarrow WC \rightarrow SN\ 1c$, for $40\ M_{\odot} < M_{\text{WR}} < 75\ M_{\odot}$

$O \rightarrow WN(\text{H-rich}) \rightarrow LBV \rightarrow WN(\text{H-poor}) \rightarrow WC \rightarrow SN\ 1c$, for $M_{\text{WR}} > 75M_{\odot}$

Wolf-Rayet stars are important in the context of this work due to their outsized influence within a WR+OB binary pair. The WR component of a WR+OB binary has an outsized contribution in returning material to the ISM, whilst also dominating the dynamics of the system, with their winds completely overpowering those of their O-type neighbours. In some cases, the dense, fast wind from the WR can collide with the much more tenuous wind from its partner, forming a strong shock, and a variety of fascinating effects. However, I wouldn't want to spoil too much too soon, but you can skip ahead to section 2.3, where this phenomena is covered in more detail.

2.2 Interstellar Dust

For much of the history of astronomy, interstellar dust was not its own field, nor was it studied in significant detail - instead it was regarded as nothing but a *nuisance*. Early astronomy, of course, was limited to the visible light spectra, at these wavelengths dust *is* in fact a nuisance, contributing nothing and extinguishing stars and the innermost depths of the galaxy. The first population counts of stars at the turn of the 20th century were hampered by this extinction, with Kapteyn (1909) noting that:

“Undoubtedly one of the greatest difficulties, if not the greatest of all, in the way of obtaining an understanding of the real distribution of the stars in space, lies in our uncertainty about the amount of loss suffered by the light on its way to the observer.”

The existence of dust grains was not considered until nearly a quarter of a century, with work by Robert J. Trumpler in 1930 concluding that the observed interstellar reddening effect could only be accounted for by small grains of cosmic dust. As technology progressed and non-visible astronomy became possible, we were for the first time able to peer past these obscuring clouds, bypassing them entirely. The scientific community also found that the interstellar dust itself

was interesting on its own, leading to further categorisation and parametrisation of these dust grains in the 1960s and 1970s (Whittet, 2002, pp. 4–13).

Interstellar dust, particularly in the case of small grains, is a loose collective of atoms and molecules held together by weak molecular bonds, typically only on the order of 10 Å to 100 Å in size. These grains are typically formed from small, refractory dust cores around 5 Å across, in high density regions such as stellar atmospheres and dark interstellar clouds (Spitzer, 2008). This initial accretion process can be quite rapid, as outflows from stars can be quite rapid, due to implantation of impinging carbon ions (Zubko, 1998). While the largest dust grains can be on the order of centimetres (in the case of protoplanetary disks), the initial grain size in this project that we will consider is approximately 50 Å. There are a multitude of ways that these dust grains can grow and shrink, though only a few are considered in this work, due to either difficulty of implementation into our model or time constraints. The first such mechanism for growth and destruction that will be discussed is grain-grain collision. Grain-grain interactions are the most easily understood, in regions with sufficiently high dust grain number densities, collisions can occur between the grains. The result of this interaction is dependent on the collision velocity between the grains. Low velocity collisions result in grain mergers, where these grains will stick together. An initial attractive force through van der Waals interaction will occur, bringing the grains into contact, upon collision the contact area will deform and flatten, allowing for the grains to coagulate and merge. Grain-grain coagulation occurs at very low velocities, typically $< 100 \text{ m s}^{-1}$, but this threshold velocity is typically lower for smaller, more tightly bound grains (Chokshi et al., 1993). At higher collision velocities these grains can simply bounce off of each other, doing very little damage outside of ablating some atoms off of the surfaces of the grains. At high velocities still these grains can shatter and fragment each other, which in the case of high velocity shocks with large grains can result in the grains being completely pulverised, turning from an accretion process to the principle cause of dust destruction (Jones, 2004; Jones et al., 1996).

The most important method of destruction of dust for this project is grain-gas sputtering, this thermal interaction dominates dust destruction at all temperatures in shocks. As an ion collides with a dust grain in a shock, the surface near the impact site is vaporised, this impact also drives a shock wave into the grain, which can melt and shatter parts of the grain. Over time material is ablated off of the dust grain, causing it to shrink in radius, and eventually completely shattered. In order to simulate this we must simplify and parametrise this into a model, we start by assuming that the dust grain is spherical. As the gas collides with the grain,

2. BACKGROUND

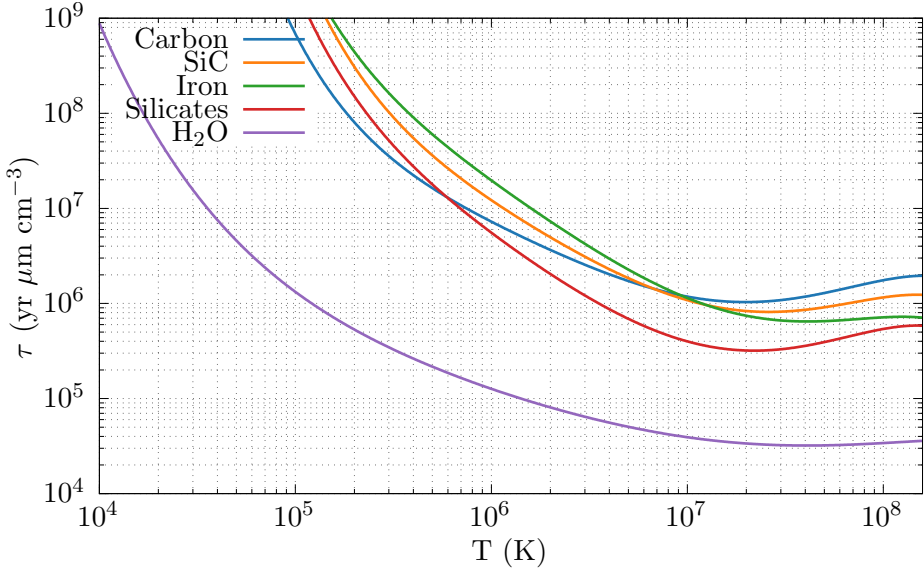


Figure 2.6: Comparison of grain lifetimes for various interstellar dust species undergoing thermal sputtering in a fast interstellar shock. Lifetime is normalised to a grain radius of $1\text{ }\mu\text{m}$ and a flow of 1 g cm^{-3} in a shock of solar abundance. Data is derived from 5th order polynomial fits calculated in Tielens et al. (1994, Table 4).

small amounts of the grain are vaporised and ejected from the surface, causing a reduction in grain radius, a , with a corresponding rate of radius change \dot{a} . \dot{a} can vary depending on the composition of the grain; for instance, grains composed of ice would be more readily vaporised by impacts than sturdier grains composed of carbon or iron. In this spherical case the dust destruction rate is inversely proportional to the number density of the gas, as the grain will be destroyed faster if there are more gas-grain interactions, and proportional to the grain radius. The dust destruction rate has a more complex dependency on the grain temperature, rapidly reducing below 10^6 K , and is found to be roughly flat above this temperature and to around $3 \times 10^8\text{ K}$ (Tielens et al., 1994). We can therefore adopt a normalised grain lifespan τ_d , which we can use to calculate the dust destruction rate in our simulations:

$$\tau_d \equiv \frac{a}{\dot{a}} \approx 3 \times 10^6 \frac{a}{n_g} \text{ yr}, \quad (2.10)$$

where n_g is the gas number density (Draine & Salpeter, 1979b; Dwek et al., 1996). The value of 3×10^6 yr was chosen for this project as it is more typical of temperatures in the post-shock region of a WCR, between 10^6 K and 10^7 K (Fig. 2.6). How this destruction rate is implemented into the simulations for this project is discussed in more detail in Section 3.8.

As with grain-grain interactions, at lower velocities grains can impact onto grains or their nuclei and stick to the surface. This steady accretion process be described in the form of a fairly simplistic model. By considering a spherical grain moving through a flow of atoms with a number density n_a , a certain number of these atoms would collide and stick to the dust grain, this sticking probability is defined as ξ . This sticking factor is found to be ≈ 1 for neutral atoms¹ (Watson & Salpeter, 1972). Above a threshold velocity, atoms fail to adhere to the grain surface, and at higher velocities still contribute to the sputtering process instead (Spitzer, 2008). For this research, this threshold temperature was defined as 14,000 K. If we model a grain of radius a , the cross section, σ , of the grain moving through the gas would be $\sigma = \pi a^2$. In the case of a grain moving through a gas of composition x and density ρ_x where the grain is significantly larger than the atoms composing the gas, it is found that the rate of change in the grain mass, dm_{gr}/dt , is:

$$\frac{dm_{\text{gr}}}{dt} = \sigma w_x \rho_x = \pi a^2 \rho_x w_x \xi_x, \quad (2.11)$$

where w_x is the RMS velocity of the gas. The associated rate of change in grain radius, da/dt , is found to be:

$$\frac{da}{dt} = \frac{w_x \rho_x \xi_x}{4 \rho_{\text{gr}}}, \quad (2.12)$$

where ρ_{gr} is the bulk density of the dust grain.

A myriad of other dust destruction processes exist, such as electron-grain and cosmic ray-grain interaction, but these are considered to be out of the scope of this project, and not influential in the case of a hot gas or dense post-shock environment (Jones, 2004). Outside of shocks, dominant destruction processes include thermal and photo-dissociation methods. UV light emitted from stars can ionise atoms on the surface of the grain, ejecting them from the surface, slowly “boiling” material from the grain. This of course makes the premise of our project all the more curious, with so many mechanisms underpinning dust destruction, particularly in hot, dense environments, how come we observe significant dust production in Wolf-Rayet binary systems?

¹Though we adopt a more conservative value of 0.1 due to the turbulent nature of the environments that are studied in this project.

2. BACKGROUND

2.2.1 Dust composition

The most important species of interstellar dust in this thesis are those composed of carbon. sp^2 - (graphite) and sp^3 -bonded (diamond) dust grains have been detected from their characteristic emission lines, as well as hydrocarbon chains and Polycyclic Aromatic Hydrocarbons (PAHs). Complex organic molecules have also been detected in dusty environments, they are believed to have formed in the surface of dust grains, instead of forming within the ISM itself (Herbst & van Dishoeck, 2009). The primary dust detected in CWB systems is amorphous carbon grains, which are defined as grains with a mixture of sp^2 - and sp^3 -bonded carbon, with no structural order or polymerisation (Draine, 2003). Other species of interstellar dust are abundant throughout the ISM; these species include water ice, silicate grains and Polycyclic Aromatic Hydrocarbons (PAHs). However, these grain species have not been detected in dust producing CWB systems, in part due to element depletion, as WC stars are hydrogen-depleted. Amorphous carbon grains are also markedly more resistant to erosion and fragmentation due to shocks than other grain types. They are also more resistant to thermal sputtering as well, due to their higher sublimation temperature, this resilience is vital if they are to survive in the extreme conditions of a CWB system (Draine & Salpeter, 1979a).

2.2.2 Radiation processes in interstellar dust

Interstellar dust can be a significant factor in the cooling of its local interstellar medium through a series of continuum and line emission processes. Collisional excitation and adsorption of photons can stochastically heat dust grains, this excess energy is then emitted in the form of near-infrared radiation (Dwek et al., 1996). The radiative emittance of a dust grain can be approximated as a black body, and hence radiates in accordance with the Stefan-Boltzmann law:

$$L = 4\pi r^2 \sigma T^4, \quad (2.13)$$

where L is the grain luminance, r is the grain radius, σ is the Stefan-Boltzmann constant and T is the grain temperature. At sufficiently high gas densities this radiative process can become the dominant cooling method in the ISM (Wolfire et al., 1995). In addition to this continuum emission, emission lines can also occur if characteristic vibrational modes in a grain lattice are excited, such as the silicate grain stretching and bending vibrational modes at 9.7 μm and 18.5 μm (Whittet, 2002, p. 212).

Discuss the mathematics of this in more detail.

2.2.3 The importance of interstellar dust

We should ask ourselves, why are dust grains important enough to merit thousands of papers, and dozens of doctoral theses? Over this short section we will attempt to explain in brief why dust grains so important.

Over 150 molecular species have been observed in the interstellar medium, with a surprisingly complex degree of organic chemistry; of the molecules with six or more atoms that have been detected, 100% of these have been organic in nature. Such complex organic molecules include benzene, acetone and ethanol, this degree of complexity should not necessarily be possible in interstellar gas-phase chemistry. Instead, these organic species form on the surface of interstellar dust grains, with gas-phase chemistry accounting for simple molecule formation such as H₂ and CO (Herbst & van Dishoeck, [2009](#)). The role of dust as the chemical refineries of the interstellar medium has a number of effects when it comes to star and planetary formation, as well as organic and pre-biotic chemistry throughout the universe. It is no understatement to say that the universe would be remarkably different if interstellar dust was not so readily abundant. Dust grains are also vitally important in the star formation cycle. As a Giant Molecular Cloud (GMC) collapses following perturbation, heat is generated, in the adiabatic case the increased temperature would provide a counterbalancing pressure on the collapsing cloud, forming a hydrostatic equilibrium and preventing the cloud from collapsing any further. In the case of extremely massive clouds, this collapse can still occur as gravity will dominate, but this equilibrium dictates the minimum mass for a cloud to collapse into a protostar. As such, for all but the most massive stars to form, energy must be lost in the form of radiation (Ward-Thompson & Whitworth, [2011](#)). As radiative cooling from dust grains is extremely efficient in cold, dense environments, this mechanism is well-suited for the environment of a GMC. In addition to cooling through rotational mechanisms of simple molecules in the gas-phase of the medium, these processes sufficiently cool the GMC, allowing for further collapse. In addition, dust grains would also provide a replenishing source of cooling molecules such as CO and OH through non-thermal grain desorption processes. The presence of dust grains within a GMC therefore strongly influences the minimum mass of stars (D. A. Williams & Cecchi-Pestellini, [2015](#)).

Interstellar dust is also crucial for the formation of planets. Collision between refractory

2. BACKGROUND

dust grains is the first stage of planetesimal formation, within the protoplanetary disk, low velocity collisions between micron-sized grains can occur, causing these grains to stick and rapidly accrete. If local region of the disk is gravitationally unstable, these small grains will form a gravitationally bound cluster, and contract over time into a planetesimal, afterwards, rapid accretion of other planetesimals gives rise to the formation of both rocky planets and gas giants (Apai & Lauretta, 2010). Dust is also a regulator of opacity, which determines the temperature structure and composition of the protoplanetary disk. Finally, and perhaps most importantly to the reader, the complex organic molecules produced in the dust grain are pre-biotic precursors to life (Birnstiel et al., 2016).

As the role of interstellar dust in star and planet formation, as well as the long-term implications of the formation of life in the universe are *slightly* out of the scope of this project, I will stop here, but it is always interesting to consider the repercussions of the topics that you research.

2.3 Colliding Wind Binary Systems

Colliding Wind Binaries (abbreviated hereon to CWBs), in opposition to all known laws of astrophysical nomenclature, is a easy to understand term - it is a binary system where stellar winds from the member stars undergoing collision. Unfortunately, the simplicity of the systems ends here, CWB systems are very poorly understood phenomena, due to a variety of factors that this section will discuss.

2.3.1 History of CWB observation

Early observations beyond visual spectrum led to the discovery of many new astrophysical phenomena, one such discovery were extremely bright and variable thermal X-ray sources. Many of these early galactic X-ray sources were found to be compact objects, and many more contained the characteristic spectral lines of a Wolf-Rayet star. While single Wolf-Rayet stars are capable of producing X-ray emission, this is typically much dimmer than what was being observed (Seward et al., 1979). The existence of CWB systems were independently proposed by Prilutskii and Usov (1976) and Cherepashchuk (1976), they proposed that significant and variable X-ray flux would result from the collision between two stellar winds, as these winds collide the gas becomes shocked and heated to temperatures on the order of 10^8 K, hot enough to emit an

appreciable quantity of X-rays. The X-ray variability can also be explained as a result of the orbital properties of the systems, X-ray variability would result from the following effects:

- Eccentricity in the orbits of the systems, leading to differing shock intensity and changing of the shock geometry, changing the fraction of the winds being shocked.
- Edge-on orbits resulting occlusion of x-rays by the stellar wind from each star.
- Face-on orbits resulting in photospheric eclipses.

Such effects could not be produced within a single star system (Pittard, 1999). Further research by Pollock (1987) also found that single WR stars were typically faint, with the brightest X-ray emitting WR stars being confirmed to within massive binaries. WR+OB systems were also found to be the brightest of such objects, while OB+OB binaries with significant X-ray flux were observed, these were typically less luminous. Early work was more concerned with X-ray observation, in particular the systems γ^2 Velorum and V444 Cygni, which were noted in particular as prototypical CWB systems by Prilutskii and Usov (1976). Later, infrared observations of these systems found another, more curious attribute, a significant excess correlating to dust formation around these systems (P. M. Williams et al., 1987). This will be discussed in more detail later in this section, but needless to say this phenomena is puzzling, as fragile grains of interstellar dust would not survive for long in the outflow of a WC star, due to the high wind temperatures and immense UV flux. Because of this, dust growth was speculated, and later confirmed, to occur within the Wind Collision Region, the topic of the next section of this thesis.

2.3.2 The Wind Collision Region

The Wind Collision Region (WCR) is the most violent and turbulent region of a CWB system, a region of high densities and even higher temperatures. If the interacting stellar winds are dense as they begin to interact, a shocked region of plasma in excess of 10^8 K is formed, the winds rapidly decelerate from hypersonic to subsonic, liberating an enormous amount of mechanical energy, on the order of $10^3 L_\odot$. As previously discussed, this is the engine that drives the significant X-ray flux observed by astronomers in the 1970s, as well as other thermal and non-thermal emissions from the UV up to gamma rays (Eichler & Usov, 1993; Grimaldo et al., 2019). As wind enters from either side of the wind collision region, it passes through a shock wave, and flows towards the centre of the wind collision region at the contact discontinuity, C (Fig. 2.7).

2. BACKGROUND

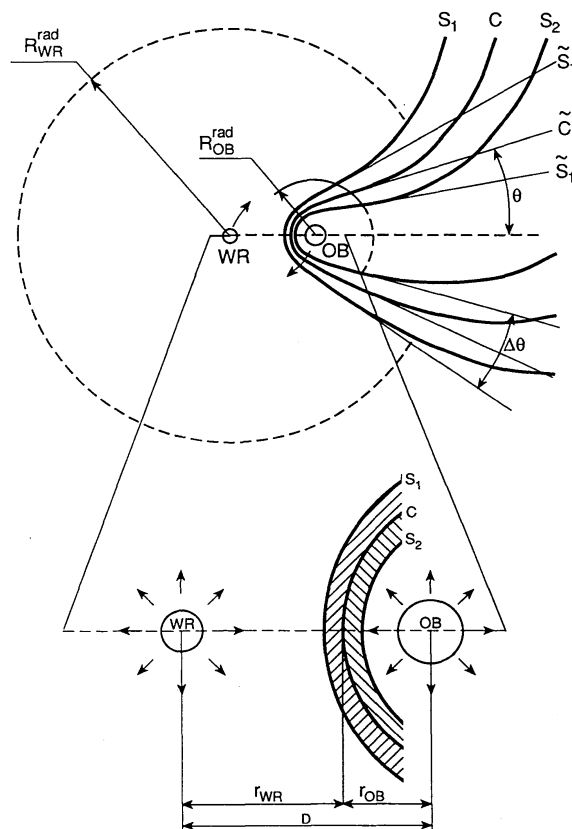


Figure 2.7: A diagram of a typical Wind Collision Region inside a WR+OB CWB system. The S_1 and S_2 surfaces denote the shock waves from the primary and secondary winds respectively, and C denotes the contact surface. The surfaces \tilde{S}_1 , \tilde{S}_2 and \tilde{C} represent conic approximations of their corresponding surfaces at intermediate distances from the OB star. The region of stellar wind collision is hatched in the bottom diagram (Eichler & Usov, 1993).

2.3 Colliding Wind Binary Systems

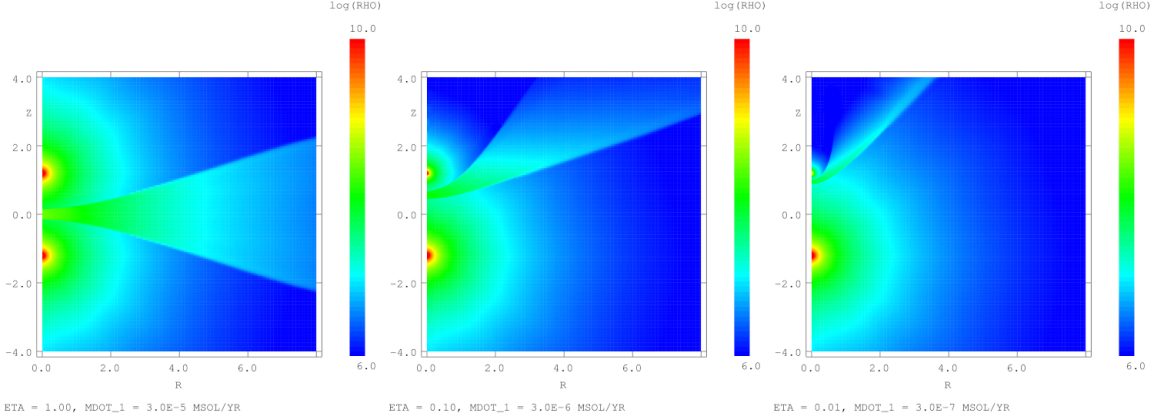


Figure 2.8: 2D axisymmetric hydrodynamical simulations of CWB systems with wind momentum ratios of 1, 0.1 and 0.001. Momentum ratio is varied by changing the mass loss rate of the second star, \dot{M}_2 . As η decreases, the WCR begins to wrap itself around the secondary star.

The wind behind the shock is driven by a combination of thermal pressure from the outflowing stellar wind, as well as the significant momentum the wind carried before being shocked (Stevens et al., 1992).

The geometry of the WCR is influenced strongly by the wind parameters of both stars, the most important of which is the wind momentum ratio, or η , which we define as:

$$\eta = \frac{\dot{M}_{\text{OB}} v_{\text{OB}}^{\infty}}{\dot{M}_{\text{WR}} v_{\text{WR}}^{\infty}}, \quad (2.14)$$

where \dot{M}_{WR} and v_{WR}^{∞} denotes the mass loss rate and wind terminal velocity of the primary, typically Wolf-Rayet star and \dot{M}_{OB} and v_{OB}^{∞} denotes the mass loss rate and wind terminal velocity of the OB partner (Usov, 1991). A lower value of η indicates a more unbalanced wind, with wind momentum ratio of 0.01 or lower being common for a typical WR+OB system. Additionally, if $\eta = 1$, we observe a sheet of interacting plasma flowing away from the system perpendicular to the orbital plane. In the case of a system where one stars momentum is significantly larger than the other, we observe the WCR extend and envelop the OB star, forming an approximately conical surface extending away from the Wolf-Rayet star (Fig. 2.8).

As the wind becomes more and more imbalanced, the contact discontinuity moves closer to the OB partner, this can be estimated with the equation:

2. BACKGROUND

$$r_{\text{WR}} = \frac{1}{1 + \eta^{1/2}} d_{\text{sep}}, \quad r_{\text{OB}} = \frac{\eta^{1/2}}{1 + \eta^{1/2}} d_{\text{sep}}, \quad (2.15)$$

where r_{WR} is the distance from the WR star to the contact discontinuity, r_{OB} is the distance from the OB star to the contact discontinuity and d_{sep} is the orbital separation distance of the stars.

$$\theta_c \simeq 2.1 \left(1 - \frac{\eta^{2/5}}{4} \right) \eta^{-1/3}, \quad \text{for } 10^{-4} \leq \eta \leq 1, \quad (2.16)$$

Work by Pittard and Dawson (2018) on determining the accuracy of opening angle expressions such as equation 2.16 found that this approximation is accurate under the condition $\eta > 0.01$, but begins to diverge significantly if this condition is exceeded. This was accomplished through a series of hydrodynamical simulations with different values for η , with the resultant opening angle calculated from the fully advected simulations. This work goes on to derive analytical solutions to the opening angles of the conic approximations of \tilde{S}_1 and \tilde{S}_2 , these solutions were found to be:

$$\theta_1 = 2 \tan^{-1} (\eta^{1/3}) + \delta\theta, \quad (2.17a)$$

$$\theta_2 = 0.658 \log_{10} (71.7\eta) \quad (2.17b)$$

where $\delta\theta$ is a small correction factor found to be $\approx \pi/9$. From these estimations the fraction of each wind that is shocked, f , can be calculated:

$$f_1 = \frac{1 - \cos(\theta_1)}{2}, \quad (2.18a)$$

$$f_2 = \frac{1 + \cos(\theta_2)}{2}. \quad (2.18b)$$

Pittard and Dawson (2018) observed that the entirety of the secondary wind was shocked if $\eta \lesssim 0.014$, while in the typical wind momentum ratio regime $0.001 \leq \eta \leq 0.01$, only $\approx 10\%$ of the WR wind is shocked (Fig. 2.9). These expressions, while useful for describing the geometry of WCR in broad strokes, are based on adiabatic simulations with instantaneous acceleration, and thus have their limitations.

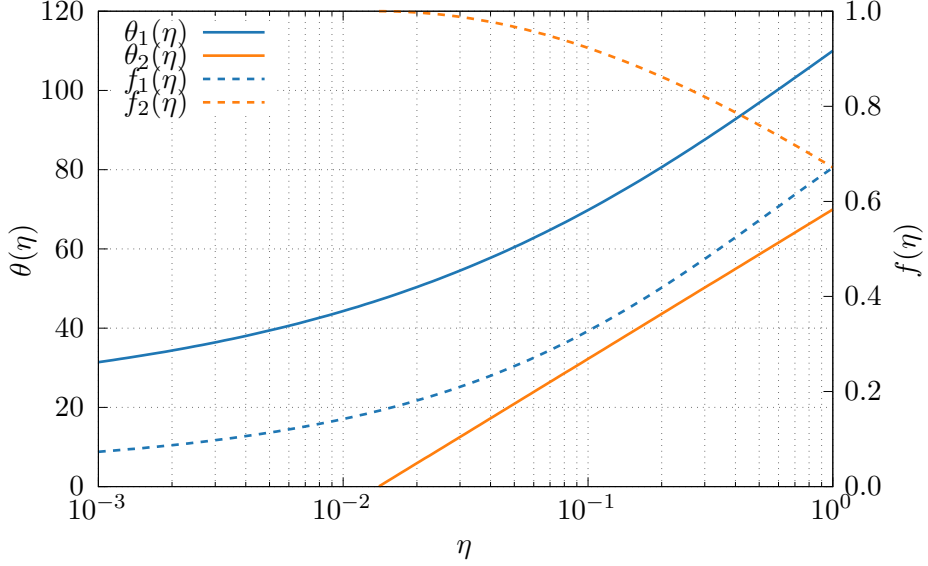


Figure 2.9: Comparison of the opening angle of \tilde{S}_1 and \tilde{S}_2 as a function of η . The wind shock fraction, f , is also plotted. $\approx 10\%$ of the primary wind is shocked under typical WR+OB conditions, while the entire secondary wind is typically shocked.

Orbital motion is also a significant factor in the geometry of a WCR, as the stars orbit each other the WCR curves and wraps around the system, as the angle of the WCR relative to the outflow from the system is constantly changing. The conical approximation as described in Eichler and Usov (1993) was found to be valid to a distance of $r_{\text{OB}} \ll r \ll (Pv_{\text{WR}}^\infty)/2$, where P is the orbital period. In systems with a short orbital period, this can result in the production of a pinwheel-like structure as the WCR extends away from the stars. In particular, the systems WR104 and WR98a produce easily observable pinwheel structures, especially in the infrared.

2.3.3 Cooling in the WCR

Temperature range	Dominant process	Spectral region
$5 \times 10^3 \text{ K} \lesssim T \lesssim 10^5 \text{ K}$	Forbidden lines	IR, Optical
$T \approx 10^5 \text{ K}$	H excitation/ionisation	Optical, UV
$5 \times 10^3 \text{ K} \lesssim T \lesssim 10^5 \text{ K}$	Resonance lines	Far UV, soft X-ray
$T \gtrsim 10^8 \text{ K}$	Bremsstrahlung	Radio

Table 2.3: Breakdown of dominant cooling processes at various temperature ranges from Dyson, 2021, whilst H excitation/ionisation occurs over a very short temperature range, it is extremely influential, causing a global peak in the cooling rate at $\approx 10^5$ K. These temperature ranges are depicted in Fig. 2.10.

2. BACKGROUND

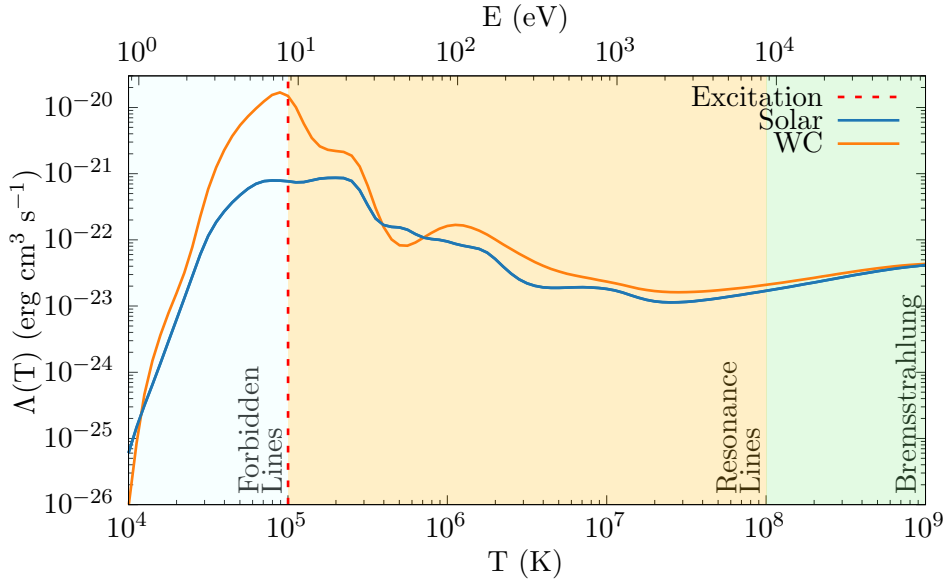


Figure 2.10: Normalised plasma cooling rates as a function of temperature and thermal energy for solar abundance and WC abundance winds. The regions where forbidden line, resonance line and bremsstrahlung emission are dominant are highlighted, with H ionisation and recombination occurring between the forbidden and resonance line sections at 10^5 K.

Cooling due to radiation emission in a hot plasma can be broken down into a variety of processes that occur over series of temperature ranges. Ions inside a plasma can become excited through collisions or photon absorption resulting in emission of photons as the ions de-excited. Mechanisms that are significant within the warm¹ and hot gas phases include forbidden line emission, hydrogen excitation and ionisation, resonance lines and bremsstrahlung (Dyson, 2021). The influence of each mechanism varies over a particular temperature range, with each mechanism dominant over a certain temperature range (Table 2.3 and Fig. 2.10).

The first mechanism to be discussed is forbidden line emission². This process dominates the cooling process of cooler gas that is not fully ionised, where collisions with free electrons excite metallic elements within the gas, which de-excite through magnetic dipole and quadrupole fine structure state transitions. This process dominates at these temperatures as the transition energies are significantly lower, on the order of 1 eV, as the photon is also of a comparatively long wavelength, it can more easily escape from the surrounding gas.

¹See what I mean about the phrase “warm”?

²Like many other phenomena discussed in this thesis, this too is a misnomer, while initially assumed to be prohibited under the contemporary understanding of atomic physics, it is in fact just astrophysicists jumping the gun again.

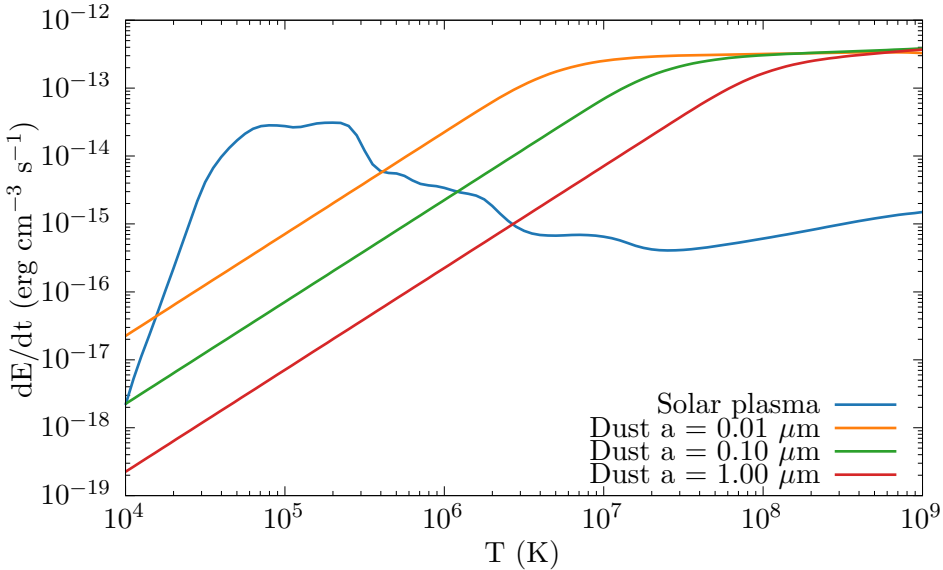


Figure 2.11: Comparison of plasma cooling to dust cooling with different grain sizes in a solar abundance gas, with a gas density of $10^{-20} \text{ g cm}^{-3}$ and a dust-to-gas mass ratio of 0.01.

As the temperature increases there is a spike in the cooling rate of the gas as the hydrogen present begins to fully ionise, at this temperature a hydrogen ion and an electron may recombine, releasing a cascade of photons as the electron de-excites.

As the plasma heats further resonance lines can

As the particle energy reaches the range of tens of keV, bremsstrahlung¹ becomes dominant (Fig. 2.10). High velocity electrons are deflected by ions, emitting radiation in the process due to conservation of energy.

(Schure et al., 2009) (Rybicki & Lightman, 2004)

We define an energy loss rate of a volume of gas, \dot{E} , which in the case of plasma cooling is calculated by the equation:

$$\frac{dE}{dt} = \left(\frac{\rho}{m_H} \right)^2 \Lambda(T) = n_g^2 \Lambda(T) \quad (2.19)$$

where n_g is the number density of the gas and $\Lambda(T)$ is the emissivity of the gas. The gas is assumed to be optically thin.

Radiative cooling through plasma and dust cooling can play an extremely important role in

¹Or braking radiation when you can't remember how to spell it.

2. BACKGROUND

the dynamics of the WCR. A more radiative WCR will typically be dominated structurally by thermal and thin-shell instabilities, leading to regions with markedly higher local gas densities. In addition to these instabilities, the region will overall be significantly more dense, as a radiative shock is capable of compressing gas beyond the adiabatic limit of $\rho_{\text{post-shock}} = 4\rho_{\text{pre-shock}}$. The post-shock region will also be much cooler, as gas can cool back to the initial wind temperature. This allows dust to form, and is perhaps the most important factor for explaining dust formation in a CWB system. The influence on radiative cooling varies from system to system, but the influence is determined exclusively by the wind properties and orbital separation of the system, leading to it being consistent in systems with circular orbits, and can vary significantly in the case of systems with highly elliptical orbits. This provides further clues for the mechanisms behind the formation of dust in the WCR, as we shall see later. The extent to which the WCR is affected by cooling is dependent on similar parameters that govern the shape and structure of the WCR itself. Cooling becomes influential on the structure of the WCR if the immediate post-shock gas is able to cool to the post shock temperature shortly after escaping from the shock, this is described in this thesis as:

$$\chi = \frac{\tau_{\text{cool}}}{\tau_{\text{esc}}}, \quad (2.20)$$

where τ_{cool} is the cooling timescale and τ_{esc} is the escape timescale. The cooling timescale is the time required for the gas to radiate all of its energy at a rate \dot{E} , hence, $\tau_{\text{cool}} = E/\dot{E}$ or:

$$\tau_{\text{cool}} = \frac{k_B T_s}{4n_w \Lambda(T_s)}, \quad (2.21)$$

where k_B is the Boltzmann constant, T_s is the shock temperature and n_w is the post-shock wind number density. The escape timescale represents the approximate time taken for the gas to escape the shock, corresponding to:

$$\tau_{\text{esc}} = \frac{d_{\text{sep}}}{c_s}, \quad (2.22)$$

where c_s is the post-shock sound speed. As the expected shock temperatures of a CWB align closely with a local minima in $\Lambda(T)$, χ can be approximated with the equation:

$$\chi \approx \frac{v_{\infty,8}^4 d_{\text{sep},12}}{\dot{M}_{-7}}, \quad (2.23)$$

where $v_{\infty,8}$ is the wind terminal velocity in units of 10^8 cm s^{-1} , $d_{\text{sep},12}$ is the separation distance in units of 10^{12} cm and \dot{M}_{-7} is the mass loss rate in units of $10^{-7} M_{\odot} \text{ yr}^{-1}$ (Stevens et al., 1992). In the case of a CWB system with a cooling parameter $\chi \gg 1$, the system is adiabatic, leading to smooth winds and gas remaining at high temperatures, as it can only cool through expansion. In the case of $\chi \leq 1$, the system is strongly radiative, the gas rapidly cools after being shocked, leading to a very dense post-shock region with a structure strongly influenced by thermal instabilities.

As we can see from Eq. 2.23, we find that strongly radiative WCRs are favoured in stars with stars with slow, dense winds and close orbits. Wind velocity in particular is highly influential on the radiative dynamics of the WCR, and could be one of the driving reasons for a lack of dust formation in certain WC sub-types. Systems with high eccentricities can also vary their orbit significantly, leading to fluctuations in χ by 2 orders of magnitude. The corresponding velocity shear between a WR and an OB wind also results in the formation of Kelvin-Helmholtz instabilities.

Dust cooling

The presence of dust within the immediate post-shock environment significantly increases the cooling rate. Fig. 2.11 compares rate of cooling due to dust emission of various types of grains to plasma cooling at solar abundances, As Λ_g and Λ_D are both proportional to ρ_g^2 , dust cooling will dominate at high temperatures so long as there is sufficient amounts of dust.

As dust grains collide with ionised gas and electrons, this imparts kinetic energy into the grains, heating them and causing them to emit infrared radiation. Assuming that there is a net accretion of ions and electrons onto the dust grains and the gas is optically thin in the infrared regime, energy is efficiently removed from the gas. At particularly high temperatures this effect can dominate over high-temperature plasma cooling processes such as bremsstrahlung, as seen in Fig. 2.11. Fig. 2.12 compares dust grain heating rates due to electron and ion collisional excitation in a solar abundance and WC abundance flow. At lower temperatures the dust grain cooling rate is dominated by electron excitation, especially in the WC case as the ratio of free electrons to ions is significantly higher, as the WC flow is enriched by heavier elements. However, as the grain temperature increases, collisional heating due to ions becomes more prevalent as the electrons are sufficiently energetic to pass through the grain without significant energy transfer; this is referred to as the electron transparency, h_e (Dwek & Werner, 1981).

2. BACKGROUND

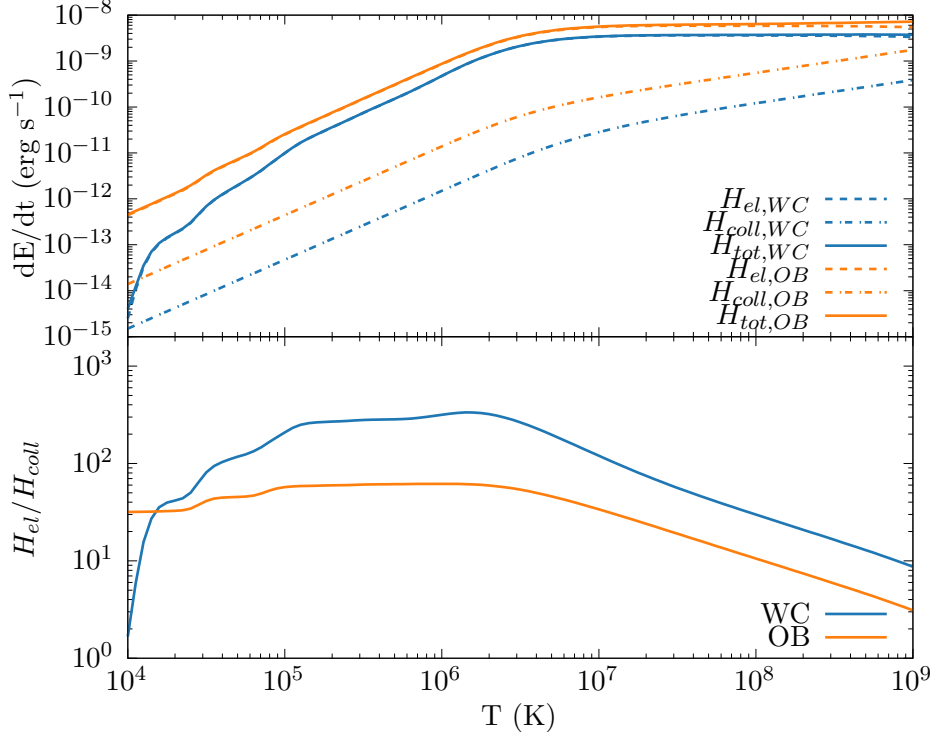


Figure 2.12: Comparison of grain heating rate due to ion collisional excitation, H_{coll} , and electron excitation, H_{el} . The dust grain has a grain radius of $5 \times 10^{-3} \mu\text{m}$ and is travelling through a gas with a density of $10^{-20} \text{ g cm}^{-3}$ with solar and WC abundances.

Work by Dwek and Werner, 1981 is used predominantly in this project to simulate cooling due to dust, a fast method for calculating the cooling rate due to dust was integrated into the numerical code for this project, which is elaborated on in section 3.7.3.

The heating rate of a dust grain due to collisions

$$H_{coll} = n\pi a^2 \langle Q(E, q, U) \rangle \times \langle v(E - qU) f(a, E - qU) f(a, E - qU) \rangle \text{ erg s}^{-1} \quad (2.24)$$

This can be simplified and expressed in the equation:

$$\begin{aligned} H_{coll} &= \left(\frac{32}{\pi m} \right)^{1/2} n\pi a^2 (k_B T)^{3/2} h(a, T) \\ &= 1.26 \times 10^{-19} \frac{n}{A^{1/2}} a^2 (\mu\text{m}) T^{3/2} h(a, T) \text{ erg s}^{-1} \end{aligned} \quad (2.25)$$

2.3 Colliding Wind Binary Systems

	Persistent		Variable		Episodic	
	Total	Example	Total	Example	Total	Example
WC4	1	WR19	0	—	0	—
WC5	0	—	0	—	1	WR47C
WC6	1	WR124-10	0	—	0	—
WC7	3	WR102-22	0	—	4	WR140
WC8	6	WR13	1	WR48a	3	WR122-14
WC9	45	WR104	6	WR98a	1	WR75-11
Total	56		7		9	

Table 2.4: Number of confirmed WCd systems with known spectral type and dust formation type from the Galactic Wolf-Rayet Catalogue (Rosslowe & Crowther, 2015), systems with uncertain spectral types not included, while systems labelled “d” are included within the “persistent” category for their associated spectral type.

2.3.4 Dust formation in CWB systems

Despite the extremely violent conditions thus far described in CWB systems, these systems appear to be extremely prolific producers of interstellar dust. Whilst single star WC systems can produce small amounts of dust in the form of amorphous carbon grains (though this could be observed to be extremely rare, pending the results of Medina et al. (2021)), binary systems have been observed to convert up to 10^{-3} of their wind masses from ionised carbon into amorphous carbon dust grains, this results in a typical dust production rate of $10^{-8} M_{\odot} \text{ yr}^{-1}$, on part with a typical Asymptotic Giant Branch (AGB) star. This dust forming behaviour has only been observed in particularly energetic WC stars (predominantly WC9, with some WC7-8 examples), WN and WO systems have not been observed producing dust, this is most likely due to amorphous grains being significantly more chemically stable and resilient to effects such as sublimation and photoevaporation than water ice or silicate grains (Draine & Salpeter, 1979a; Salpeter, 1977). Dust formation is also observed to form within the WCR, which can form quite beautiful pinwheel-shaped patterns, as dust streams away from the stars in the post-shock outflow.

Whilst beautiful, Wolf-Rayet systems are elusively rare. The Galactic Wolf-Rayet Catalogue¹ (Rosslowe & Crowther, 2015) has a collection of 667² known galactic WR stars, 106 of such stars are contained within a binary system, with 41 such binaries containing WC stars. Rosslowe and Crowther (2015) notes that there are a total of 42 confirmed WCd systems, approximately 35% of all WC systems, though this value is somewhat out of date and includes single star systems. A more up-to-date estimate performed for this thesis using the updated dataset estimates a total of

¹The most recent version of this catalogue is available at <http://pacrowther.staff.shef.ac.uk/WRcat>

²At time of writing, with the last update being August 2020.

2. BACKGROUND

80 WCd systems, of which 72 have well-determined spectral subtypes (table 2.4). Rosslowe and Crowther (2015) goes on to estimate that out of an estimated total of 1900 galactic WR stars, approximately 300 of these stars are predicted to be dusty WC stars. Whilst this is a far cry from the number of galactic AGB stars - of which carbon-rich AGBs outnumber WCd stars by approximately 3 orders of magnitude (Ishihara et al., 2011) - these systems can still significantly impact the surrounding interstellar medium, with strong stellar feedback propagating large quantities of dust into the surrounding medium.

Table 2.4 contains an excerpt of the observed WCd systems with clearly defined spectral subtypes, most dust producing stars are either WC8 or WC9 subtypes, which are markedly cooler and less luminous than their WC4 counterparts. This reduced luminosity is potentially the driving factor for dust formation in the system. As WC8-9 systems have slower, cooler winds (Niedzielski & Skorzynski, 2002), they are more strongly influenced by post-shock cooling, allowing for greater dust formation within the WCR. A small number of these systems have somewhat variable or episodic dust production cycles, such as WR98a and WR140, which are the two systems being observed within this thesis. Furthermore, the bulk of WCd systems do appear to be in binary systems with a close periastron passage, in fact, this orbit itself appears to be a driving force behind how dust is produced in these systems, as we will later discuss.

A good starting point to understanding dust formation is to understand how the WCR can mitigate the mechanisms resulting in dust destruction, whilst aiding the processes involved in dust formation. As previously discussed, dust can be destroyed through high-velocity collisions with grains, as well as evaporation through heating or ionising radiation. These processes are mitigated through the cooling, as well as the high level of UV extinction due to the high density of the WCR. Meanwhile, the dust production rate increases within high density regions, as collisions between dust grains and gas occur at a much higher rate. The same can be said with dust grains, allowing for fast growth from gas and impinging ion accretion, and grain-grain collision as the number density of dust grains begins to increase. The accumulation of these effects would be a very fast initial growth rate, which tapers off as the post-shock region diffuses and expands, resulting in a reduction in density.

The presence of instabilities driven by cooling and other factors can lead to pockets of high density post-shock material, as high density drives dust formation, this can lead to “clumps” of highly dust-enriched post-shock stellar wind. These clumps would have additional protection from UV photons, and would also be cooled enough for dust to form, thus, the driving hypothesis

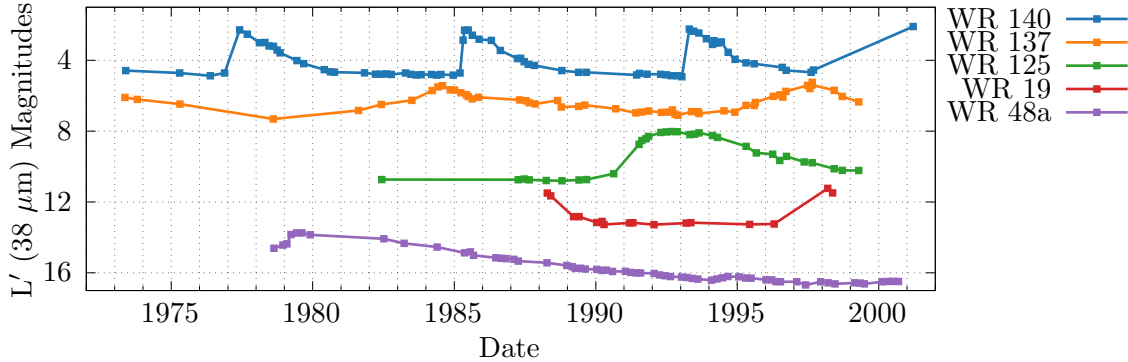


Figure 2.13: L' photometry for episodic dust making stars, data derived from Crowther (2003), and provided by PM Williams in private correspondence. WR 140 and WR 137 in particular have extremely predictable dust forming events which correspond to periastron passage in both systems.

for this theory is that these are regions where the bulk of dust formation would occur. As such, it is theorised in order to achieve a high rate of dust formation, a dense, highly radiative post-shock WCR must be formed, as cooling in the post-shock region is dependent on separation distance, wind velocity and mass loss rate, these parameters should first be explored, with the knowledge gleaned used to direct an analysis of observed systems such as WR140.

Eccentricity appears to play an important factor in the production of dust, highly eccentric systems can vary their dust production rates significantly. Fig. 2.13 shows the periodic change in mid-IR emission that can be explained as dust emission from small amorphous carbon grains, in the case of systems such as WR140 or WR125 dust production can be reduced to the point where associated emissions can drop by several magnitudes. This relation is clearly periodic, with a peak in dust production coinciding with the periastron passage of these systems. This implies that dust production is dependent on orbital separation, which will influence the degree of cooling occurring within the WCR, it could potentially also alter the wind velocity on collision, which will also influence dust production in the same manner. Further analysis of available dust producing CWB systems suggests that *all* WCd systems with circular orbits produce dust either persistently or with a degree of variability, while eccentric WCd systems are solely produce dust episodically.

2. BACKGROUND

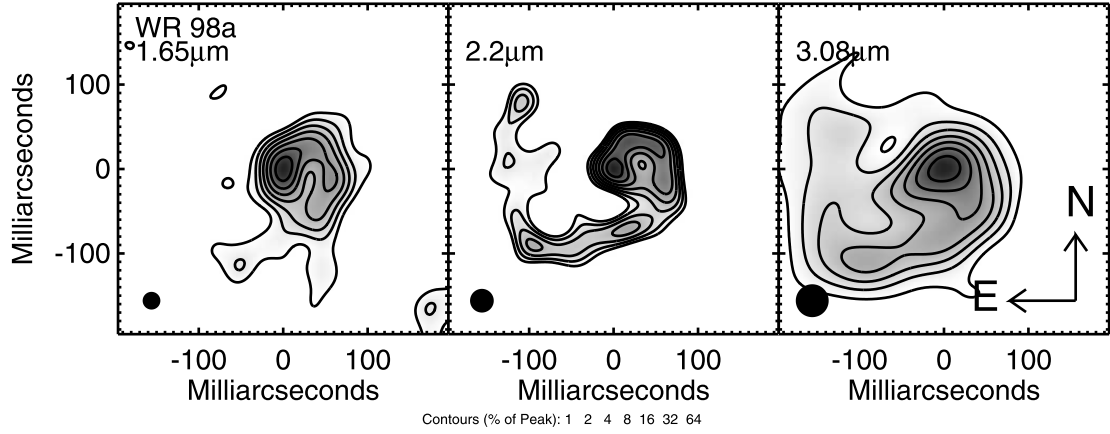


Figure 2.14: Multiwavelength aperture synthesis images of WR98a taken on June 24th 2000, at 1.65, 2.2, and 3.08 μm . Plot sourced from Monnier et al. (2007), the significant IR excess is a clear sign of ongoing dust production. The system also has a pronounced pinwheel structure most prominent at 2.2 μm .

2.3.5 Important WCd systems

The principle systems that are being observed in this thesis are the variable dust forming system, WR98a, and the episodic dust forming system WR140. The archetypal continuous dust forming system WR104 was also proposed for simulation, but had to be cut due to time constraints, this system will also be discussed to provide a point of comparison between the two systems.

System	\dot{M}_{WR} ($M_{\odot} \text{ yr}^{-1}$)	\dot{M}_{OB} ($M_{\odot} \text{ yr}^{-1}$)	v_{WR}^{∞} (km s^{-1})	v_{OB}^{∞} (km s^{-1})	η	χ_{\min}	\dot{M}_{D} ($M_{\odot} \text{ yr}^{-1}$)
WR98a	5.0×10^{-6}	5.0×10^{-8}	900	2000	0.0222	0.7970	$(6.10^{+1.77}_{-1.38}) \times 10^{-7}$
WR104	3.0×10^{-5}	6.0×10^{-8}	1220	2000	0.0033	0.2430	$(4.39^{+1.27}_{-0.97}) \times 10^{-6}$
WR140	5.6×10^{-5}	1.6×10^{-6}	2895	3200	0.0314	2.6866	$(8.11^{+4.83}_{-4.15}) \times 10^{-10}$

Table 2.5: Wind properties of systems considered for simulation in this thesis.

System	Classification	Period (d)	Eccentricity (e)	Inclination (i)	M_{WR} (M_{\odot})	M_{OB} (M_{\odot})	Periastron (AU)	Apastron (AU)
WR98a	WC8-9+OB	556	~ 0	$35 \pm 6^\circ$	10.0	18.0	4.06	4.06
WR104	WC9d+B0.5V	245	0.0600	$\lesssim 16^\circ$	10.0	20.0	2.20	2.48
WR140	WC7+O5	2869	0.8993	$119.1 \pm 0.9^\circ$	10.31	29.27	1.53	26.9

Table 2.6: Orbital properties of systems considered for simulation in this thesis.

WR98a

WR98a is a WC8-9+OB variable dust formation system. It has an approximately circular orbit with a semi-major axis of 4.06 AU, and is inclined at $\approx 35^\circ$ from Earth.

(Monnier et al., 1999)

WR98a was chosen for simulation primarily due to its moderate rate of dust formation, and comparatively docile winds. With a slow WC wind velocity of 900 km s^{-1} and a WC mass loss rate of $5 \times 10^{-6} M_\odot \text{ yr}^{-1}$

The dust formation rate is lower than many WC systems (Lau et al., 2020)

Due to these factors the system is markedly easier to simulate, and thus provided a good starting point for our work as we refined the model and implemented features into the hydro-dynamical system.

A comparatively wide orbit reduces the number of cells required to simulate the system, simplifying the simulation of the system further.

Finally, WR98a has previously been simulated using a multi-fluid dust model in Hendrix et al. (2016), this allows us to provide a point of comparison between our work and already published work. This is especially useful as there are only a handful of papers that cover dust models in CWB systems.

Because of this relative ease of simulation and relatively slow wind velocity for both stars in the system, WR98a was chosen to be the baseline system for the research conducted in chapter 4.

WR140

WR140 is significant in that it is the first system to be observed with episodic dust forming CWB properties, P. M. Williams et al. (1978) notes a rapid brightening in the infrared, suggesting the formation of a new shell of dust around the system. WR140 has undergone frequent observations, with spectroscopic data going back to 1972, and is perhaps the most well-observed episodic WCd system, for this it was immediately considered for

As it is a highly eccentric system with a particularly long period orbit, a number of difficulties with the constraints of only having SMR available throughout this project, with AMR not

2. BACKGROUND

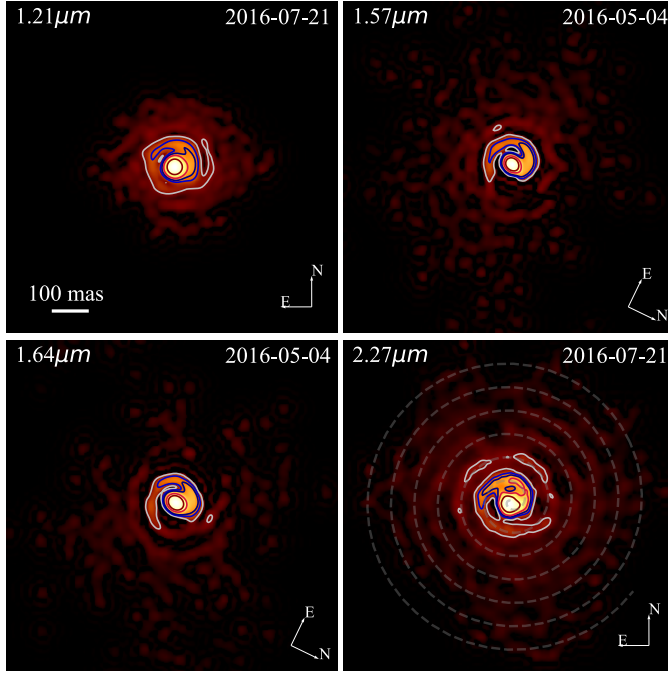


Figure 2.15: Deconvolution of J, H, K, and 2.27 μm bands of WR104 sourced from Soulain et al. (2018). The spiral pattern and first revolution is visible in all images, in particular at 2.27 μm .

currently being stable in this particular hydrodynamical code, As such, it was decided to only simulate the system as it undergoes closest approach, from $\phi = 0.95$ to $\phi = 1.10$, as a full orbit of the system would require AMR to undertake within the time constraints remaining in this project.

WR104

WR104 is an archetypal example of a continuous WCd system, it is a comparatively tight binary with a semi-major axis of 2.34 AU and a period of ~ 241 days, the orbit is also relatively circular, with an eccentricity of $e = 0.06$ (Lamberts et al., 2012). The system consists of a WC9 star with a B0.5V partner (P. M. Williams & van der Hucht, 2000), this combination of a WC star and a comparatively weak B partner results in a severely imbalanced wind, with a momentum ratio of 0.003, an order of magnitude lower than WR98a. This imbalanced wind, combined with the tight orbit, results in an extremely strong WCR that is constantly churning out dust. Using radiative transfer models, Harries et al. (2004a) calculated a dust production rate of $(8 \pm 1) \times 10^{-7} \text{ M}_\odot \text{ yr}^{-1}$, corresponding to 2% of the carbon mass loss rate of A more advanced

2.3 Colliding Wind Binary Systems

model by Lau et al. (2020), which is used to assess the dust formation rates of systems in this thesis, calculated the dust formation rate to be $(4.39^{+1.27}_{-0.97}) \times 10^{-6} M_{\odot} \text{ yr}^{-1}$.

WR104 can be considered to be an ideal example of a continuous dust forming system, the system is relatively close, at a distance of 2.5 kpc, and is at an inclination that is almost face-on relative to Earth, at $i \lesssim 16^{\circ}$. As such, the pinwheel outflow from the system can be clearly resolved, with infrared excess due to dust clearly observed within the pinwheel structure (Soulain et al. (2018), see Fig. 2.15). Due to the systems parameters and well defined observable dusty pinwheel structure, along with prior observations and simulations of the system, it is an ideal candidate for simulation

There are a number of reasons for this prodigious dust formation rate, as the systems orbit is comparatively close and circular with a very dense primary wind, the wind is expected to be highly radiative throughout the entire orbital period, this suggests a cool post-shock WCR that can continuously produce dust. The estimated cooling parameter is more than an order of magnitude lower than the other systems considered for simulation, leading to a

Unfortunately, despite being a very strong candidate for simulation, attempting to simulate the system proved to be exceptionally difficult. The very close orbit of the system would mandate a very high simulation resolution, increasing the amount of compute time required to finish the simulation, only simulating a small region would prevent the pinwheel from being formed and observed, which we would have ideally wanted to include. In addition the strong radiative cooling resulted in the simulation being very unstable unless the Courant number is exceedingly small, this also significantly increases compute time. With a limited amount of compute resources as well as a limited amount of time, this stretched the feasibility of simulating this system. As the wind from the primary star is significantly stronger than its partners, WR104 has a much lower momentum ratio than the other systems being considered, as such, the WCR is situated much closer to the secondary star. At closest approach, $r_{\text{OB}} \approx 60 R_{\odot}$, which would require WR104 to be simulated at a much higher resolution, in turn demanding significantly more computational resources. Physical effects, such as radiative inhibition and sudden braking may also significantly alter the wind velocity and post-shock environment, reducing the pre-shock primary wind velocity Gayley et al. (1997). The pre-shock secondary wind velocity would also be influenced, due to insufficient acceleration from line driving before the winds collide. As radiative line driving is not simulated these effects cannot be taken into account, and would have resulted in an inaccurate simulation of the system. The effect of incomplete acceleration and

2. BACKGROUND

sudden braking in highly wind-imbalanced systems is discussed more substantially in section [3.7.1](#). With limited time remaining in the project, as well as the above factors, simulation work on WR104 was abandoned in favour of a parameter space search of a system with baseline properties similar to WR98a, as well as a limited simulation of WR140. Simulating this system however, is a particularly enticing avenue of future research.

2.3.6 WR+WR systems

Recently, two candidates of a theorised subset of CWB have been discovered - WR+WR systems, which have a *second* Wolf-Rayet star as their partner, with a secondary wind around 3 orders of magnitude denser than a WR+OB system, this would of course result in a truly titanic wind collision. These candidates are the recently discovered WR70-16 ([Callingham et al., 2019](#)), and the previously discovered WR48a system ([Danks et al., 1983](#)), which exhibits the spectroscopic lines of both a WC and WN system ([P. M. Williams, 2019](#)). These systems are predicted to be comparatively rare, even among CWB systems, this is largely due to unlikelihood that both stars in the system would be in their Wolf-Rayet phase at the same time. Despite these systems having an enormous combined mass-loss rate, initial estimates of the dust production rates of both systems indicate that their dust conversion efficiencies are comparatively low compared to less energetic systems, and overall quite mundane dust production rates in general. Whether this suppressed dust production rate is a common phenomena among WR+WR systems remains to be seen, as more systems would need to be discovered in order to determine this.

WR70-16 (“Apep”) – a recently discovered WR+WR system

A potential avenue of research for this field is the simulation of WR+WR systems such as the recently discovered WR70-16 system (hereafter referred to as “Apep”), this system was discovered due to the significant difference between the spectroscopically derived wind velocity of $(3,400 \pm 200) \text{ km s}^{-1}$ and the observed expansion speed of $(570 \pm 70) \text{ km s}^{-1}$ ([Callingham et al., 2019](#)). This inhibited wind velocity, far below any categorised WR wind velocity, suggests that much of the wind undergoes collision with the wind of a binary partner. The extremely luminous non-thermal and infrared emission, suggested two extremely high mass loss rate stars within the system, as well as evidence for a third, distant partner in a loose trinary system ([Callingham et al., 2020](#)). Spectroscopic analysis suggested that the central component of the Apep system consists of a nitrogen sequence WN4-6b and a carbon sequence WC8 star, with more

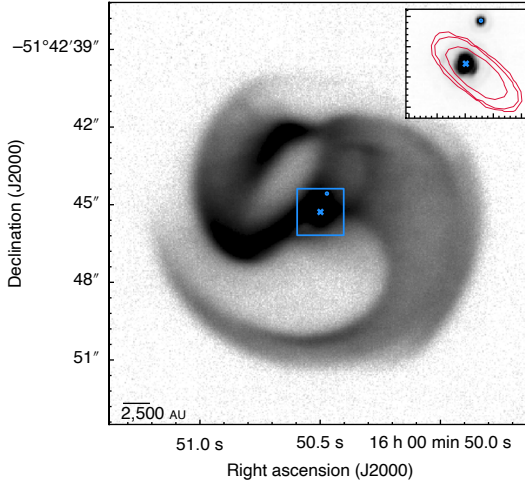


Figure 2.16: Callingham et al. (2019)

massive and luminous WN4-6b star kinematically dominating the system. This discovery is very significant as it is the first galactic WR+WR system discovered, other systems have been identified, but are extragalactic in nature.

Further work by Han et al. (2020) has estimated the orbital parameters of Apep, finding that it is a highly eccentric system with a period of (125 ± 20) yr and an eccentricity of 0.7 ± 0.1 , inclined at $\pm 30^\circ \pm 5^\circ$ towards Earth. An initial estimate of the dust formation rate was made, finding a dust production rate of $\sim 5 \times 10^{-7} M_\odot \text{ yr}^{-1}$, while observation of the surrounding dust shell suggests that it is a periodic dust forming system, which is sensible considering the systems high eccentricity.

The opening angle of the WCR was found to be very wide, at $125^\circ \pm 10^\circ$, further suggesting the presence of two very high mass loss rate objects within the system, suggesting relatively balanced wind momenta for a CWB system. Additional calculations by Marcote et al. (2021) estimated the systems wind momentum ratio to be 0.44 ± 0.08 , again in line with WR+WR hypothesis. Finally, pre-print work by del Palacio et al. (2021) finds a mass loss rate of $4 \times 10^{-5} M_\odot \text{ yr}^{-1}$ for the WN star and $2.9 \times 10^{-5} M_\odot \text{ yr}^{-1}$ for the WC star, which all but confirms the presence of a WR+WR binary at the heart of Apep.

With an estimated combined mass loss rate of $6.9 \times 10^{-5} M_\odot \text{ yr}^{-1}$ we can estimate that the system has a dust conversion efficiency of 0.7%; whilst this system is therefore not a prodigious producer of dust this is most likely due to the extremely high wind terminal velocity and high separation distance, which would suggest a fairly smooth and adiabatic post-shock region. We

2. BACKGROUND

can estimate the cooling parameter of the system to be ~ 80 , based on angular separation from Han et al. (2020), confirming that at present, the winds are adiabatic. In order to estimate the closest approach of the system, and therefore the minimum cooling parameter an accurate measure of the stellar mass of both objects would need to be made, there is insufficient data for this at the time of writing.

WR48a – revisiting a WR+WR candidate

WR+WR systems appear to be incredibly rare, with only a small number of extragalactic WN sequence examples in the LMC (Shenar et al., 2019), as well as an additional galactic WR+WR binary candidate, WR48a, (Zhekov et al., 2014; P. M. Williams, 2019; Zhekov et al., 2022). In the case of WR48a, its change in classification from a dust forming WC8 with an unknown partner to a WC8-WN8 is contemporaneous with the discovery and classification of Apep, though there is a distinct lack of recent observations of the system compared to the more recent WR+WR candidate.

Lau et al. (2020) calculated a dust formation rate for WR48a of $(8.46^{+3.48}_{-4.38}) \times 10^{-8} M_{\odot} \text{ yr}^{-1}$ with a dust conversion efficiency of 0.12%, markedly less than other systems with much less available material. A future avenue of research would be to simulate these systems to understand why the dust formation rate is comparatively low, despite the readily available stellar material. The main difficulty of simulating these systems is the lack of orbital parameters and accurate mass loss rates, as WR48a has insufficient data and Apep has only been recently discovered, there are currently too many unknown factors in order to build an adequate simulacrum of the systems¹. Another difficulty is the large degree of orbital separation, high eccentricity and long orbital timescales required to simulate these systems. The current limitations of the hydrodynamical code being used in this project render it difficult to simulate entire orbital passes of highly elliptical systems with long periods, if these issues are resolved in later versions of the hydro code however, this would present an interesting avenue of future research.

¹A lack of accurate orbital parameters is also an issue in devising simulations for more conventional WR+OB systems

CHAPTER 3

Methodology & Numerical Simulation

3. METHODOLOGY & NUMERICAL SIMULATION

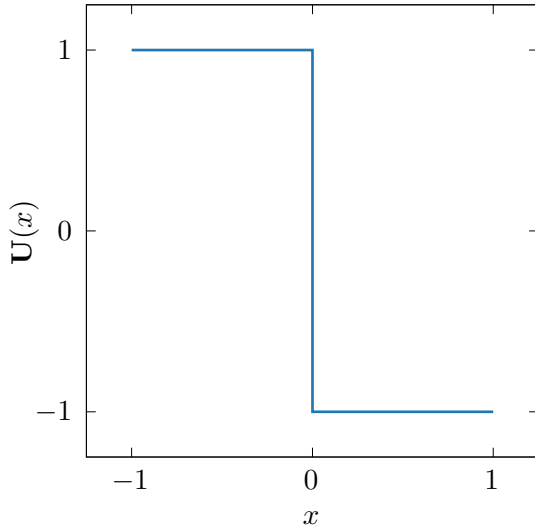


Figure 3.1: The initial conditions of a Riemann problem, where \mathbf{U} is a conserved variable.

3.1 The History & Mathematics of Numerical Simulations

The Euler equations are a specific case of the more general Navier-Stokes equations of fluid dynamics, covering the case of an inviscid fluid lacking thermal conductivity, these properties make the equations ideal for application to astrophysical fluids. At vast length scales the aggregate properties of a collection of molecules in near vacuum are essentially in-line with what is predicted by inviscid fluid dynamical equations; while the general lack of physical contact, both rare and fleeting, rules out the influence of thermal conduction and convection on the fluid at large. Astrophysical fluids at first appear strange and unintuitive compared to the more familiar fluid dynamics we have an almost innate understanding of as human beings; but if one zooms out enough and starts thinking in terms of parsecs and astronomical units, similarities begin to appear.

In a one-dimensional adiabatic case, with a fluid of density ρ , a velocity of u , a fluid pressure of P and a total energy, E , the Euler equations take the form:

3.1 The History & Mathematics of Numerical Simulations

$$\frac{\partial \rho}{\partial t} + \frac{\partial}{\partial x}(\rho u) = 0, \quad (3.1a)$$

$$\frac{\partial \rho u}{\partial t} + \frac{\partial}{\partial x}(\rho u^2 + P) = 0, \quad (3.1b)$$

$$\frac{\partial E}{\partial t} + \frac{\partial}{\partial x}[u(E + P)] = 0. \quad (3.1c)$$

As the Euler equations are a non-linear series of partial differential equations, no general analytical solution exists, to make it worse, numerical solutions aren't exactly easy either. The basest method of numerically solving such problems is Godunov's scheme (Godunov, 1959); this scheme is a finite-volume method wherein the problem is split into a series of cells, with a Riemann problem between the interfaces of each cell, an approximate solution to the Euler equations can then be made by solving all of these Riemann problems in sequence. This provides a first-order accurate approximation in a more general form, compared to the otherwise intractable set of PDEs. Whilst this piecewise method of solving many thousands of Riemann problems may provide a more generalised method of calculating fluid dynamics, performing it by hand would invoke a terrible strain on a mathematicians wrists. Godunov's scheme however, coincided with the burgeoning field of computer science,

Solving a higher-dimensional problem is a trivial extension to the original problem. In the 2-D case the number of interfaces increases to 4, with each interface being the analogous to each side of a square or rectangle, while in the 3-D case the interfaces can be thought of as the 6 faces of a cuboid. As such, the general formulation of the Euler equations becomes:

$$\frac{\partial \mathbf{U}}{\partial t} + \nabla \cdot [\mathbf{F}(\mathbf{U})] = 0, \quad (3.2)$$

where \mathbf{U} is a vector of conserved variables and $\mathbf{F}(\mathbf{U})$ is a vector of the corresponding fluxes of the conserved variables:

$$\mathbf{U} = \begin{bmatrix} \rho \\ \rho u \\ E \end{bmatrix}, \quad \mathbf{F}(\mathbf{U}) = \begin{bmatrix} \rho \mathbf{u} \\ \rho u \mathbf{u} + P \\ \mathbf{u}(E + P) \end{bmatrix}. \quad (3.3)$$

In practise however, solving higher-dimensional problems are significantly more computationally intensive, due to the increased number of interfaces and the drastically increased number of cells required to simulate the problem.

3. METHODOLOGY & NUMERICAL SIMULATION

Approximate methods were developed to account for the exact methods computational complexity, however early methods were less exact, and could not preserve the contact surface, these methods were also markedly less stable, limiting their effectiveness. The Harten-Lax-van Leer-Contact (HLLC) solver (Toro et al., 1994) is a commonly used approximate Riemann solver that has a similar order of accuracy and robustness to an exact solver while being markedly more efficient to solve.

Godunov's method is commonly used as a base for higher-order extensions, which employ methods to reconstruct the

Piecewise linear (van Leer, 1979)

The piecewise parabolic method solves (Colella & Woodward, 1984)

3.2 The Purpose of Numerical Simulations

Numerical simulation, thanks to its generalised but calculation-intensive approximation of partial differential equations, has an enormous range of uses, especially in the field of astrophysics. In particular, numerical simulation excels in modelling over large timescales and regions that are difficult or impossible to observe. The laws of physics have remained fairly consistent over the last 13.8 billion years¹, because of this we have managed to simulate the conditions of the early universe, showing the collapse of over-dense regions of the burgeoning universe into filaments and eventually galaxies provides our only continuous look into the long-term evolution of the universe, with deep-sky observations able to catch snapshots of these effects. Regions that undergo too much extinction or that are too distant to observe can be simulated, as a reasonable estimation of the initial system parameters can be made. Numerical simulation, in a sense, fills in the gaps and weaves together the many snapshots of the universe we can make from our lone vantage point in a more uneventful part of the cosmos.

This is of course not me screwing my simulationist hat firmly onto my head and claiming that theoretical methods of astrophysics are inherently superior. Whilst an immensely versatile and useful tool in an astrophysicists arsenal, numerical simulations are entirely reliant on the understanding of the laws of physics as we know them, as well as the skill of the programmer. If a simulationist gets too far into the weeds, wielding numerical simulations like a hammer, every astrophysical problem begins to look like a nail, which creates its own problems.

¹With some earlier exceptions.

3.2 The Purpose of Numerical Simulations

Colliding Wind Binaries in particular are a class of astrophysical phenomena that truly rely on numerical modelling in order to glean further understanding from them. The WCR is particularly difficult to observe, there is no nearby prototypical WCd system, meaning observation of fine-detail features requires extremely high angular resolution telescopes to begin with, this is compounded by the relatively small size of the region of the WCR where dust is rapidly produced. Whilst observing the large-scale structure of the WCR is possible with current telescopes, and clear observation of the surrounding dust cloud is possible (such as in the case of the recently discovered Callingham et al. (2019)), observing the dust producing region is markedly more difficult. In the typical case of a dust producing region 50 AU across embedded in a WCd system at a distance of 3,000 kpc an angular resolution greater than 30 μ as would be required to resolve the region, ruling out even the highest resolution instrumentation. As such, numerical simulation with a dust evolution model must be used to simulate the dust producing region, whilst the overall dust production rate from the simulation can be compared with observational estimates. This can be improved further, by the use of a radiative transfer model to model the dust production rate of the systems, however this was not feasible in the constraints of this projects timescale, but could be performed as a follow-up project.

It is a shame that CWB systems are difficult to *simulate* as well!

Numerical simulations can be vastly simplified by reducing the number of dimensions in the simulation, single object systems can be typically reduced to a 1-D spherically symmetric or 2-D cylindrically axisymmetric simulation, in the case of supernovae or jets, for instance. In the case of a CWB system with orbits however no dimensions can be reduced, a single dimension simulation will not simulate the WCR, while a 2-D axisymmetric simulation will not properly simulate the effect of orbital motion, which as we observe, is essential to determine the morphology of a WCd system. In addition to this, in order to see how dust evolves over the large length-scales of the WCR requires very large simulation domains, while accurately resolving the apex of the WCR requires a fairly high number of cells between the stars in the system (this was found to be approximately 100 cells for a typical system). The combination of these two factors is quite terrible, as the simulation is both 3-D and requires an extremely large effective resolution, enough to tax even the most capable of our available compute resources. Fortunately, mesh refinement techniques can improve this situation by drastically reducing the number of cells that need processing, simplifying our problem from “*impossibly intensive*” to “*extremely intensive*”.

3. METHODOLOGY & NUMERICAL SIMULATION

3.3 Computational Hydrodynamics

3.3.1 Comparison of hydrodynamical methods

3.3.2 The MG hydrodynamical code

The MG hydrodynamical code was utilised at the start of the project, as problem generators for CWB systems had already been written, while also being fairly well understood throughout the department. MG is a relatively easy to use hydrodynamics code many of the required features for this project, it is fairly extensible and supports MPI and AMR for fast and effective numerical simulation, it was initially estimated that this would take a little more than a year to implement the dust model, cooling models, and be on our way to running large-scale simulations – how wrong we were.

Unfortunately, the crux of the project – the advected scalar dust model – never adequately worked, either producing dust rates measurable in grams per year, or the simulation rapidly converting remapped wind into dust, despite it being too hot to do so according to our dust model. Attempts to implement the dust model through modification of the conserved variables or through a rate-based source function were made, with many different implementation attempts, none of these panned out, unfortunately, resulting in a large amount of work being discarded. Using strict constraints to prevent rigorous dust production resulted in strange looking systems, that did not behave as observations suggested. Furthermore, building a model that relies on dozens of constraints based on limited empirical data is rarely a good model, and is a bit like building a clock that doesn't move at all, so that it is at the very least right twice a day.

In addition to incompatibility with the dust model, numerous technical issues compounded this work. Mapping the wind onto the CWB also proved difficult when combined with AMR, as the provided implementation of wind remapping required a circular region with a radius of 3 coarse cells. In order to get the required separation for systems with close orbits, a very high coarse resolution would be required, massively increasing memory usage. using a source function for wind mapping allowed for more refined cells to be used, but this could also produce artefacts at level transitions, while also producing extremely hot winds as the temperature could not be correctly defined.

In general, while being very extensible in terms of being able to implement a problem generator fairly easily, low-level manipulation of the code was found to be extremely difficult due to

limited documentation and a complex, linked-list mesh structure. As such, writing workarounds and fixes to the issues described was very time-consuming, slowing progress in the project significantly. Compounding on this, iteration time was extremely long, requiring multiple hours to run a simulation to determine if the fixes worked, debugging was rendered difficult by the use of OpenMPI, and the general structure of the code rendered the setting of breakpoints difficult even in the single-threaded case. Finally, the numerical integrator was found to not be particularly stable in the face of extremely radiative cooling environments, complex multi-step cooling processes were considered and implemented, but even these could not handle such rapid cooling without breakdown if a reasonable Courant number was to be used. The solution was to artificially limit cooling to a fraction of the energy in the cell per timestep, however this reduces the simulation accuracy, and results in much slower cooling within the post-shock WCR¹.

In the end, the decision was made to switch from `MG` to the new `Athena++` hydrodynamical code. This decision was made in mid-2020, by the end of 2020 the problem generators were build, the necessary modification to the underlying code of `Athena++` were completed and the dust model was fully implemented.

3.4 The `Athena++` hydrodynamical code

The `Athena++`² hydrodynamical code was found to be a much more suitable fit for this project. `Athena++` is a total re-write of the older Athena MHD code in C++ with a focus on implementing Adaptive Mesh Refinement, source code clarity, modularity, and generally improved performance (Stone et al., 2020). This clarity and modularity allowed us to port over our dust model from `MG` to `Athena++` in a few months. This modularity is best exemplified by the use of “problem generators” to define a specific hydrodynamical problem. A problem generator is a C++ file that is included at compile-time, containing the initialisation conditions, run-time functions, source terms and refinement conditions needed to generate and simulate a hydrodynamical problem. As problem generator is defined at compile-time this ensures that only the required problem files are included in compilation, preventing any accidental overloading of function names or

¹I understand, reader, that this section reads like a series of complaints... This is because it is. I recommend that you humour me, as attempting to debug `MG` ate up more than two years of my life and was the direct cause of many, *many* sleepless nights. Thankfully this is the last time we will ever speak of it, unless you and I share a pint or two at a local pub.

²<https://github.com/PrincetonUniversity/athena>

3. METHODOLOGY & NUMERICAL SIMULATION

Integrator	Elapsed Time	Relative Time	τ_f
<code>rk3</code>	1,444.6 s	100.0%	5.467×10^5 s
<code>ssprk5_4</code>	2,352.4 s	163.1%	5.542×10^5 s

Table 3.1: Time elapsed

compiler issues. This also allows for switching between different versions of a problem without complication, requiring only a quick reconfiguration and recompilation to change problem.

Multiple time-integration and spatial reconstruction methods have been implemented into **Athena++**, which requires essentially zero modification on the user’s end, a startling revelation coming from other numerical codes. Time-integration method vary from a computationally simple 2nd order van Leer (van Leer, 1979) method to strong stability preserving methods (Ruuth & Spiteri, 2005) to super time-stepping Runge-Kutta-Legendre (Meyer et al., 2014) methods; changing of the time-integration method can be implemented without recompilation, and can even be changed upon restart of an in-progress simulation, which was found to be useful for if a simulation was having trouble running at a certain point. **Athena++** must be recompiled for the specific spatial reconstruction method, as the number of overlapping “ghost” cells needs to be defined at compile-time. In this project, either the 3rd order accurate strong stability preserving Runge-Kutta method (`rk3`) or the 4th order accurate, five-stage, 3 register, SSPRK method was utilised (`ssprk5_4`), depending on the instability of the simulation. The `rk3` method was found to be more than twice as fast as the `ssprk5_4` method in the case of a CWB system, though could crash in the cases of rapid cooling and dust production, if a simulation crashed multiple times the simulation would be altered to use `ssprk5_4`. The Riemann solver can also be changed at compile-time, however this was left to the default solver, the Harten-Lax-van Leer-Contact (HLLC) solver (Toro et al., 1994).

One of the reasons outside of stability for choosing **Athena++** was its very high parallel performance, the problem is divided into a regular array of sub-volumes containing $X \times Y \times Z$ cells. This array, referred to as a “meshblock” is then distributed to a processing node available to the programme to calculate the next time-step. The meshblocks are encoded in a tree structure, in the 3D case an octree (Stone et al., 2020), as the relationship between parent and child blocks must be preserved for mesh refinement to work. This is in comparison to the linked-list method of distribution which is used in **MG**, which is not performant in distributed multiprocessing systems such as **ARC**, as this can result in lots of communication of relatively small packets between nodes as a time-step is being calculated, reducing performance significantly due to

3.4 The `Athena++` hydrodynamical code

bandwidth and latency constraints. This meshblock system does have is drawbacks, however, time-stepping is synchronous, and bound to the width of the lowest level, this is not the case in MG, where multiple sub-steps are performed on lower levels, which are processed first, with the coarsest levels running on a single step. This method is much faster but can result in significant divergence from a synchronous method. Whilst a synchronous timestep can be slower in some cases, in the case of a simulation with hypersonic winds and rapid cooling a small time-step would typically need to occur anyway.

`Athena++` is highly parallel and utilises the OpenMP and OpenMPI software libraries in order¹. In the case of a simulation that requires more cores than a single computer can provide, OpenMPI is used to distribute meshblocks between nodes in a HPC² cluster, whilst this can introduce bottlenecks due to the comparatively slow networking between nodes, this allows for thousands of cores to be used, rather than dozens.

In order to prevent numerical errors from occurring between the interfaces between meshblocks, “ghost cells”, cells from adjacent meshblocks copied into the current meshblock, are used. In this work, the two outermost layers of cells in a meshblock are distributed along with the adjacent meshblocks to processing nodes, which represents a substantial memory saving compared to the all processing nodes having the entire problem stored in memory. In our case, using `Athena++` with the ARC4 HPC was found to be performant up to 192 cores, with diminishing returns with additional cores. Typically, 128 cores were used for each simulation, as this represented a good trade-off in processing throughput and node availability, as ARC4 is a heavily utilised resource. Calculating the parallel fraction of `Athena++` using a distributed computing cluster such as ARC4 proved to be difficult, as node locations in the network could not be taken into account. A fork of `Athena++` that utilises GPGPU acceleration has been developed, and boasts an even higher performance compared to the more traditional CPU bound `Athena++`, however, this was not used due to the scarcity of GPGPU compute nodes in ARC (Grete et al., 2020).

¹Sadly, the engineers at Intel who worked on the Netburst architecture were [wrong](#), processors can't easily scale up to dozens of GHz, instead, multiple cores have to be used, making high performance code that much harder to write.

²High Performance Compute

3. METHODOLOGY & NUMERICAL SIMULATION

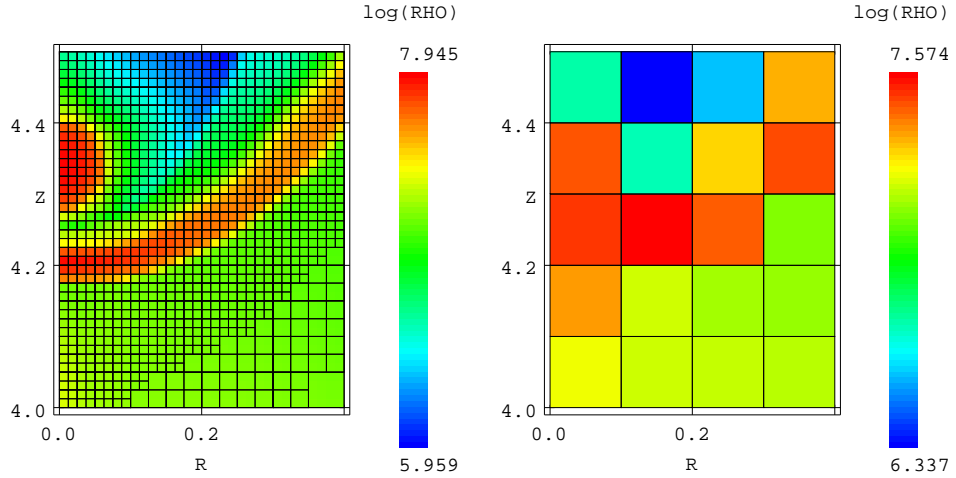


Figure 3.2: An example of adaptive mesh refinement in the MG hydrodynamical code around the OB star in a colliding wind binary problem using cylindrically symmetric co-ordinates. With AMR the WCR is properly resolved, while without the system cannot adequately resolve the WCR.

3.5 Mesh Refinement

One of the problems previously discussed with modelling CWB systems is the wide range of length scales needed to appropriately simulate a system, the total dust production region can cover dozens of AU, while the WCR in order to be properly resolved needs to have a feature size between 3 and 4 orders of magnitude smaller than that. Coupled with the requirement for a 3-D model if orbits are to be considered and suddenly you find yourself looking at a simulation with a resolution with 10^9 cells or higher. In order to remain compliant with the Courant-Friedrichs-Lowy condition, the associated timestep must also be reduced, increasing the amount of computations in accordance with a fourth dimension. In the case of the more ambitious simulations in this project, a region approximately 1,000 AU was defined, with an effective resolution of approximately 1.07×10^{12} cells; this sheer amount of data would be difficult to store, let alone compute, and would be far beyond the capabilities of any HPC service available to this project.

In order to resolve this resolution issue, using cells more effectively than brute-force increasing the resolution must be performed, as such, algorithms such as Adaptive Mesh Refinement (AMR) were introduced to the field of numerics with almost immediate uptake. AMR is a flexible method of mesh refinement, first discussed by Berger and Oliger (1984) and expanded upon by Berger and Colella (1989). This method starts with a “coarse” grid at the lowest defined resolution, and

tests each cell against a series of conditions, such as proximity to an object in the simulation, conserved parameter or truncation error; if the cell passes any of these threshold conditions it is flagged for refinement. At the end of a simulation step, the AMR algorithm will split the cell in half along each axis, increasing the effective resolution of the cell. Conversely, a region can be flagged for de-refinement, where the cells are merged together again, if a condition was transient and is no longer being passed. Figure 3.2 shows this effect, the application of mesh refinement greatly increasing the resolution of the WCR, allowing for the space between the star and the WCR to be properly resolved, which is crucial for the physically accurate simulation of the CWB.

The benefit of this refinement on systems with only small regions requiring high resolutions is immediately apparent. In the case of the previously described system with 1.07×10^{12} cells, naively refining a region around 1.5 times the orbital separation from the barycentre with 7 refinement levels reduced the number of cells in the simulation to 1.55×10^6 cells, a 6 order of magnitude reduction in cell count and memory usage. Care must be taken, however, not to over-refine the simulation or to rapidly refine and de-refine a region. The former can be mitigated by defining a maximum refinement level, while the latter can be mitigated by defining a minimum number of timesteps required for a cell to be repeatedly flagged for refinement and de-refinement. Another issue with this method is multiple refinements per timestep for a cell, which can render the simulation unstable.

In the case of **Athena++** meshblocks are instead refined or de-refined, whilst this improves multi-threaded performance with multiple CPUs as it reduces the amount of communication required between processor nodes, this method does increase memory requirements, and is not optimal in an idealised case. Though, as these simulations are being performed on an HPC cluster this is optimal for our case. Unfortunately, despite the advantages of AMR over SMR, there is a known issue with [Athena++¹](#) which prevents the use of AMR with passive scalars enabled, scalar values are not conserved properly around meshblock interfaces, which can rapidly escalate and result in physical inaccuracy and breakdown of the simulation. As there was ultimately no time to correct this bug, the decision was made to persist with using Static Mesh Refinement (SMR) for the second papers work, despite a version of the code already being written with AMR in mind.

Static Mesh Refinement operates by refining regions defined in the problem config file or

¹<https://github.com/PrincetonUniversity/athena/issues/365>

3. METHODOLOGY & NUMERICAL SIMULATION

code that can be refined to a higher resolution, which will progressively de-refine beyond this region until the coarse level is reached. Whilst markedly less flexible, this is still particularly useful for simulations where the resolution requirements remain approximately in the same place spatially. In the case of CWB systems this is a reasonably good approximation, as the region around the orbit of the stars can be refined to a higher resolution, while progressively de-refining further out from the barycentre. Due to the comparatively low flexibility of AMR in a block-based hydrodynamical code such as `Athena++`, this was a preferable alternative to refactoring our model to work in either `MG` or a different numerical code such as `Enzo`.

3.6 Datatypes & visualisation

`Athena++` exports data in a number of data formats, from formatted tables, to VTK files (Schroeder et al., 2006) to the Hierarchical Data Format standard (HDF5) (The HDF Group, 1997–2022). For all numerical grids being exported, the HDF5 standard was used as it was easily the most flexible. In particular, HDF5 has native support for MPI parallelised I/O, which negates the need for writing out individual files for the data for each processing node, and generally has a much greater throughput. A separate, comma-delimited “history” filetype was used to store summated values of conserved variables and advected scalars, this was used primarily to determine simulation-wide dust production rates and average grain sizes as the simulation evolved. The `Athena++` input file syntax allows the user to define multiple outputs to be written at a certain elapsed simulation times, as well as periodically writing “checkpoint” files for the simulation to resume from. For most simulations, this was performed every fraction of an orbit, with checkpoint files and 3D datasets being written every 1/100th of an orbit, and 2D datasets and “history” file updates being written every 1/1000th of an orbit.

Data was plotted using a series of custom programmes designed to parse data as quickly as possible, the Python 3.8 (Van Rossum & Drake, 2009) plotting library provided in the `Athena++` repository was modified to incorporate Delaunay triangulation, instead of interpolating static meshes to the finest level in order to operate correctly with Matplotlib (Hunter, 2007), data-points are triangulated with each other. This is a markedly more memory and processing efficient method, as data is not duplicated or smoothed at the interpolation step, and was found to be approximately 2000% faster. Whilst this can result in artefacts at low resolutions, the resolution of the simulation was sufficient such that these artefacts were not observed. The GNU Parallel library was used to batch-process 2D exports (Tange, 2021), as Python is for the most part

single threaded and interpreted it was found to be more effective use Parallel to run multiple python instances at once, each processing a single data file using the command:

```
1 seq 0 <max> | parallel -j44 "athena_plot.py plot-config.yaml -n {}"
```

where `<max>` is the number of simulation files. The `Numba` library (Lam et al., 2015) was also used to improve performance by JIT¹ compiling, parallelising and vectorising certain steps that were not performant in either Python or Numpy (Harris et al., 2020). In this case, `Numba` was used to restructure numerical array data into a linear series of arrays, performing derived parameter such as dust density and temperature calculations, and matrix co-ordinate transforms. While this is less straightforward to implement, as many of Python's data-types cannot be used, this offered a 2 order of magnitude processing speed increase in the case of an 8-core workstation.

For 3D visualisation the `VisIt` application is used (Childs et al., 2012). However for print 2D slices generated using `Matplotlib` were used. The `Gnuplot` utility (T. Williams et al., 2020) was used for generating line and scatter plots throughout this thesis, in particular history outputs from `Athena++`. Occasionally, rendering video of the batch processes 2D exports was performed in order to better understand how the systems propagated over time, in order to do this `ffmpeg` library (Tomar, 2006) was used to render the videos. For this, the following command was used:

```
1 cat /*.png | ffmpeg -f image2pipe -framerate 30 -i - -c:v libx264 -vf format=yuv420p output.mp4
```

3.7 Simulating CWB systems

3.7.1 Assumptions

Another assumption is that the outflow from each star is rapidly accelerated to the stars wind terminal velocity, v^∞ . This negates the need for simulating radiative line driving effects on the stellar wind, or calculating the CAK parameters for each wind, however this can result in over-estimation of the wind collision velocity if the wind momentum is sufficiently imbalanced, and the apex of the WCR is close to the secondary star. If the wind velocity is sufficiently reduced this can effect the structure of the wind collision region, as the wind momentum ratio and cooling parameter will be changed. Additional factors such as sudden radiative braking can also effect the primary star, where in the case of an extremely unbalanced wind, the primary stellar

¹Just In Time.

3. METHODOLOGY & NUMERICAL SIMULATION

wind can become rapidly decelerated as it approaches the secondary star and its radiative flux is more influential than the driving force of the parent star (Gayley et al., 1997). This should be considered when analysing the results of each simulation, and understanding how the secondary wind velocity can effect the cooling and dust production rate of the WCR.

3.7.2 Wind propagation & refinement

As there are only two gravitationally interacting bodies in the system, it was deemed unnecessary to implement a more complex n-body gravitational system to model the dynamics of the stars. Additionally, calculating the radial velocity at the start of the simulation would be required, all of which is not needed in the case of a Keplerian orbit simulation. As the orbital path of the system is already known, this also allowed the use of a “phase offset” to change the starting point of each simulation, such as in the case of the WR140 simulation, which begins at $\phi = 0.95$.

With the assumption that winds are rapidly accelerated to v^∞ , propagating stellar winds through a simulation has been drastically simplified. In the simulation, the conserved variables inside a small spherical region 6 fine cells in radius are modified in order to inherent the parameters of a stellar outflow, with a mass loss rate of \dot{M} and a wind velocity of v_∞ radially outwards from the star. The conserved variables, correspond to:

$$\rho_R = \frac{\dot{M}}{4\pi r^2 v_\infty}, \quad (3.4a)$$

$$P_R = \rho_R v_\infty^*, \quad (3.4b)$$

$$E_R = \frac{P_R}{\gamma - 1} + \frac{1}{2} \rho_R v_\infty^2, \quad (3.4c)$$

where r is the radial distance from the star, P_R is the cell pressure, and γ is the ratio of specific heats, typically 5/3. Whilst this method is very fast and effective, it requires the remap region to remain completely undisturbed, if the WCR impinges upon the remap region this will result in significant physical inaccuracy. In order to mitigate this, it was found that there should be 75 – 120 fine cells separating the stars, for a system with $\eta \sim 0.01$. For systems with a WCR closer to the secondary star the number of cells should be significantly increased.

Throughout this thesis SMR is used to increase the effective resolution of simulations, a box around the CWB orbit is refined to the highest level defined in the simulations input file,

`Athena++` de-refines the cells gradually around this box until the simulation is at its coarsest resolution.

3.7.3 Cooling in numerical simulations

As discussed in section 2.3.3, there are many cooling processes that need to be considered when simulating a complex system such as a CWB.

Sufficient cooling is in fact, essential to this dust formation process. Gas temperature in the immediate post-shock region can exceed 10^8 K , far beyond the temperatures required to adequately form dust, as any nascent grains would quickly be shattered by thermal processes. There is sufficient evidence to suggest that significant, rapid temperature loss occurs in the post-shock regime, the high metallicity of the WC wind and high number density of atoms and ions makes it the ideal region for rapid cooling due to radiative processes.

Another boundary to dust formation due to an insufficiently radiative post-shock flow is a lack of sufficient downstream density. In the case of strong, adiabatic shocks, constraints are set on the downstream gas parameters of the system, such that:

$$u_b = \frac{1}{4}u_a, \quad (3.5a)$$

$$\rho_b = 4\rho_a, \quad (3.5b)$$

$$P_b = \frac{3}{4}\rho_a u_a^2, \quad (3.5c)$$

where a is the upstream side and b is the downstream, post-shock side. As the gas density can only be a factor of 4 larger than the post-shock flow, the post shock density (even if it were at temperatures suitable for dust formation) is insufficiently dense for sufficient dust production. However, in a radiative shock behaving isothermally (where the temperature change, ΔT throughout the entire lifespan of the fluid is equal to zero), the final density, ρ_f can be approximated to:

$$\rho_f \approx \gamma M_a^2 \rho_a, \quad (3.6)$$

where M_a is the pre-shock mach number. For a shock with an initial sound speed of $M_a = 100$ the final density can exceed the pre-shock density by a factor of 10^4 !

3. METHODOLOGY & NUMERICAL SIMULATION

Performing radiative cooling within a numerical simulation is computationally difficult, and trade-offs between accuracy and performance must be considered at every step of designing the simulation, as every single cell must undergo cooling. For this project, the final cooling can be out by a few percent at worst, but is fast enough to run the simulations in a reasonable amount of time without excessive memory requirements. In order to simplify the radiation calculations, radiation does not re-interact with the simulation, instead it is completely removed from the simulation. Due to this, scattering, re-adsorption and radiative transfer are not simulated at all.¹. Other methods of reducing computational cost and optimising the code are used in this project, and will be described in detail in this section.

Plasma cooling

Thus, instead of calculating the emissivity of the plasma for the current density, temperature and abundances, a lookup table is pre-calculated and loaded into the simulation at runtime. These lookup tables are generated by combining a series of lookup tables generated for pure flows of elements, and combined based on the abundance of the element within the stellar wind, hence each star in the simulation has its own unique lookup table. A typical lookup table in this project utilises logarithmically spaced temperature bins from 10^4 K to 10^9 K, with 100 bins in total, if the calculated temperature is between bins a linear interpolation step is used to improve the accuracy of the the emissivity solution. In order to calculate the energy loss within a cell, the following formulae is used:

$$\frac{dE}{dt} = \left(\frac{\rho}{m_H} \right) \Lambda_w(T), \quad (3.7)$$

where $\Lambda_w(T)$ is the normalised emissivity at the cell temperature, T. This solution is orders of magnitude faster than performing an emissivity calculation in every cell, and is essential to performing fast hydrodynamical simulations with plasma radiative cooling.

Other optimisations relied on replacing a naïve linear search with an indexing method that relied on the logarithmic spacing of the temperature bins, instead of performing a search the index, n , of the emissivity value stored in an array can be calculated using the formulae

¹If these are considered, your programme is now a ray-tracing programme as well as a hydrodynamical code, which is its own, even more complicated field.

$$n = \left\lfloor \frac{\log(T) - \log(T)_{\min}}{\delta \log(T)} \right\rfloor, \quad (3.8)$$

where $\log(T)$ is the log of the cell temperature, $\log(T)_{\min}$ is the minimum log temperature in the lookup table and $\delta \log(T)$ is the log spacing of the temperature bins. This speed-up is fairly significant as the average search performance changes from $\mathcal{O}(n)$ to $\mathcal{O}(1)$ time, a marked improvement over even a binary search, which would resolve in an average of $\mathcal{O}(\log n)$ time. In the case of a 100 bin array this is only a minor speed-up, but with the sheer number of calculations being performed, any optimisation to a function used multiple times per cell can significantly improve performance. In the case of larger, or multi-parameter lookup tables this method would only improve in performance, and is a good example of general optimisation in a numerics programme.

In order to integrate the energy loss rate to determine the exact amount of energy lost within a timestep, an integration method needs to be chosen, for this project, a fast, first-order Euler method with multiple sub-steps was chosen. Whilst this method is not particularly accurate or robust, it was found to be fast, and the adaptive sub-step method was found to calculate a reasonably accurate approximation of a cells change in temperature in a very small amount of time. This sub-step method is elaborated on in section 3.7.4.

Other methods of refining the emissivity value were also considered, such as fitting a local curve to the data or using a spline-based interpolation step instead of a linear step, however these were only marginally more accurate, at a significantly increased calculation time. An exact cooling method was also considered, which was found to be significantly more performant, but had a series of limitations that prevented it from being used in the codebase at this time. This exact cooling method, described by Townsend (2009), introduces a temporal evolution function (TEF), $Y(T)$, into the solution, which describes a measure of the total time required to cool from an arbitrary temperature to T . This function, as well as its inverse, need to be calculated prior to cooling being calculated, but do not have to be calculated for every cell and timestep, while solving the TEF for the cell temperature takes approximately the same amount of time as a single first order Euler method integration, whilst offering an *exact* calculation of the post-step temperature. This scheme is one of the rare example of a numerical method that is both accurate *and* fast, taking approximately the same time as a second order explicit method overall, whilst also being perfectly accurate even in highly radiative hypersonic flows. Unfortunately this method has a number of limitations that precluded its usage in this project. First, this method

3. METHODOLOGY & NUMERICAL SIMULATION

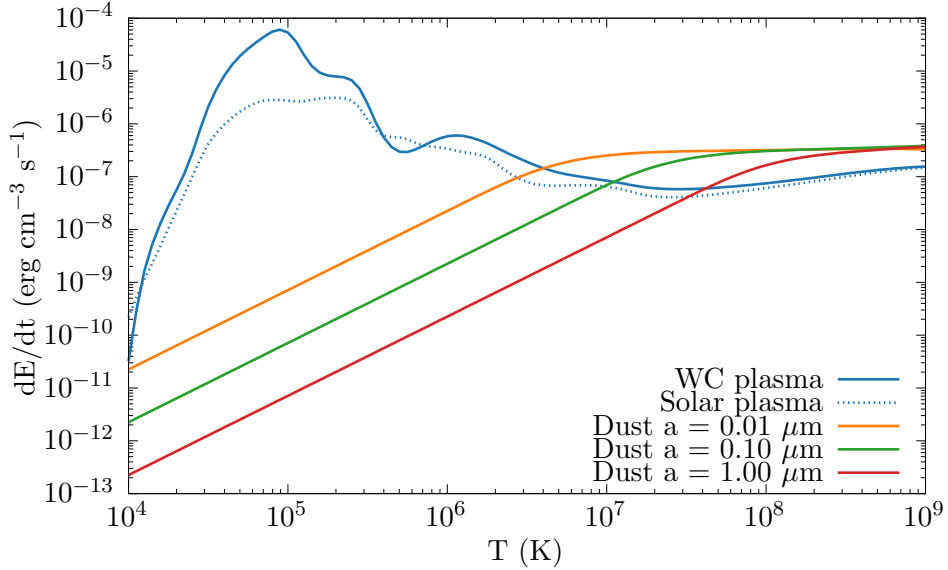


Figure 3.3: Comparison of energy loss due to plasma & dust cooling with varying grain sizes in a typical post-shock flow, where $\rho_g = 10^{-16} \text{ g cm}^{-3}$ and a dust-to-gas mass ratio of 10^{-4} . Whilst less influential at lower temperatures, dust cooling can aid cooling in the immediate post-shock environment.

would not have been able to accurately model mixed wind situations, hampering its usage cooling winds with drastically different abundances. Second, and most importantly, dust cooling could not have been modelled with this single parameter TEF method, which would have required using a two stage cooling method, as the gas temperature would not be synchronised between stages, this would have resulted in a highly inaccurate cooling solution, obviating the advantages of the exact cooling method.

Dust cooling

Dust cooling

In the case of the immediate post-shock environment where dust is present in the form of small, rarefied nascent grains, the cooling rate is greater than the plasma cooling rate due to bremsstrahlung, as seen in figure 3.3. As such, it is assumed that dust cooling plays an initial role in the initial cooling of the post-shock flow in colliding wind binaries, and should ideally be included.

Whilst a lookup table has proven to be adequate for plasma cooling, dust cooling for a given stellar wind is markedly more difficult to solve. Whilst emissivity due to radiative processes in a

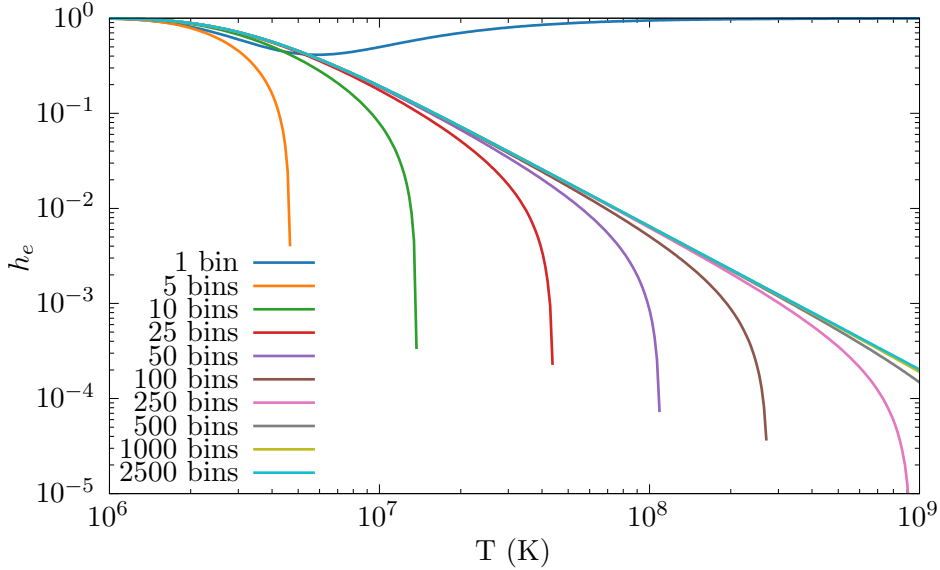


Figure 3.4: Comparison of h_e as a function of temperature for dust grains with a radius of 0.005 μm , h_e is calculated via the trapezium rule with a varying number of bins, bin counts below 400 bins result in wildly inaccurate or in some case negative values for h_e , while beyond 400 bins the result is accurate and converges slowly.

gas or plasma can be parametrised in terms of temperature assuming that the flow abundances remain the same, the same does not apply to dust cooling, which requires three parameters, the grain radius, density and temperature. Calculating emissivity due to dust is a markedly simpler proposition than calculating plasma emissivity, and could be performed quickly within a hydrodynamical code if only grain-atom interactions are considered. Grain-electron interactions are a markedly more complex proposition.

The complexity in grain-electron interactions lies in determining the electron transparency, h_e , which is the probability that an electron will embed in the dust grain and heat it, rather than pass through. h_e can be computed via integration by parts, however due to this occurring in the main cooling loop, this results in a nesting of integrals, which can lead to extremely time-consuming computation for individual cells. The integral could be simplified by reducing the number of bins to integrate with, however below approximately 400 bins the results can become extremely inaccurate, resulting in incorrect or even *negative* values for h_e . More complex integration methods reduce the number of steps required, but are in themselves more time consuming to calculate, leading to the same issue. Initial tests using the integral method within a numerical simulation led to severe slowdown as processing time for cooling took up to 90% of the overall processing time for each timestep. The effect on grain heating due to electron

3. METHODOLOGY & NUMERICAL SIMULATION

interactions cannot be discounted, as it can be up to an order magnitude greater than grain heating due to incident atoms. This was considered to be unacceptable in terms of performance, and as such a faster method needed to be determined.

Multiple options were considered for improving the performance of this routine. Initially, a Λ_d lookup table was considered, this consisted of a logarithmically spaced table of ρ , a , T and Λ_d values calculated by an implementation of the Dwek and Werner, 1981 prescription. A binary search for each parameter is performed, with the an offset, P_d , being calculated for each parameter,

$$P_d = \frac{P - P_0}{P_1 - P_0}, \quad (3.9)$$

these offsets are then used to perform a trilinear interpolation to calculate λ_d from the lookup table.

$$\begin{aligned} \Lambda_{00} &= \Lambda_{000} (1 - \rho_d) + \Lambda_{100}\rho_d, \\ \Lambda_{01} &= \Lambda_{001} (1 - \rho_d) + \Lambda_{101}\rho_d, \\ \Lambda_{10} &= \Lambda_{010} (1 - \rho_d) + \Lambda_{110}\rho_d, \\ \Lambda_{11} &= \Lambda_{011} (1 - \rho_d) + \Lambda_{111}\rho_d, \\ \Lambda_0 &= \Lambda_{00} (1 - a_d) + \Lambda_{10}a_d, \\ \Lambda_1 &= \Lambda_{01} (1 - a_d) + \Lambda_{11}a_d, \\ \Lambda &= \Lambda_0 (1 - T_d) + \Lambda_1 T, \end{aligned} \quad (3.10)$$

where 0 is the lookup table value lower than the parameters actual value, and 1 is the lookup table value greater than the parameters actual value. This implementation was written in the form of a series of nested loops to utilise SIMD vectorisation to improve performance.

Whilst this method is significantly faster than calculating Λ for each cell with an integration step, a $(100 \times 100 \times 100)$ lookup table requires approximately 32 MB of memory to store, and is much more time consuming to search through. As such, eliminating complexity from the binary search and reducing the number of interpolations were identified as improvements to the These optimisations were made by simplifying the lookup table into a series of smaller lookup tables and relying on even logarithmic spacing of the lookup table to determine the parameter indices, rather than performing a binary search for them. Additionally, as ρ and a are invariant within

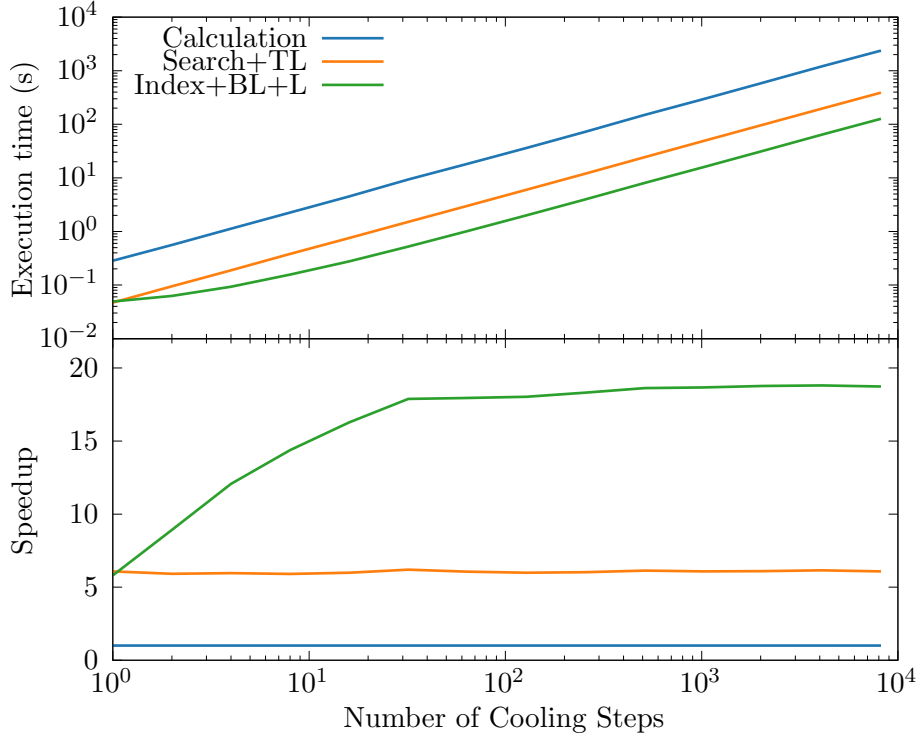


Figure 3.5: Comparison of execution time and speedup for lookup table methods.

the cooling loop, these parameter offsets are solved separately using a bilinear interpolation, while in the cooling sub-step loop, a separate linear offset is performed to find the temperature offset, solving to find Λ_d . These optimisations resulted in this method scaling significantly better, as there is a lower total number of calculations required as the number of sub-steps increases (figure 3.5).

The second method considered for solving the h_e integral was using an approximation described by Dwek and Werner, 1981 where h_e could be described by a series of equations:

$$\begin{aligned}
 h_e(x^*) &= 1, & x^* > 4.5, \\
 &= 0.37x^{*0.62}, & x^* > 1.5, \\
 &= 0.27x^{*1.50}, & \text{otherwise,}
 \end{aligned} \tag{3.11}$$

where $x^* = 2.71 \times 10^8 a^{2/3}(\mu\text{m})/T$. Whilst this is less accurate, especially in the region where one case ends and the other begins where the result begins to diverge, this method is multiple orders of magnitude faster. Figure 3.6 shows these discrepancies, in the case where electron

3. METHODOLOGY & NUMERICAL SIMULATION

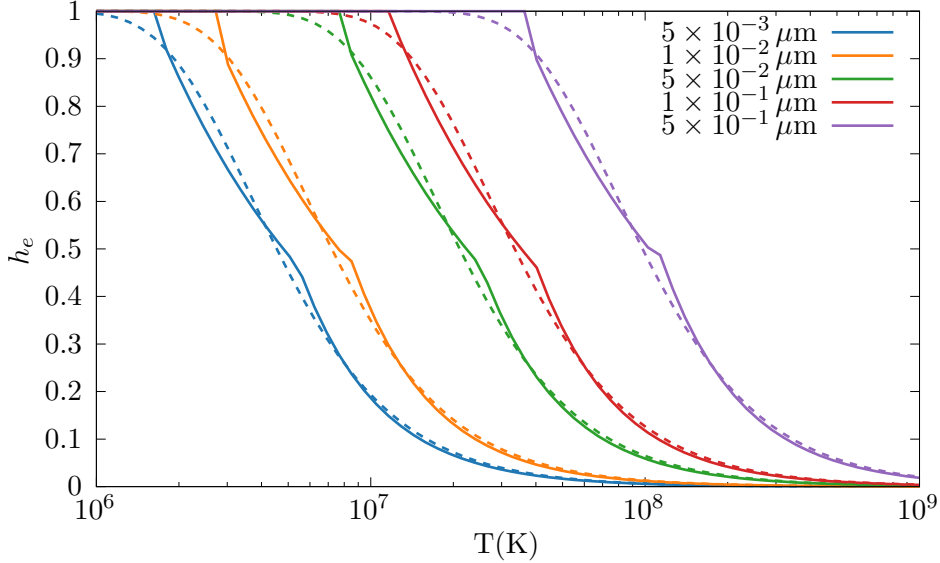


Figure 3.6: Grain transparency as a function of temperature for the estimate method described in equation 3.11 (solid lines) and a 400 bin integration method (dashed lines).

Method	t(s)	Iter/s	Speedup
400 bin integration by parts	36.03	35,526	-
Binary search + trilinear	6.016	212,751	599%
Index calculation + bilinear + linear	1.999	640,447	1,803%
Dwek and Werner, 1981 approximation	0.147	8,693,171	24,510%

Table 3.2: Comparison of methods explored for estimating $\Lambda_d(\rho, a, T)$ in cooling code, 10^4 initial values were chosen and 128 cooling sub-steps were performed, benchmark code was compiled and run using `GCC 10.3.0` with the `-O3` optimisation set on an Intel i7-7700HQ processor with a maximum clock speed of 3.8 GHz.

transparency begins to decrease the approximation is out somewhat significantly, as well as mid-way through the curve, whilst at temperatures below 10^6 K the approximation and integral methods are perfectly aligned. As the grains grow hotter and the electron transparency reduces, the influence on the cooling rate due to incident electrons reduces quite drastically, meaning that extremely high accuracy is less important at these temperatures (figure 3.7). The accuracy of the approximation method is also shown in figure 3.8, the estimated value for Λ_d closely matches the integrated value aside from the smallest dust grains at very high temperatures $T > 6 \times 10^8$ K.

Table 3.2 shows the improvements to performance inherent in the estimation method; the final result is that the approximation is over 24,500% faster, the resulting dust cooling function therefore will have a minimal computational impact on the cooling loop as a whole. As this approximation was conclusively shown to not significantly effect the cooling rate due to grain

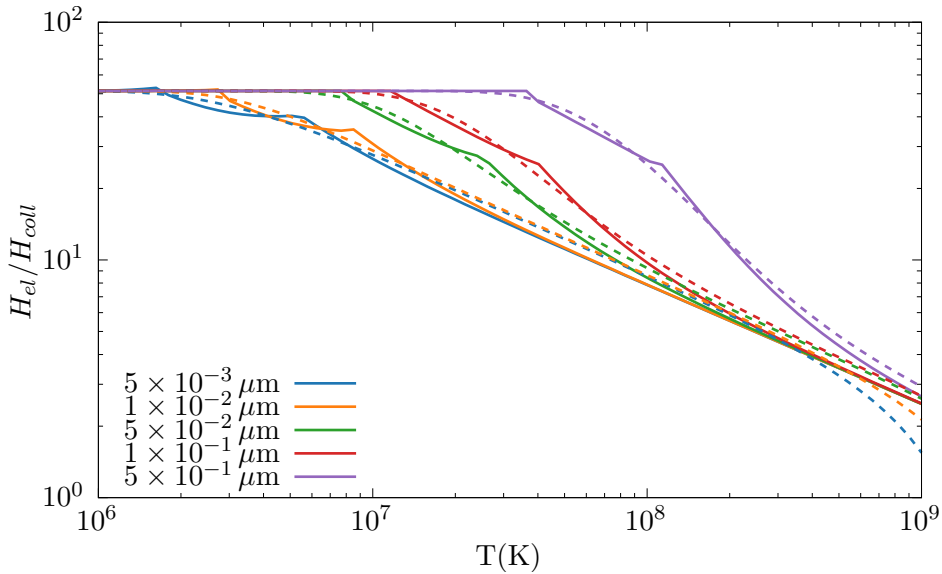


Figure 3.7: Comparison of the ratio heating rate of a dust grain due to incident electrons and incident atoms as a function of temperature for various grain sizes, whilst the result between the integration method and estimate method diverge, this is while the contribution of heating from electrons becomes less influential on the cooling rate of the grain.

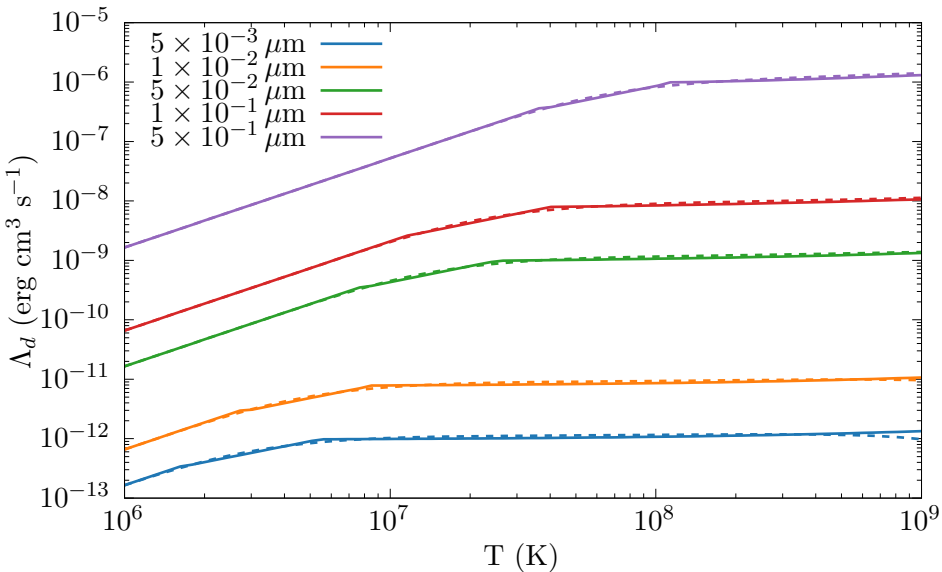


Figure 3.8: Λ_d as a function of temperature for various grain sizes, the estimate method is extremely close to the integral value aside from at the highest temperatures.

3. METHODOLOGY & NUMERICAL SIMULATION

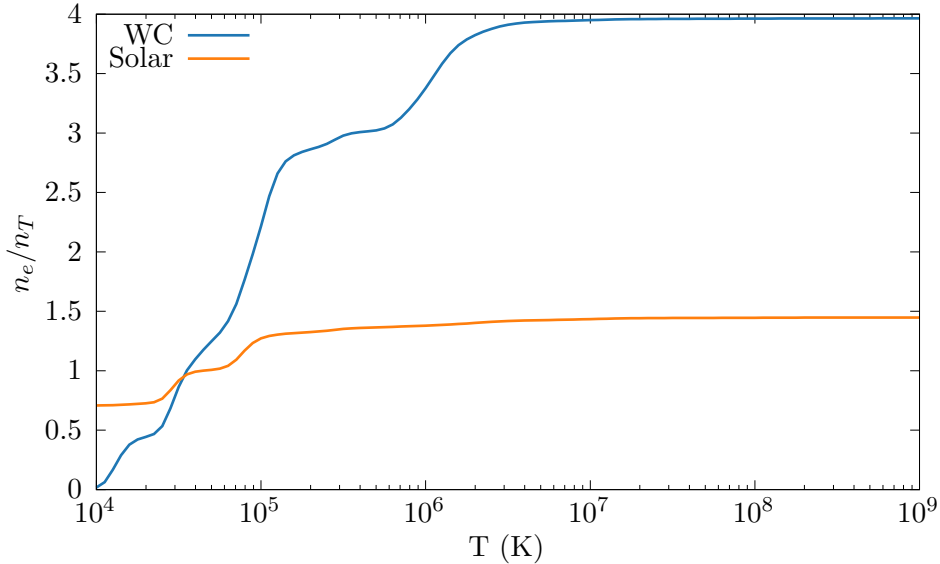


Figure 3.9: Ionisation fraction

heating, the approximation was chosen.

Further improvements were made to correctly determine the electron number, n_e , to calculate the cooling contribution for dust due to grain-electron collisions. the initial version of this code assumed that $n_e = 1.1n_p$, an estimate based on solar abundances, however the electron-to-ion ratio varies significantly with temperature in a WC wind, which is hydrogen depleted and as such can vary from 0 to ~ 4 between 10^4 and 5×10^6 K (figure 3.9). In order to solve this problem quickly for each timestep, a lookup table similar to the plasma cooling curves was used, containing the electron-ion ratio at temperatures between 10^4 and 10^8 K for each wind abundance.

3.7.4 Model implementation

In order to simulate energy loss due to radiation in **Athena++**, the conserved variable array is adjusted to remove energy from a specific cell, this is analogous to energy being removed from the system due to radiative processes. This process is assumed to be 100% efficient, re-adsorption and scattering is not simulated, as this would be very complex to simulate at every time step.

Radiative processes are part of a source function that is performed for every mesh block. The cooling routine within the source function iterates through all cells within the meshblock,

calculating radiative energy loss for each cell. Within the loop, the cell parameters are loaded from the conserved variables array, and additional gas and dust parameters are calculated from these conserved variables. in particular the mean molecular mass of a cell is calculated with the formulae:

$$\mu = C\mu_{WR} + (1 - C)\mu_{OB}, \quad (3.12)$$

where μ_{WR} and μ_{OB} are the mean molecular masses of the winds and C is the wind “colour” scalar, the contribution of each wind to the gas density of the cell. The temperature is subsequently calculated using the ideal gas law:

$$T = \frac{P\mu m_H}{\rho k_B}. \quad (3.13)$$

At the current temperature, the cooling parameter, $\Lambda(T)$ for each wind is found from the lookup tables, and weighted in a similar manner as equation 3.12. The energy loss due to dust grains is then calculated, with the total energy loss rate within the cell defined as:

$$\dot{E} = \dot{E}_G + \dot{E}_D = \left(\frac{\rho}{m_H} \right)^2 \Lambda_G(T) + n_D \dot{E}_{\text{grain}}, \quad (3.14)$$

this energy loss rate is then multiplied by the timestep, dt , and then subtracted from the total energy within the cell.

One of the main issues with estimating the cooling rate rather than performing an exact calculation of energy loss is that the cooling rate and current temperature are coupled, this can result in wildly inaccurate final temperatures at the end of the cooling step compared with an exact integration. This is especially a concern at the expected temperatures in the post-shock, radiatively cooled environment, as the $\Lambda(T)$ is maximised at approximately 10^5 K. If the timestep is too large this can result in over-estimation of the cooling. The simplest solution would be to make the time-step smaller, however this would reduce the performance of the code, as the cooling loop takes significantly less time to perform than the hydrodynamical loop. Instead, adaptive sub-stepping is used to iterate through the time-step, adjusting the maximum sub-step for an integration based on the current gas parameters, specifically the amount of energy remaining in the cell. Figure 3.10 shows the adaptive sub-stepping routine in operation, at the initial time, the cooling parameter Λ is maximised, as such the time-step is significantly

3. METHODOLOGY & NUMERICAL SIMULATION

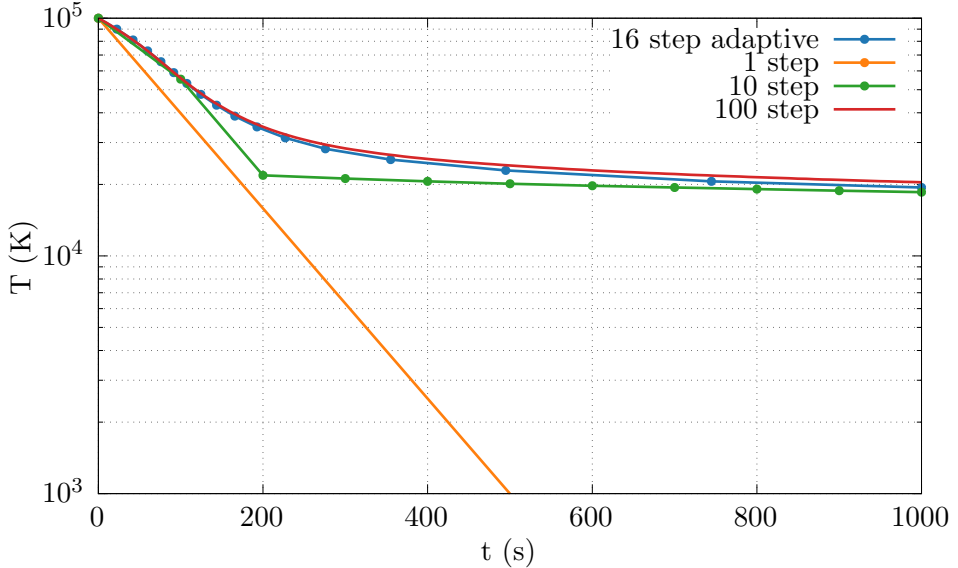


Figure 3.10: Comparison of the adaptive timestep method versus linearly spaced sub-steps for a solar abundance flow with a density of $10^{-16} \text{ g cm}^{-3}$ and an initial temperature of 10^5 K . Cooling was artificially limited to prevent negative temperatures, which would have occurred in the case of the 1 sub-step method.

lower than when the gas has cooled as is less radiative. This compares favourably to a single sub-step example, which would cause the simulation to crash due to negative temperatures, and with linearly spaced steps, which either required many more steps or were potentially unstable.

A suitably accurate maximum cooling time is calculated by first calculating the cooling time in the cell using the formulae:

$$\tau_{\text{cool}} = \frac{E_i}{\dot{E}_{\text{iter}}}, \quad (3.15)$$

where E_i is the cells internal energy and \dot{E}_{iter} is the total energy loss rate for the current iteration. A fraction of this value is used as the sub-timestep, which is used to calculate the energy loss in that iteration.

$$dt_{\text{step}} = \kappa \tau_{\text{cool}}, \quad (3.16)$$

Another iteration of the cooling calculation is then performed, with sub-step time re-calculated, until the elapsed time is equal to the hydrodynamical timestep, dt . Throughout the simulations in this project a value of $\kappa = 0.1$ was adopted.

3.7 Simulating CWB systems

In order to assess the performance and accuracy of this method, a test environment was produced to simulate the radiation of a region of gas in the post-shock environment. For this test, a gas density of $10^{-16} \text{ g cm}^{-3}$ and an integration timestep of 1,000 s were utilised. In order to demonstrate the flexibility of the adaptive method over the temperature ranges of a CWB simulation, initial temperatures of 10^5 , 10^6 and 10^7 K were used to demonstrate the models effectiveness in the cool, warm¹ and hot regimes of the WCR. This was compared with the exact integration method proposed in Townsend, 2009 as well as a modified version of the cooling code which uses evenly spaced sub-steps. To demonstrate the relative accuracy of the chosen cooling timescale fraction, lower values of κ were also used to demonstrate that lower values, while more accurate, were much more computationally complex.

The main limitation of a first-order Euler integration method such as this is that it converges on the correct answer slowly, and as such will be out by a few percent in the worst case so long as a sensible sub-step is used. Table 3.4 shows that while an iteration of the logarithmic index method used in this project is slightly more performant than the fast exact integration method proposed in Townsend, 2009, multiple sub-steps quickly render this performance benefit moot, in high-temperature cases with a lower gas density this method is much more accurate with fewer steps, however, as such this method was considered suitable for performing radiative cooling in the high-temperature immediate post-shock environment and lower density low-temperature WCR environment, where the bulk of this project focusses.

$\kappa = 0.1$			$\kappa = 0.01$			$\kappa = 0.001$		
T_i	Steps	Error	Steps	Error	Steps	Error		
10^5 K	16	6.025×10^{-2}	159	1.282×10^{-2}	1585	7.637×10^{-3}		
10^6 K	1	8.233×10^{-4}	6	1.012×10^{-4}	58	3.359×10^{-5}		
10^7 K	1	1.577×10^{-7}	1	1.577×10^{-7}	2	1.411×10^{-7}		

Table 3.3: Accuracy of the adpative sub-step Euler method compared with the Townsend, 2009 exact cooling method, with $\kappa = 0.1$ this method is out by 6% at worst in the low-temperature example, while very accurate at higher temperatures with only a single step needed.

Whilst this is a fairly simplistic method of performing adaptive sub-stepping, it is fast, effective, and not prone to failure. An adaptive RK method and implicit method were also considered, but not utilised in the final code, as this sub-stepping procedure was intended for speed and numerical safety over accuracy.

Care is made to correctly calculate energy loss around unresolved interfaces. *Finish this!*

¹See what I mean about the phrase “warm”?

3. METHODOLOGY & NUMERICAL SIMULATION

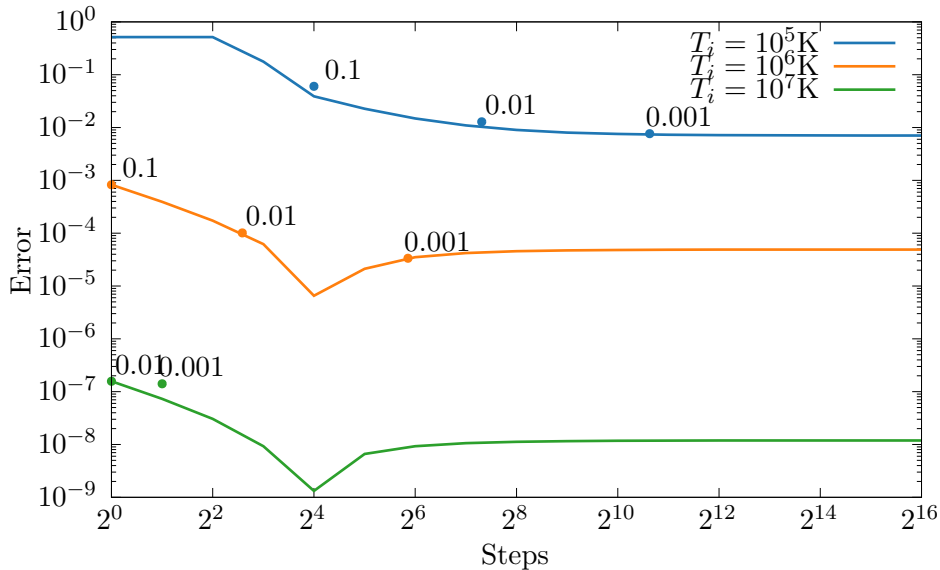


Figure 3.11: Comparison of estimated , points represent κ , in the low temperature case the answer is not particularly accurate, but with the adaptive method with $\kappa = 0.1$ the result is only out by a few percent for a small number of sub-steps.

	Search	Logarithmic	Townsend, 2009
τ (ns)	146	134	151
$\Delta\tau$ (ns)	8.0	1.5	0.9

Table 3.4: Comparison of performance between first order Euler integration methods and the exact integration method described by Townsend, 2009. Tests were conducted with a sample of 10^6 iterations on a 3.2 GHz M1 processor, while the code was compiled using clang 12.0.5 and the -O3 optimisation set.

3.8 The BODMAS Adverted Scalar Dust Model

Binary Orbit Dust Model with Accretion and Sputtering¹

The primary focus of this project was to implement a dust model within a numerical simulation, in order to determine the growth of dust grains within the

3.8.1 BODMAS features

3.8.2 Implementation

(Dwek et al., 1996)

The most processing efficient method of

The dust content of the system can be defined in the form of

a and z

This method does have its drawbacks, principally, the advected scalar method cannot simulate grain-grain or grain-gas interactions with high relative velocities, such as interactions within the wind collision region, where

Dust grains are assumed to be spherical, as atoms accrete or sputter from the surface of the grain, this corresponds to a change in grain radius, da/dt , this can be extrapolated to find the change in grain density with the formulae:

$$\frac{dV_{\text{gr}}}{dt} = 4\pi a^2 \frac{da}{dt}, \quad (3.17a)$$

$$\frac{dm_{\text{gr}}}{dt} = \rho_{\text{gr}} \frac{dV_{\text{gr}}}{dt}, \quad (3.17b)$$

$$\frac{d\rho_d}{dt} = n_d \frac{dm_{\text{gr}}}{dt}, \quad (3.17c)$$

where dV_{gr}/dt and dm_{gr}/dt are the change in grain volume

at the end of every time step,

Grain accretion in this model occurs at temperatures from 10^4 K to 1.4×10^4 K,

¹All good theses have a laboured acronym!

3. METHODOLOGY & NUMERICAL SIMULATION

da/dt and $d\rho_d/dt$ are then integrated across the simulation time-step using the Euler method, as the time-scale of dust accreting in significant quantities is much smaller than the time-scale of a single step.

The grain radius scalar is recalculated using following formula:

$$a_{\text{new}} = a_{\text{old}} + \Delta a_{\text{accretion}} - a_{\text{sputter}}, \quad (3.18)$$

where a_{old} is the pre-timestep grain radius,

The new gas density in the cell is then recalculated using the formulae:

$$\rho_{g,\text{new}} = \rho_{g,\text{old}} + \Delta \rho_{d,\text{sputter}} - \Delta \rho_{d,\text{accretion}}, \quad (3.19)$$

$\Delta \rho_{d,\text{sputter}}$ and $\Delta \rho_{d,\text{accretion}}$ are the changes in dust density due to sputtering and grain-gas accretion respectively. Finally, the scalars z is recalculated for the new dust and gas densities.

3.8.3 Contemporary dust Models

The Hendrix dust model

Perhaps the most similar contemporary dust model is the model described in Hendrix et al. (2016) - as this model is concerned with simulating the dynamics of dust within a CWB. This is not to say that these models are identical, of course, as the Hendrix model explores how dust spreads throughout the WCR of WR 98a, in order to compare with observational data using radiative transfer code.

The main differentiating factors between this model and our model are the driving mechanism and dust evolution. In the Hendrix model dust is modelled as a separate fluid, with an Epstein drag function between the wind and dust fluids; this method allows for dust kinematics that aren't implicitly co-moving. This is a more accurate method of modelling dust, however it requires significantly more processing time and is much more difficult to implement, requiring a numerical code that supports multiple fluids. At the start of this PhD this was considered but eventually rejected due to time constraints.

However, the Hendrix model has limitations that this model does not have, this is because the purpose of the Hendrix model is to analyse the distribution of dust within a CWB system,

3.8 The BODMAS Adverted Scalar Dust Model

rather than to model the evolution of the dust itself. To this end, the Hendrix model does not calculate dust growth or destruction, and only uses a single small grain size, with the dust-to-gas mass ratio calculated based on observations of the target system, WR98a.

3.8.4 Future dust models

Due to time constraints and limitations in the code in use, only a limited set of mechanisms for dust evolution were included in this projects simulations. While the BODMAS model represents an interesting start for the modelling of dust grains in colliding wind binaries, future models could implement more complex models which incorporate additional destruction and growth mechanisms as well as

A multi-scalar model could be used to more accurately measure the growth of dust grains, rather than a single average grain size and This would be more difficult to implement than a single model but would be able to simulate the growth of grains with a large number *Athena++* and MG both have issues with a large number of scalars, as such both numerical codes may require significant modification to cope with this. A multi-fluid model with dust being physically simulated rather than assumed to be perfectly co-moving would be an ideal next step. Multiple grain size distributions could also be modelled in a similar way to the proposed multi-scalar model, however the kinematics of the dust grains could also be simulated separately. The increased inertia of more massive dust grains could result in the kinematics of the dust flow diverging from the co-moving assumption. To that end, a successor dust model would adopt a multi-fluid and drag function method, which was considered but not included for the sake of time. This multi-fluid model would also allow for more physically accurate simulation of grain-gas and grain-grain interactions, as the collision velocities would be exactly calculated rather than estimated through bulk motion properties, high speed collision of gas on dust grains in the immediate post-shock environment could also shatter grains, though modelling this as well as spalling of particles in the wind through the dust grains would be complex to simulate.

Furthermore, additional mechanisms for dust destruction, such as through photodissociation and sublimation could also be implemented, the implementation of these could be used to determine the effectiveness of the WCR in protecting nascent, still forming dust grains.

The initial grain nucleation model could also be improved, injection of extremely small grains into the simulation through the stellar remap zones was chosen as the underlying chemical process for formulation of these dust grains is poorly understood at the time of writing. The

3. METHODOLOGY & NUMERICAL SIMULATION

small grain nucleation model was also found to be only dependent on the initial grain radius, a_i , whilst changing the amount of grain nuclei in the WR wind does not change the amount of dust produced. As such the simulations are currently bound by a single input parameter, which can be constrained based on what is currently understood about dust grain accretion. A more complex model may require additional parameters, and as such would be highly dependent on them.

Another avenue of future research would be performing a radiative transfer simulation upon a fully advected system, in order to compare with

This was initially considered at the start of the project, but was not performed due to the limited amount of time remaining at the end of the PhD.

This was performed by Hendrix et al. (2016), with the resultant images emulating the sensitivity and angular resolution characteristics of UKIRT, Keck and ALMA (figure 3.12).

Radiative transfer models would be used to

3.8 The BODMAS Advected Scalar Dust Model

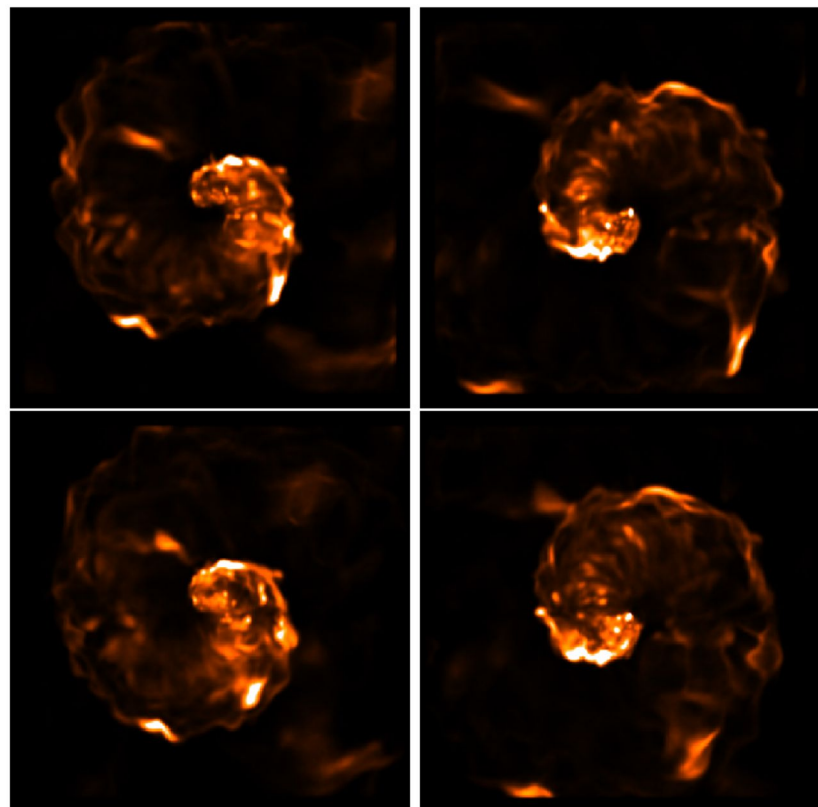


Figure 3.12: Synthetic images of WR 98a emulating the capabilities of ALMA using a radiative transfer model, reproduced from Hendrix et al. (2016).

3. METHODOLOGY & NUMERICAL SIMULATION

CHAPTER 4

An exploration of dust formation within WCd systems
using an advected scalar dust model

4. AN EXPLORATION OF DUST FORMATION WITHIN WCD SYSTEMS

Abstract

Dust production is one of the more curious phenomena observed in massive binary systems with interacting winds. The high wind temperatures, UV photon flux and violent shocks should destroy any dust grains that condense. However, in some extreme cases dust production yields of approximately 30% of the total mass of the stellar winds have been observed. In order to better understand this phenomenon a parameter space exploration was performed using a series of numerical models of dust producing carbon phase Wolf-Rayet (WCd) systems. These models incorporated a passive scalar dust model simulating dust growth, destruction and radiative cooling. We find that reasonable dust yields were produced by these simulations. Significant changes in the dust yield were caused by changing the mass loss rates of the stars, a greater mass loss rate contributing to increased dust yields. Similarly, a close orbit between the stars also resulted in higher dust yields. Finally, a high velocity wind shear, which induces Kelvin-Helmholtz (KH) instabilities and wind mixing drastically increases the dust yields.

4.1 Introduction

Binary systems with colliding stellar winds are a fascinating type of system, capable of producing a variety of peculiar phenomena. The shocks produced from this wind interaction creates some of the most luminous persistent stellar-mass x-ray sources in the night sky (Rosslowe & Crowther, 2015). Within the wind collision region the available mechanical energy can exceed $10^4 L_\odot$, producing shocks with temperatures up to 10^8 K.

In particularly energetic colliding wind binary (CWB) systems with a Wolf-Rayet (WR) star as the main producer of the stellar wind, dust in the form of amorphous carbon grains has been observed to form (Allen et al., 1972). This is particularly curious, as the high wind temperatures, strong shocks and UV luminosities of these systems would result in dust grains being rapidly destroyed through sublimation processes. These dust forming CWB systems have only been observed to occur if a carbon phase WR star (WC star) is partnered with either another WR star or an OB main sequence star (a WR+OB system). While the exact methods of dust formation and evolution in these systems are poorly understood, dust formation rates

4.1 Introduction

have been observed to be extremely high, up to $10^{-6} M_{\odot} \text{ yr}^{-1}$. This is approximately 36% of the total wind by mass in the case of WR104 (Lau et al., 2020).

Within different colliding wind binary systems, dust may form either continuously or periodically. The first such observed dust forming system was the episodic dust forming system WR140, first reported by P. M. Williams, van der Hucht, Pollock et al. (1990) who observed a significant and highly variable infrared excess, consistent with emission from dust grains. The dust production rate was later found to vary by a factor of 40 over the orbital period of 7.9 yr (Thomas et al., 2021; van der Hucht et al., 1999). Persistent dust forming systems were subsequently discovered, such as WR104 (Tuthill et al., 1999) and WR98a (Monnier et al., 1999). Whilst the exact mechanism for dust formation is not currently known, there is a strong correlation between periodicity and eccentricity, with less eccentric systems forming dust continuously, while highly eccentric systems exhibit episodic dust formation (Crowther, 2003). Due to this orbital dependency, it is likely that there is an optimal dust forming separation, where dust can form in large quantities. This could be due to factors such as strong post shock cooling, which is highly dependent on the wind speed and orbital separation. Additionally, dust may be protected from the bulk of the stellar radiation due to the extremely large degree of extinction that may occur in the dense post-shock environment of radiative shocks (Cherchneff, 2015).

Direct observation of dust forming CWBs and in particular the wind collision region (WCR) is exceptionally difficult for a number of reasons:

- WR+OB CWB systems are extremely rare. Of the 667 catalogued WR stars at the time of writing, 106 have been confirmed to be in a binary system (Rosslowe & Crowther, 2015; P. M. Williams, 2019).
- A WC star is required for dust formation. No nitrogen sub-type Wolf-Rayet (WN) have been observed to form dust.
- Not all WC+OB systems are dust producing, limiting the sample size further.
- 56 dust forming systems with a known spectral type have been observed overall. Despite producing an extremely large quantity of dust in their local region, they are outnumbered by AGB stars by ~ 3 orders of magnitude (Ishihara et al., 2011).
- Galactic CWB systems are comparatively distant from earth. For instance, WR 104, a well-studied system, is ~ 2.5 kpc distant (Soulain et al., 2018) and no WCd systems

4. AN EXPLORATION OF DUST FORMATION WITHIN WCD SYSTEMS

have been detected at a distance of $< 1 \text{ kpc}$ (Rosslowe & Crowther, 2015). This prevents observations of these systems at a high angular resolution.

- Grain growth from small nucleation grains is predicted to be very rapid in CWB systems (Zubko, 1998). Therefore studying the initial grain evolution would require observations of extremely high angular resolution.

For these reasons, numerical simulations are useful for modelling the growth of dust grains within this unresolved region. In order to better understand what influences dust production in a CWB system, a parameter space exploration of the wind and orbital parameters was performed. In particular the orbital separation, mass-loss rate and wind velocity were modified for both stars in order to influence the wind momentum ratio, η , and the cooling parameter, χ . The wind momentum ratio is defined as:

$$\eta = \frac{\dot{M}_{\text{OB}} v_{\text{OB}}^{\infty}}{\dot{M}_{\text{WR}} v_{\text{WR}}^{\infty}}, \quad (4.1)$$

where \dot{M} is the mass loss rate of a star and v^{∞} is the terminal velocity of a star's outflow. A low value for η indicates that the winds are extremely imbalanced, with the WR typically dominating the wind dynamics of the system. The wind momentum ratio determines for a given orbital separation, d_{sep} , the distance from each star to the apex of the wind collision. We define the terms r_{WR} and r_{OB} , representing the distance from the WR and OB stars to the stagnation point of the WCR:

$$r_{\text{WR}} = \frac{1}{1 + \eta^{1/2}} d_{\text{sep}}, \quad (4.2a)$$

$$r_{\text{OB}} = \frac{\eta^{1/2}}{1 + \eta^{1/2}} d_{\text{sep}}. \quad (4.2b)$$

This assumes the winds both accelerate to terminal speed and that there is no radiative inhibition (Stevens & Pollock, 1994) or braking (Gayley et al., 1997). In some systems the winds may be so imbalanced that the stronger wind collides directly with the companion star. The half-opening angle of the WCR can be estimated by the formulae:

$$\theta_c \simeq 2.1 \left(1 - \frac{\eta^{2/5}}{4}\right) \eta^{-1/3} \quad \text{for } 10^{-4} \leq \eta \leq 1, \quad (4.3)$$

to a relatively high degree of accuracy (Eichler & Usov, 1993; Pittard & Dawson, 2018).

The cooling parameter, χ , compares the cooling time to the escape time from the shocked region for a parcel of gas in the immediate post-shock environment. An approximation can be made using the known parameters of a system using the equation:

$$\chi = \frac{t_{\text{cool}}}{t_{\text{esc}}} \approx \frac{v_8^4 d_{12}}{\dot{M}_{-7}}, \quad (4.4)$$

where v_8 is the wind terminal velocity in units of 10^8 cm s^{-1} , d_{12} is the distance to the WCR apex in units of 10^{12} cm , and \dot{M}_{-7} is the mass loss rate in units of $10^{-7} M_{\odot} \text{ yr}^{-1}$ (Stevens et al., 1992). $\chi \leq 1$ indicates that radiative cooling is very important, while $\chi \gg 1$ indicates that the system is adiabatic. Strong cooling is aided with slow, dense winds and a high metallicity. As such in many systems the post-shock WR flow will rapidly cool from the immediate post-shock temperature of $\sim 10^{7-8} \text{ K}$ to temperatures in the dust formation range, $T \lesssim 10^4 \text{ K}$. A strongly radiating WCR can also be significantly compressed far more as it loses energy. In comparison, an adiabatic WCR is limited to a maximum density increase of a factor of 4 above the pre-shock wind density for a ratio of specific heats, $\gamma = 5/3$. The density increase and cool temperatures result in rapid dust growth and protection from the stellar UV radiation in some systems. Note also that Eq. 4.4 takes account of gas and plasma cooling only, but other cooling, such as dust cooling, may also be important.

In this paper, we aim to explore how dust formation is affected by the orbital and wind parameters of persistent dust forming WR+OB systems. This is performed by running a series of hydrodynamical simulations with an advected scalar dust model. In Section 4.2 we outline the methodology of our simulations, and how our dust model is implemented. We discuss our model series parameters, and why these parameters were chosen in Section 4.3. Finally we discuss our results and conclude in Sections 4.4 and 4.5.

4.2 Methodology

Numerical simulations within this paper utilise the Athena++ hydrodynamical code, a highly modular modern fluid dynamics code (Stone et al., 2020). Simulations are generated in 3D and the Euler hydrodynamical equations are solved in the form:

4. AN EXPLORATION OF DUST FORMATION WITHIN WCD SYSTEMS

$$\frac{\partial \rho}{\partial t} + \nabla \cdot (\rho \mathbf{u}) = 0, \quad (4.5a)$$

$$\frac{\partial \rho \mathbf{u}}{\partial t} + \nabla \cdot (\rho \mathbf{u} \mathbf{u} + P) = 0, \quad (4.5b)$$

$$\frac{\partial \rho \varepsilon}{\partial t} + \nabla \cdot [\mathbf{u} (\rho \varepsilon + P)] = \dot{E}_{\text{cool}}, \quad (4.5c)$$

where ε is the total specific energy ($\varepsilon = \mathbf{u}^2/2 + e/\rho$), ρ is the gas density, e is the internal energy density, P is the gas pressure, \mathbf{u} is the gas velocity and \dot{E}_{cool} is the energy loss rate per unit volume from the fluid due to gas and dust cooling.

Athena++ has been configured to run using a piecewise linear reconstruction method with a 4th order Strong Stability Preserving Runge-Kutta time-integration method (Spiteri & Ruuth, 2002). Athena++ was forked from the original repository and additional routines were written for a colliding wind binary scenario. Routines were created to produce a steady outflow from a small spherical region around a set of cartesian co-ordinates as well as a function to move these co-ordinates with each time-step; these were used to simulate stellar wind outflow and orbital motion, respectively. Additionally, Athena++ was further modified to include an advected scalar dust model for simulating dust growth and destruction as well as a photon emission cooling model to approximate cooling for gas and dust particles within the fluid.

Athena++ utilises OpenMPI for parallelism, breaking the simulation into blocks, which are distributed between processors. The block size is variable, but for these simulations a block size of $32 \times 32 \times 8$ was found to be optimal. This meshblock system is also utilised in mesh refinement for increasing the effective resolution. As the CWB systems are being simulated in their entirety, a very large volume needs to be simulated, while at the same time the region between the stars must be resolved with a resolution of at least 100 cells in order to adequately resolve the WCR. This difference in length scales necessitates the use of static mesh refinement (SMR) to improve the effective resolution of the simulation. A base coarse resolution of $320 \times 320 \times 40$ cells in XYZ is defined for the simulations, while a region close to the stars operates at a higher refinement level. This results in a resolution increase of a factor of 2^{n-1} greater than the coarse resolution, where n is the refinement level (see Fig. 4.1). In the case of 7 levels (inclusive of the base, “coarsest” level) as used in most of the simulations in this paper, this results in an effective resolution of $20480 \times 20480 \times 2560$ cells. SMR is utilised instead of Adaptive Mesh Refinement, a more flexible conditional method, as it has proven to be more reliable for our simulations. As much of the grain evolution occurs a small distance from the WCR stagnation point, much of

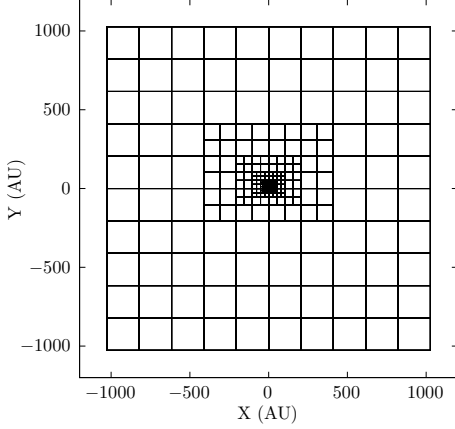


Figure 4.1: A plot of the blocks used in a 7 level simulation with a block size of $32 \times 32 \times 8$ cells. The block density increases dramatically closer to the barycentre. The coarse simulation resolution is $(320 \times 320 \times 40)$ cells with a block size of $(32 \times 32 \times 8)$ cells. The diagram is sliced about the z axis at $z = 0$.

the simulation volume can be run at a lower resolution without affecting the simulation results.

The wind outflow from each star is simulated by replacing the conserved variables (density, momentum and energy) within a small region around the expected position of the stars; this region is typically on the order of 6 maximally refined cells in radius. This rewrite corresponds to a change in density, ρ_R , pressure, P_R , and mechanical energy, E_R , imparted by an outflowing wind, such that

$$\rho_R = \frac{\dot{M}}{(4\pi r^2 v_\infty)}, \quad (4.6a)$$

$$P_R = \rho_R k_B T_w / \mu m_H, \quad (4.6b)$$

$$E_R = \frac{P_R}{\gamma - 1} + \frac{1}{2} \rho_R v_\infty^2, \quad (4.6c)$$

where v_∞ is the wind velocity as it flows radially from the center of the “remap zone”, T_w is the wind temperature and r is the radial distance from the current cell to the centre of the remap zone. Orbits are calculated by moving the remap zones in a manner consistent with Keplerian dynamics, which are repositioned at the start of every timestep. This orbital speed is also added to the remap wind speed.

4. AN EXPLORATION OF DUST FORMATION WITHIN WCD SYSTEMS

	X(E)	
	Solar	WC9
H	0.705	0.0
He	0.275	0.546
C	3.07×10^{-3}	0.4
N	1.11×10^{-3}	0.0
O	9.60×10^{-3}	0.05

Table 4.1: Abundances by mass used for the OB and WR stars being simulated. Other elements are assumed trace when calculating dust emission (P. M. Williams et al., 2015).

4.2.1 Gas and dust cooling

Cooling due to photon emission from atoms, ions and free electrons, as well as dust particles, is simulated by removing energy from a cell at each timestep. The total energy loss is calculated by integrating the energy loss rates due to gas, plasma and dust cooling using the Euler method; in regions with very rapid cooling sub-stepping is used to improve accuracy, with the number of sub-steps being determined by comparing the timestep to the cooling timescale of the cell. Gas cooling is simulated using a lookup table method. A data file containing the gas temperature and associated normalised emissivity, $\Lambda_w(T)$, of the wind at that temperature is read into the simulation. In a typical cooling step, the temperature is calculated and compared with the lookup table to find the closest temperature bins that are lower and higher than the cell temperature. A linear interpolation is then performed to find an appropriate value for $\Lambda_w(T)$. The energy loss in the stellar wind can then be calculated with the formulae:

$$\frac{dE}{dt} = \left(\frac{\rho}{m_H} \right)^2 \Lambda_w(T), \quad (4.7)$$

where ρ is the gas density and m_H is the mass of a hydrogen atom. The lookup table was generated by mixing a series of cooling curves generated by MEKAL simulations of elemental gasses. These simulations were combined based on the elemental abundances of each wind, with the WC star having typical WC9 abundances and the OB star having a solar abundance (see Table 4.1). Figure 4.2 shows the resulting cooling curves used for each star. The most significant abundances used are noted in Table 4.1. The cooling regime of the simulations ranges between temperatures of 10^4 to 10^9 K. A floor temperature of 10^4 K is implemented. Temperatures between $10^4 \text{ K} < T \leq 1.1 \times 10^4 \text{ K}$ are set to 10^4 K as they are assumed to be either rapidly cooling or a part of the stellar wind.

4.2 Methodology

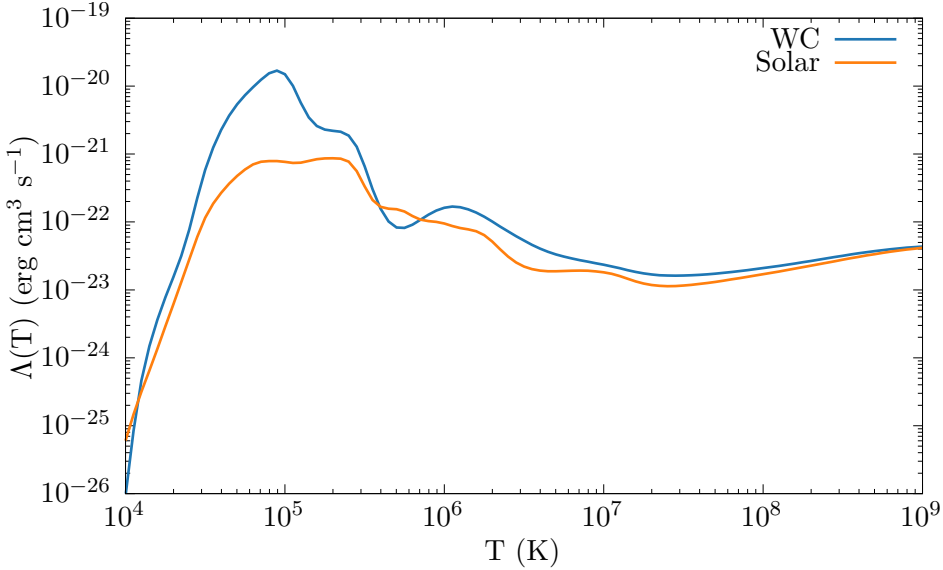


Figure 4.2: Comparison of WC and solar cooling curves for calculating the energy loss due to gas cooling.

A model for cooling due to emission from dust grains is also included as dust cooling is expected to play a significant role in each system. The rate of cooling is calculated using the uncharged grain case of the Dwek and Werner (1981) prescription. Grains are heated due to collisions with ions and electrons, causing them to radiate, with energy being removed from the simulation. This assumes that the region being simulated is optically thin to far infrared photons. The grain heating rate (in erg s^{-1}) is calculated with the following formulae:

$$H = 1.26 \times 10^{-19} \frac{n}{A^{1/2}} a^2 (\mu\text{m}) T^{3/2} h(a, T), \quad (4.8)$$

where H is the heating rate due to atom and ion collisions, n is the particle number density, A is the mass of the incident particle in AMU, $a(\mu\text{m})$ is the grain radius in microns, T is the temperature of the ambient gas, and $h(a, T)$ is the effective grain “heating factor”, also referred to as the grain transparency.

To obtain the collisional heating due to incident atoms, H_{coll} , the heating rates are summed for hydrogen, helium, carbon, nitrogen and oxygen atom collisions:

$$H_{\text{coll}} = H_{\text{H}} + H_{\text{He}} + H_{\text{C}} + H_{\text{N}} + H_{\text{O}}. \quad (4.9)$$

Other elements are not considered as they are present in trivial proportions in both winds. As

4. AN EXPLORATION OF DUST FORMATION WITHIN WCD SYSTEMS

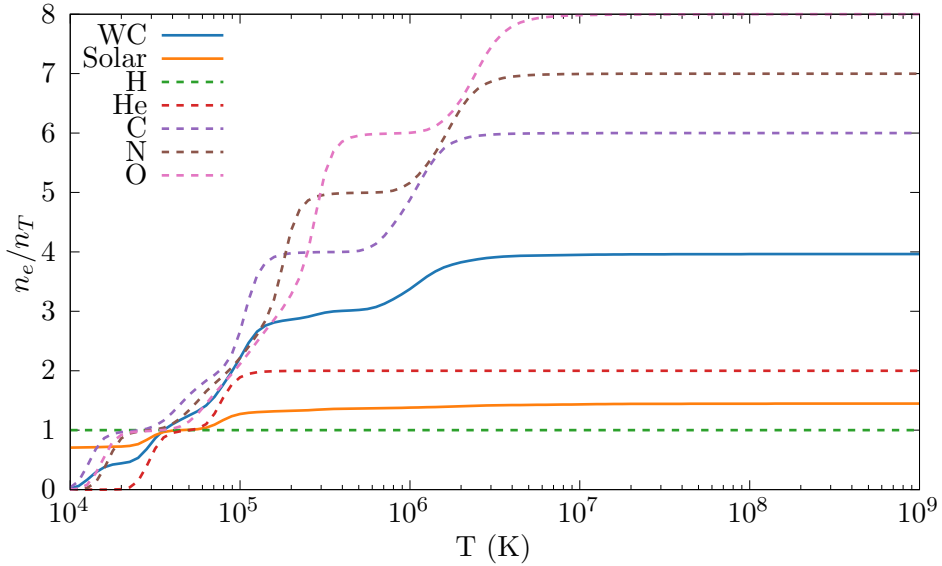


Figure 4.3: A comparison of the electron-ion ratio in both winds as a function of temperature. Also shown are the electron-to-ion ratios for the individual elements.

dust grains are assumed to be uncharged, the grain transparency for each species is calculated with the formulae:

$$h(a, T) = 1 - \left(1 + \frac{E_0}{2k_B T}\right) e^{-E_0/k_B T}, \quad (4.10)$$

where E_0 is the initial energy required to overcome the grain's potential and k_B is the Boltzmann constant.

Electron-grain collisional heating, H_{el} , is modelled using the same calculation for H_{coll} , albeit with some differences. One major factor for accurately calculating the energy loss due to electron collisions is that the electron number density, n_e , needs to be correct. This is achieved with a second series of lookup tables that contain the electron-to-ion ratio of each wind across a temperature range of 10^4 to 10^9 K (Fig. 4.3). The electron number density is $n_e = \beta n_i$, where β is the electron-to-ion ratio and n_i is the ion number density. Another difference between calculating electron-grain and gas-grain cooling is calculating electron-grain transparency, which is a significantly more complex problem than calculating ion-grain transparency. An assumed full opacity proves to be extremely inaccurate at temperatures $> 10^6$ K. Electron-grain transparency is therefore calculated via an approximation described in Dwek and Werner (1981):

$$\begin{aligned}
h(x^*) &= 1, & x^* > 4.5, \\
&= 0.37x^{*0.62}, & x^* > 1.5, \\
&= 0.27x^{*1.50}, & \text{otherwise,}
\end{aligned} \tag{4.11}$$

where $x^* = 2.71 \times 10^8 a^{2/3} (\mu\text{m})/T$. This approximation is approximately 4 orders of magnitude faster than using an integration method, while differing by less than 8% (Fig. 4.4). Grain-grain collisions are not modelled, as this would be difficult to calculate due to the single-fluid model in use. Further simulations utilising a multi-fluid model could allow for this to be simulated. Finally, in order to calculate the change in energy due to dust cooling, the rate of energy change, dE/dt , is calculated using the formulae:

$$\Lambda_d(T, a) = \frac{H_{\text{coll}} + H_{\text{el}}}{n_H}, \tag{4.12a}$$

$$\frac{dE}{dt} = n_T n_d \Lambda_d(T, a), \tag{4.12b}$$

where Λ_d is the normalised dust emissivity, n_H is the hydrogen number density, n_T is the total number density and n_d is the dust number density. The total energy loss rate per unit volume due to gas and dust cooling is given by:

$$\frac{dE}{dt} = \left(\frac{\rho}{m_H} \right)^2 \Lambda_w(T) + n_T n_d \Lambda_d(T, a). \tag{4.13}$$

4.2.2 Numerical modelling of dust through advected scalars

The most important modification to Athena++ was the addition of a dust growth and destruction model to simulate the production of dust within the WCR. A series of passive scalars were used where the dust parameters described by the scalars can evolve and advect through the simulation, analogous to a co-moving fluid, which previous papers have noted is an accurate dynamical model for dust within the WCR (Hendrix et al., 2016). In these simulations, information about the dust is stored in the form of two variables, the average grain radius, a , and the dust-to-gas mass ratio, z . From these constants the dust production rate, number density, and total dust mass can be derived. A co-moving model allows for a simplified model of dust formation. In such a model, the mean particle velocity between two particles of different size is:

4. AN EXPLORATION OF DUST FORMATION WITHIN WCD SYSTEMS

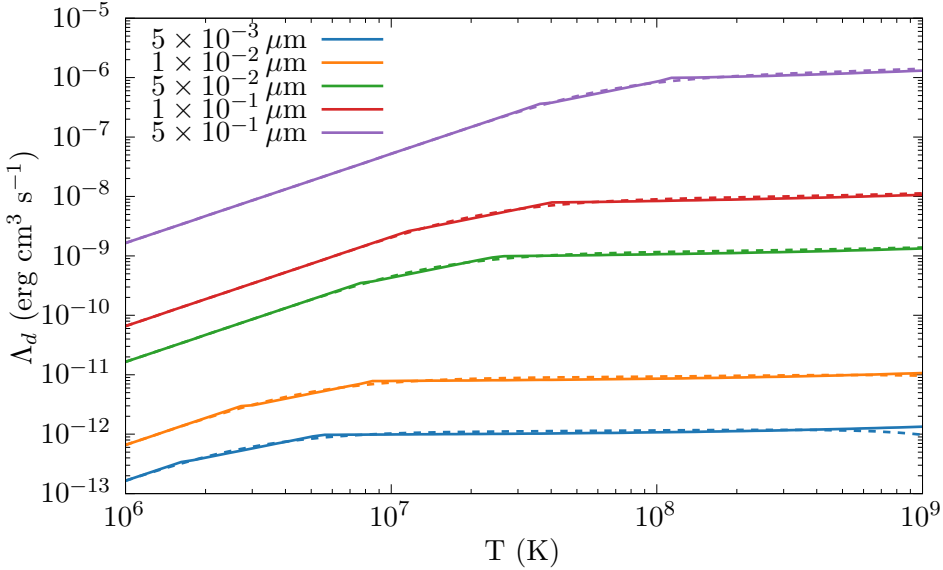


Figure 4.4: Dust grain cooling curves, $\Lambda_d(T, a)$, as a function of temperature for various grain sizes. The estimate method (Eq. 4.12, dashed line) is extremely close to the integral value (solid line) aside from at the highest temperatures.

$$\langle u \rangle = \sqrt{\frac{8kT}{\pi m_r}}, \quad (4.14)$$

where m_r is the familiar reduced mass between a test particle of mass m_t and a field particle of mass m_f , such that $m_r = m_f m_t / (m_f + m_t)$.

As the dust grain is significantly more massive, the reduced mass is approximately equal to the grain mass, simplifying the dynamics of the simulation in a co-moving case.

Dust growth is modelled through approximating growth due to grain-gas accretion where grains co-moving with a gas perform relatively low-velocity collisions with the surrounding gas, causing it to accrete onto the surface of the dust grain (Spitzer, 2008). Assuming a single average grain size the rate of change in the average grain radius is given by:

$$\frac{da}{dt} = \frac{\xi \rho_C w_C}{4 \rho_{gr}}, \quad (4.15)$$

where w_C is the Maxwell-Boltzmann distribution RMS velocity for carbon ($w_C = \sqrt{3k_B T / 12m_H}$), ξ is the grain sticking efficiency, ρ_C is the carbon density in the gas and ρ_{gr} is the grain bulk density. The associated rate of dust density change, $d\rho_d/dt$ is calculated with the formulae:

4.2 Methodology

$$\frac{dm_{\text{gr}}}{dt} = 4\pi\rho_{\text{gr}} \frac{da}{dt} a^2 = \pi\xi\rho_C w_C a^2, \quad (4.16a)$$

$$\frac{d\rho_{\text{d}}}{dt} = \frac{dm_{\text{gr}}}{dt} n_{\text{d}}, \quad (4.16b)$$

where n_{d} is the grain number density and dm_{gr}/dt is the rate of change of the grain mass. In this paper we take $\xi = 0.1$ as a conservative value, though this value can rise to as high as 1 in the case of highly charged grains. A bulk density analogous to amorphous carbon grains ($\rho_{\text{gr}} = 3.0 \text{ g cm}^{-3}$) is used.

Dust destruction gas-grain sputtering is calculated using the Draine and Salpeter (1979b) prescription. A dust grain has a lifetime which is dependent on the number density of the gas the grain is moving through, n_g . In the case of amorphous carbon grains, the dust lifetime is:

$$\tau_{\text{d}} = \frac{a}{\dot{a}} \approx 3 \times 10^6 \frac{a}{n_g} \text{ yr}, \quad (4.17)$$

where a is in microns. This value is based on an average lifetime of carbon grains in interstellar shocks at shock temperatures between 10^6 and $3 \times 10^8 \text{ K}$ (Dwek et al., 1996; Tielens et al., 1994). The rate of change in grain mass can then be calculated with the formulae:

$$\frac{dm_{\text{gr}}}{dt} = -4\pi\tau_{\text{d}}\rho_{\text{gr}}n_g a^2, \quad (4.18a)$$

$$\frac{d\rho_{\text{d}}}{dt} = \frac{dm_{\text{gr}}}{dt} n_{\text{d}}. \quad (4.18b)$$

Application of the dust growth and destruction routines in the code is determined by the gas temperature of a cell. Dust growth occurs when $T \leq 1.4 \times 10^4 \text{ K}$ whilst dust destruction occurs at temperatures of $T \geq 10^6 \text{ K}$.

In order to propagate dust through each simulation, a small initial value for the advected scalars is set in each cell in the remap zones. An initial grain radius of $a_i = 50 \text{ \AA}$ and initial dust-to-gas mass ratio of $z_i = 10^{-6}$ is imposed. Changing z_i does not significantly impact the final dust-to-gas mass ratio of the system as z rapidly increases within the WCR and dust growth in the WCR dominates the total production. Dust also grows to some extent in the unshocked winds but at a much lower rate than within the WCR. A small initial grain radius is sensible,

4. AN EXPLORATION OF DUST FORMATION WITHIN WCD SYSTEMS

as small dust grains are believed to rapidly nucleate from impinging carbon ions (Harries et al., 2004b; Zubko, 1998).

In order to determine if our dust model is producing reasonable dust yields, we calculate the maximum expected dust production rate in each system, $\dot{M}_{d,\max}$ (Pittard & Dawson, 2018). This rate would occur if 100% of the carbon in the WR wind being shocked by the WCR was converted into dust. The fraction of the WR wind that passes through the WCR is given by

$$f_{\text{WR}} = \frac{1 - \cos(\theta_{\text{WR}})}{2}, \quad (4.19)$$

where θ_{WR} is the opening angle of the WR shock front, approximated as $\theta_{\text{WR}} \approx 2 \tan^{-1}(\eta^{1/3}) + \pi/9$. The theoretical maximum dust production rate is then

$$\dot{M}_{d,\max} = \dot{M}_{\text{WR}} X_{\text{C,WR}} f_{\text{WR}}, \quad (4.20)$$

where X_{C} is the carbon mass fraction in the WR star.

4.3 Model Parameters

In this paper we do not attempt to model particular systems. Rather we aim to gain a deeper understanding of the primary influences of dust formation in a CWB system. A series of simulations were therefore run in order to determine how dust formation varies due to changes in orbital separation and wind momentum ratio. A baseline simulation with properties similar to WR98a with a circular orbit and identical stellar masses was created. This baseline simulation has a momentum ratio of 0.02. Other simulations were then run with different orbital separations and/or wind momentum ratios. Another set of simulations were run where the cooling mechanisms were selectively disabled, in order to understand how radiative cooling affects the dust production rate. Tables 4.2 and 4.3 detail the wind and orbital parameters of the baseline simulation. The orbital separation is modified by changing the orbital period of the simulation, while the wind momentum ratio is modified by adjusting the mass loss rate and wind terminal velocity for each star. Two simulation sub-sets for this were performed: simulations where the wind terminal velocities were adjusted for each star and simulations where the mass loss rates for each star were adjusted.

4.3 Model Parameters

Parameter	WR	OB
\dot{M}	$5.0 \times 10^{-6} M_{\odot} \text{ yr}^{-1}$	$5.0 \times 10^{-8} M_{\odot} \text{ yr}^{-1}$
v_{∞}	$1.0 \times 10^8 \text{ cm s}^{-1}$	$2.0 \times 10^8 \text{ cm s}^{-1}$
T_w	$1.0 \times 10^4 \text{ K}$	$1.0 \times 10^4 \text{ K}$

Table 4.2: Wind properties of the baseline system.

Parameter	Value
$M_{\text{WR/OB}}$	$10.0 M_{\odot}$
d_{sep}	4.0 AU
P	1.80 yr

Table 4.3: Baseline system orbital properties.

4.3.1 Cooling mechanisms

For this set of simulations, the influence of cooling was changed by varying which cooling routines are operating. All simulations in this set keep the same orbital and wind parameters, which are that of the baseline system described in Tables 4.2 & 4.3. One simulation has both plasma and dust cooling in operation (the `fullcool` simulation), while the other two simulations have plasma cooling only and no cooling, respectively (`plasmacool` and `nocool`, Table 4.4). The final, no radiative cooling simulation instead relies on adiabatic expansion for temperature change in the WCR; as such, this simulation behaves as if it has a χ value for both winds that is arbitrarily high. The post-shock flow in the `nocool` model will also be unable to compress as much due to the lack of energy loss via radiative cooling. The role of these simulations is to discern whether cooling alone, or other system parameters can affect dust production.

4.3.2 Wind momentum ratio

Another set of simulations was devised in order to assess the influence of the wind parameters on the formation of dust within a CWB. As the wind momentum ratio is dependent on both the mass loss rate and wind velocity of each star, each of these properties is modified over a set

Name	Plasma cooling?	Dust cooling?
<code>fullcool</code>	Yes	Yes
<code>plasmacool</code>	Yes	No
<code>nocool</code>	No	No

Table 4.4: Cooling series simulation parameters.

4. AN EXPLORATION OF DUST FORMATION WITHIN WCD SYSTEMS

Name	\dot{M}_{WR}	\dot{M}_{OB}	v_{WR}^{∞}	v_{OB}^{∞}	η	χ_{WR}	χ_{OB}
<code>baseline</code>	$5.0 \times 10^{-6} M_{\odot} \text{ yr}^{-1}$	$5.0 \times 10^{-8} M_{\odot} \text{ yr}^{-1}$	10^8 cm s^{-1}	$2 \times 10^8 \text{ cm s}^{-1}$	0.02	1.20	1915
<code>mdot-1</code>	$1.0 \times 10^{-5} M_{\odot} \text{ yr}^{-1}$	$5.0 \times 10^{-8} M_{\odot} \text{ yr}^{-1}$	10^8 cm s^{-1}	$2 \times 10^8 \text{ cm s}^{-1}$	0.01	0.60	1915
<code>mdot-2</code>	$2.5 \times 10^{-6} M_{\odot} \text{ yr}^{-1}$	$5.0 \times 10^{-8} M_{\odot} \text{ yr}^{-1}$	10^8 cm s^{-1}	$2 \times 10^8 \text{ cm s}^{-1}$	0.04	2.39	1915
<code>mdot-3</code>	$5.0 \times 10^{-6} M_{\odot} \text{ yr}^{-1}$	$1.0 \times 10^{-7} M_{\odot} \text{ yr}^{-1}$	10^8 cm s^{-1}	$2 \times 10^8 \text{ cm s}^{-1}$	0.04	1.20	957
<code>mdot-4</code>	$5.0 \times 10^{-6} M_{\odot} \text{ yr}^{-1}$	$2.5 \times 10^{-8} M_{\odot} \text{ yr}^{-1}$	10^8 cm s^{-1}	$2 \times 10^8 \text{ cm s}^{-1}$	0.01	1.20	3830
<code>vinf-1</code>	$5.0 \times 10^{-6} M_{\odot} \text{ yr}^{-1}$	$5.0 \times 10^{-8} M_{\odot} \text{ yr}^{-1}$	$2 \times 10^8 \text{ cm s}^{-1}$	$2 \times 10^8 \text{ cm s}^{-1}$	0.01	19.1	1915
<code>vinf-2</code>	$5.0 \times 10^{-6} M_{\odot} \text{ yr}^{-1}$	$5.0 \times 10^{-8} M_{\odot} \text{ yr}^{-1}$	$5 \times 10^7 \text{ cm s}^{-1}$	$2 \times 10^8 \text{ cm s}^{-1}$	0.04	0.07	1915
<code>vinf-3</code>	$5.0 \times 10^{-6} M_{\odot} \text{ yr}^{-1}$	$5.0 \times 10^{-8} M_{\odot} \text{ yr}^{-1}$	10^8 cm s^{-1}	$4 \times 10^8 \text{ cm s}^{-1}$	0.04	1.20	30638
<code>vinf-4</code>	$5.0 \times 10^{-6} M_{\odot} \text{ yr}^{-1}$	$5.0 \times 10^{-8} M_{\odot} \text{ yr}^{-1}$	10^8 cm s^{-1}	10^8 cm s^{-1}	0.01	1.20	120

Table 4.5: Wind parameters for simulations varying the wind mass loss rate, \dot{M} , and terminal velocity, v^{∞} . η is the wind momentum ratio (Eq. 4.1), χ is the cooling parameter (Eq. 4.4). Note that the value of χ does not take into account cooling due to dust.

of different simulations. η is varied from 0.01 to 0.04 by adjusting the wind parameters for each star. This is further subdivided by which property is modified, either the mass loss rate or wind terminal velocity (Table 4.5). As the cooling parameter, χ , has a much stronger dependency on v^{∞} than \dot{M} , the modification of either parameter while maintaining a similar value for η allows us to determine whether χ is the primary parameter determining the formation of dust within WCd systems. This can be seen when comparing simulations `mdot-1` and `vinf-1`, which have similar wind momentum ratios but the cooling parameters for the WC star differ by a factor of 32. These simulations are compared to the baseline simulation, which has a radiative post-shock WCR. All simulations were run for a minimum of 1 orbit. As these orbits are circular, there should be no major variance of the winds after the start-up transients are fully advected, save for some fluctuations.

4.3.3 Separation distance

A final series of simulations was performed with the wind parameters equivalent to the baseline model, but with differing orbital separations. The separation was altered by modifying the orbital period. The separation distance was varied from the baseline model of 4 AU up to 64 AU (Table 4.6), which has the effect of modifying the cooling parameter, χ , of each simulation without changing the wind momentum ratio; allowing us to further discern which is the dominant parameter influencing dust formation. For instance, simulation `dsep-64AU` has a cooling parameter value approaching the fast WR wind model `vinf-1`, despite having a wind momentum ratio of 0.02.

4.3 Model Parameters

Name	P	d_{sep}	χ_{WR}	χ_{OB}	Levels	Effective Resolution
<code>dsep-4AU</code>	1.80 yr	4 AU	1.20	1915	7	(20480 \times 20480 \times 2560) cells
<code>dsep-8AU</code>	5.06 yr	8 AU	2.39	3830	6	(10240 \times 10240 \times 1280) cells
<code>dsep-16AU</code>	14.3 yr	16 AU	4.79	7659	5	(5120 \times 5120 \times 640) cells
<code>dsep-32AU</code>	40.5 yr	32 AU	9.57	15319	4	(2560 \times 2560 \times 320) cells
<code>dsep-64AU</code>	115 yr	64 AU	19.1	30638	3	(1280 \times 1280 \times 160) cells

Table 4.6: Parameters of simulations varying the separation distance, d_{sep} , between the stars.

Each simulation has a coarse resolution of $320 \times 320 \times 40$ cells, with a varying number of levels. As the separation distance is doubled, the static mesh refinement box around the stars is doubled in size and the number of levels is decremented. This manipulation of levels ensures that the number of cells between the stars is kept consistent and reduces memory usage. The extent for all simulations in this series were doubled over the other series in this paper to approximately $2000 \times 2000 \times 250$ AU. Similarly to the previous set of simulations, a minimum of 1 orbit was needed for each simulation, however, as the orbital period of each simulation varies, certain simulations were able to run for a significantly longer length of time, with data for multiple orbits being obtained.

4.3.4 Data collection

HDF5 files were generated at regular time intervals - 3D HDF5 meshes were generated every $1/100^{\text{th}}$ of an orbit, while 2D slices were produced every $1/1000^{\text{th}}$ of an orbit. These HDF5 files contain the primitive variables of the simulation: gas density, ρ , gas pressure, P , and wind velocity components, v_x , v_y and v_z . These variables were then used to derive other variables such as temperature and energy. The scalars governing the dust properties were also stored for each cell: the dust-to-gas mass ratio, z , and the dust grain radius, a . The wind “colour”, the proportion of gas from each star, was also tracked. A value of 1.0 indicates a pure WR wind while 0.0 indicates a pure OB wind.

The volume-weighted totals of all parameters of interest were also collected, such as the total gas and dust mass of the system and average grain radius. Average values, such as \bar{z} and \bar{a} , are mass-weighted. To calculate dust formation within the WCR, a method of determining if a cell was part of the wind collision region was devised - the cell density would be compared to the predicted density of a single smooth wind with the wind parameters of the WC star in the system:

4. AN EXPLORATION OF DUST FORMATION WITHIN WCD SYSTEMS

$$\rho_{WC} = \frac{\dot{M}_{WC}}{4\pi r^2 v_{WC}^\infty}, \quad (4.21)$$

where r is the distance from the barycentre. This threshold value was set to $1.25\rho_{SW}$. Higher threshold values were found to be inaccurate at large distances from the barycentre. Other methods of detecting the WCR, such as determining wind mixing levels, were not successful in general.

4.4 Results

The first set of simulations were performed in order to assess whether the implemented cooling model would influence dust formation within the WCR. This was found to be the case. Figure 4.5 shows that with no cooling only a very small amount of dust formation occurs. Dust production in the radiative simulations is significantly higher, with the `fullcool` simulation having consistently higher dust formation rates than the `plasmacool` simulation. Figure 4.6 shows that at the temperatures present within the WCR, dust grains that are present can enhance the cooling, allowing the shocked gas to reach temperatures low enough for dust formation faster than if only plasma cooling was simulated.

In the case of the `fullcool` simulation, a peak dust formation rate of $7 \times 10^{-9} M_\odot \text{yr}^{-1}$ was calculated. This fluctuation appears to be due to dust forming mostly in high density instabilities (see Fig. 4.7). The average dust formation rate from these simulations is noted in Table 4.7. The observed rates are less than 0.1% of the theoretical maximum given by Eq. 4.20, which indicates that the average dust-to-gas ratio, z , in the WCR, does not exceed 10^{-3} .

As cooling is significant in the post-shock WR wind ($\chi_{WR} = 1.2$), further compression occurs, resulting in much higher post-shock densities (Fig. 4.8). This rapid cooling results in ideal conditions for dust formation, especially within high density instabilities. A similar effect for the OB wind is not observed, as radiative energy losses are not influential on the dynamics of the flow, due to the faster, significantly thinner stellar wind ($\chi_{OB} = 1915$). Fig. 4.9 shows that the `fullcool` simulation has a similar immediate-post shock temperature to an adiabatic model, but the shocked WR wind cools to the floor temperature within an extremely short timescale, allowing the nascent dust grains to grow. We also observe that simulations with wind have a markedly more mixed wind, due to thermal instabilities in the post-shock environment (Fig. 4.10). Fig. 4.11 shows that dust clumps form shortly after the initial wind collision. These

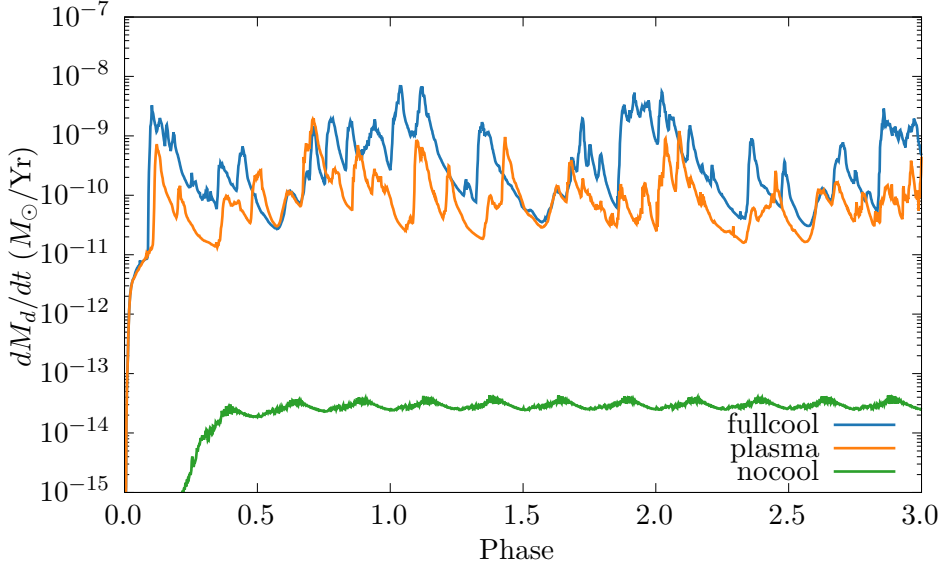


Figure 4.5: A comparison of the dust formation rates as the cooling mechanisms in the simulation are changed. Without adequate cooling barely any dust is formed. While dust formation increases with all cooling mechanisms enabled, plasma cooling is still the dominant cooling process between 10^4 and 10^9 K for dust production.

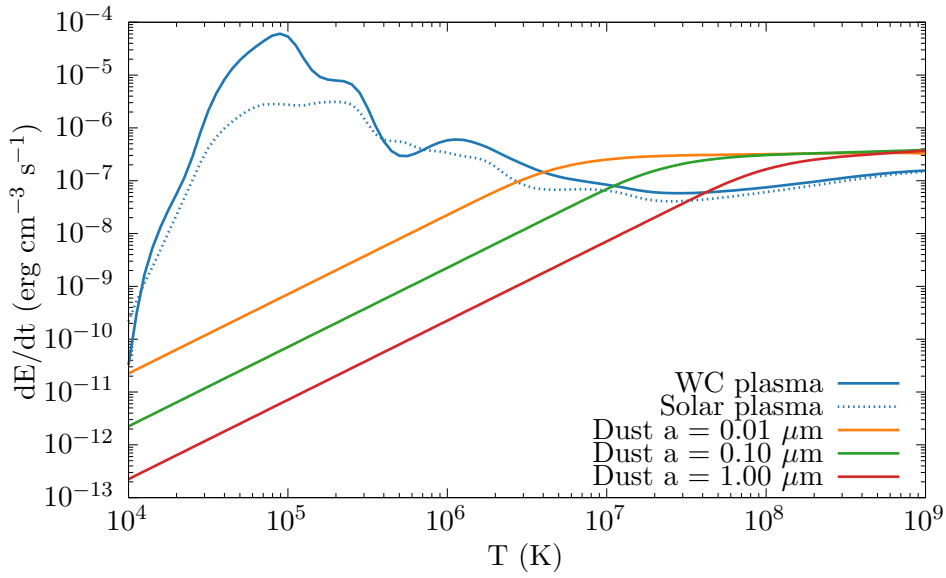


Figure 4.6: Comparison of the energy loss rate due to plasma and dust cooling with varying grain sizes, where $\rho_g = 10^{-16} \text{ g cm}^{-3}$ (typical of the density in the WCR) and a dust-to-gas mass ratio of 10^{-4} is assumed. Whilst less influential at lower temperatures, dust cooling can aid the overall cooling in the immediate high temperature post-shock environment.

4. AN EXPLORATION OF DUST FORMATION WITHIN WCD SYSTEMS

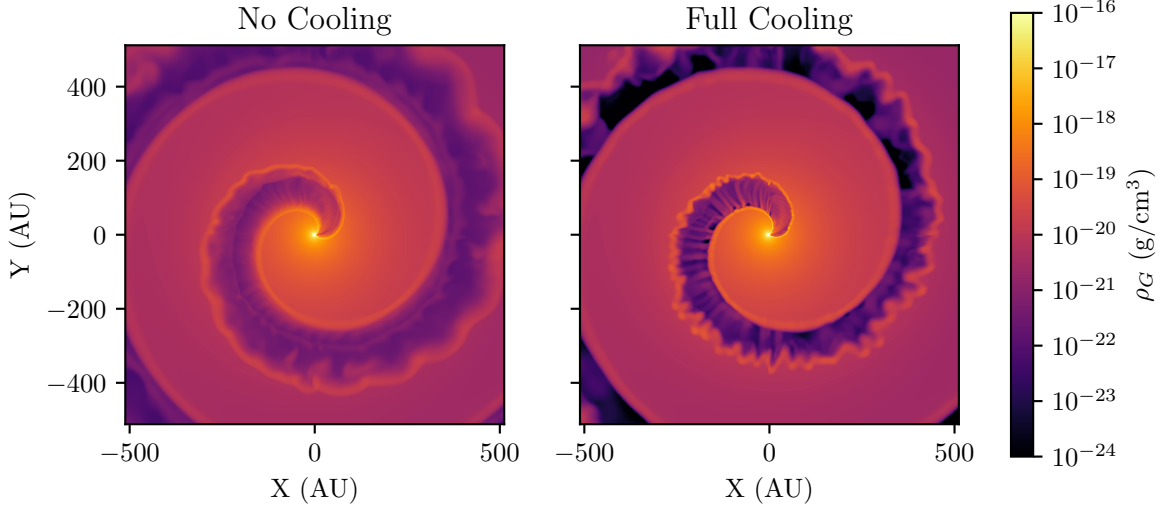


Figure 4.7: Density comparison in the orbital plane for the `nocool` and `fullcool` models. With cooling enabled instabilities are far more prevalent, with pockets of very high density material within the WCR.

clumps rapidly convert post-shock gas to dust. However, rapid dust production tapers off as the post-shock flow becomes more diffuse. This behaviour is similar to dust models described in Harries et al. (2004b) and Hendrix et al. (2016), which suggest that the bulk of dust formation occurs only a short distance from the parent stars. The post-shock temperature is significantly lower in the leading edge of the WCR relative to the orbital motion, leading to a larger portion of dust forming in this region.

Pittard (2009) notes that in the case of colliding winds with $\eta = 1$ the trailing edge of the WCR takes part in oblique shocks with the stellar winds, while the leading edge is shadowed by the upstream WCR from the colliding material. This results in a trailing edge with strong instabilities and cool, high density clumps of post-shock wind, while the leading edge has a low density flow that is not dominated by instabilities. This does not appear to occur in these low- η systems, as oblique shocks occur at a much greater distance, where the stellar wind is significantly less dense. Instead, the leading edge of the WCR appears to be much thinner and denser than the trailing edge. This is believed to be due to the leading edge interacting more strongly with the outflowing material due to the orbital motion of the stars, sweeping up material and obliquely shocking with the downstream WCR. Most of the dust formation then occurs in the downstream post-shock region of the trailing edge of the WCR, as soon as it has sufficiently cooled (Fig. 4.11). Furthermore, dust formation slows significantly as the post-shock wind begins to diffuse, limiting the dust formation to a region around 100 AU from the WCR

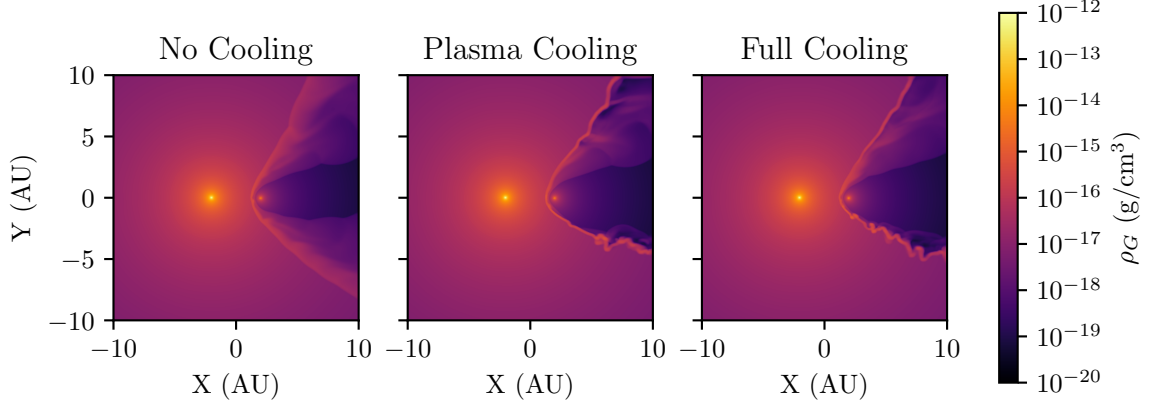


Figure 4.8: Density comparison in the orbital plane of simulations with differing radiative processes.

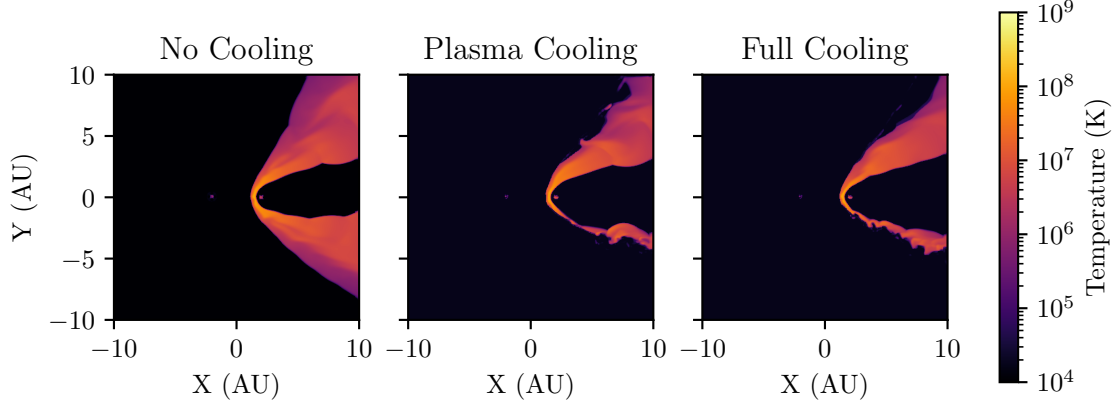


Figure 4.9: Temperature comparison in the orbital plane of simulations with differing radiative processes.

apex. This is in agreement with P. M. Williams, van der Hucht, Thé and Bouchet (1990) and Hendrix et al. (2016), who found that there is a limited region suitable for dust formation.

4.4.1 Mass loss rate variation

The dust formation rate in the mass loss variation simulations was found to be dependent on the strength of the WC or OB winds. As can be seen in Fig. 4.12 and Table 4.8, the rates are separated into similar dust production rates for simulations with increases or decreases in mass loss rates; simulations with either wind being stronger than the `baseline` simulation produced most dust, while simulations with weaker winds produced approximately 3 orders of magnitude less dust than the most productive simulations. This result appears to be proportional to

4. AN EXPLORATION OF DUST FORMATION WITHIN WCD SYSTEMS

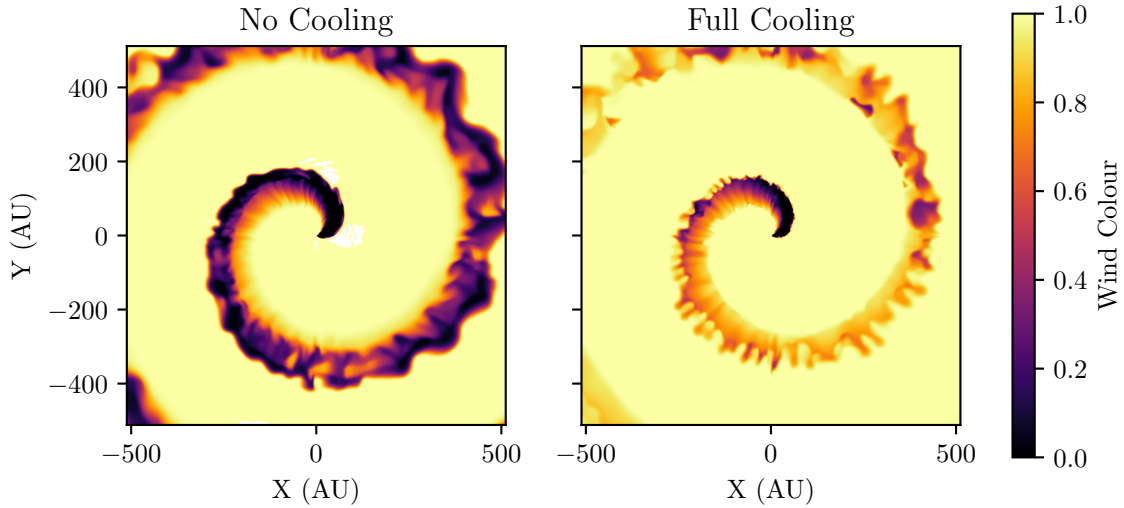


Figure 4.10: Wind “colour” for `nocool` and `fullcool` models. The WCR is more thoroughly mixed if the simulation is allowed to cool.

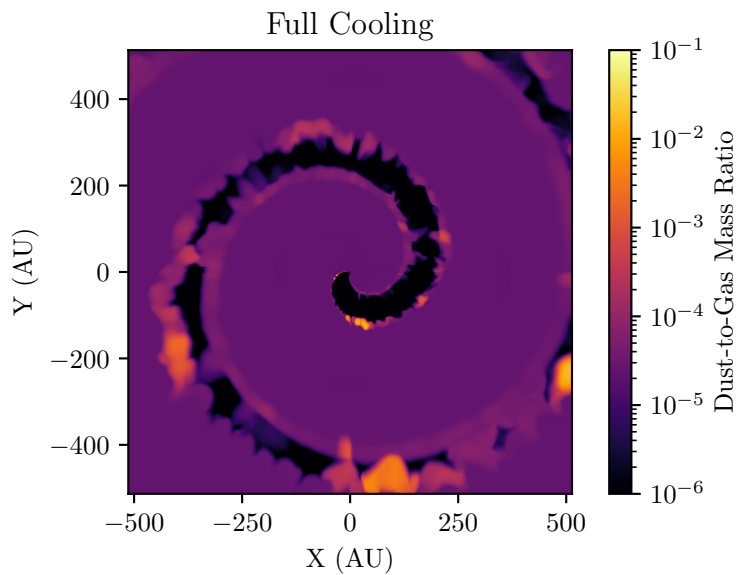


Figure 4.11: The full extent of the `baseline` simulation, showing the dust-to-gas mass ratio in the orbital plane. Dust typically forms in clumps within instabilities, leading to a variation of the dust formation rate as the simulation progresses. Most of the dust forms in the leading arm of the WCR.

4.4 Results

Model	η	χ_{WR}	χ_{OB}	$\dot{M}_{\text{d,avg}}$ $M_{\odot} \text{ yr}^{-1}$	$\dot{M}_{\text{d,max}}$ $M_{\odot} \text{ yr}^{-1}$
<code>fullcool</code>	0.02	1.20	1915	5.38×10^{-10}	9.06×10^{-7}
<code>plasmacool</code>	0.02	1.20	1915	1.29×10^{-10}	9.06×10^{-7}
<code>nocool</code>	0.02	1.20	1915	2.71×10^{-14}	9.06×10^{-7}

Table 4.7: Average rate of dust production for the set of different radiative simulations. $\dot{M}_{\text{d,max}}$ is the maximum expected dust formation rate (Eq. 4.20).

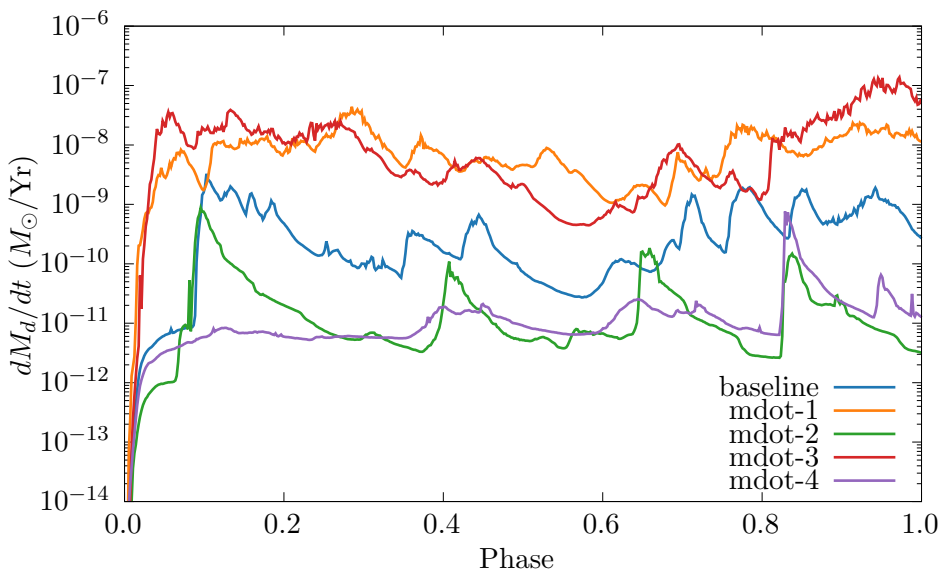


Figure 4.12: A comparison of the dust production rates for simulations that vary the mass loss rate, \dot{M} . Simulations with either a strong primary or secondary wind produce similar levels of dust, whilst if either wind is weaker, the dust production rate is reduced.

the wind momentum ratio. For instance, `mdot-1` and `mdot-3` produce on average two orders of magnitude more dust than the `baseline` simulation, these simulations have an identical value for η , but differ in total mass loss rate by a factor of 2. This suggests that a stronger shock can increase dust formation rate, due to higher post-shock densities and more cooling. Some of this value can be attributed to the changing number density of grains, particularly in simulations `mdot-1` and `mdot-2`, where grain number density increases and decreases by a factor of 2 respectively. In the case of `mdot-1` this doubles the number density of grains, increasing the amount of dust cooling and increases the number of grain nucleation sites for dust formation.

4. AN EXPLORATION OF DUST FORMATION WITHIN WCD SYSTEMS

Model	η	χ_{WR}	χ_{OB}	$\dot{M}_{\text{d,avg}}$ $M_{\odot} \text{ yr}^{-1}$	$\dot{M}_{\text{d,max}}$ $M_{\odot} \text{ yr}^{-1}$
baseline	0.02	1.20	1915	5.38×10^{-10}	9.06×10^{-7}
mdot-1	0.01	0.60	1915	8.79×10^{-9}	1.42×10^{-6}
mdot-2	0.04	2.39	1915	2.53×10^{-11}	5.83×10^{-7}
mdot-3	0.04	1.20	957	2.34×10^{-8}	1.17×10^{-6}
mdot-4	0.01	1.20	3830	3.81×10^{-11}	7.11×10^{-7}

Table 4.8: Average rate of dust production for the mass loss rate simulation set.

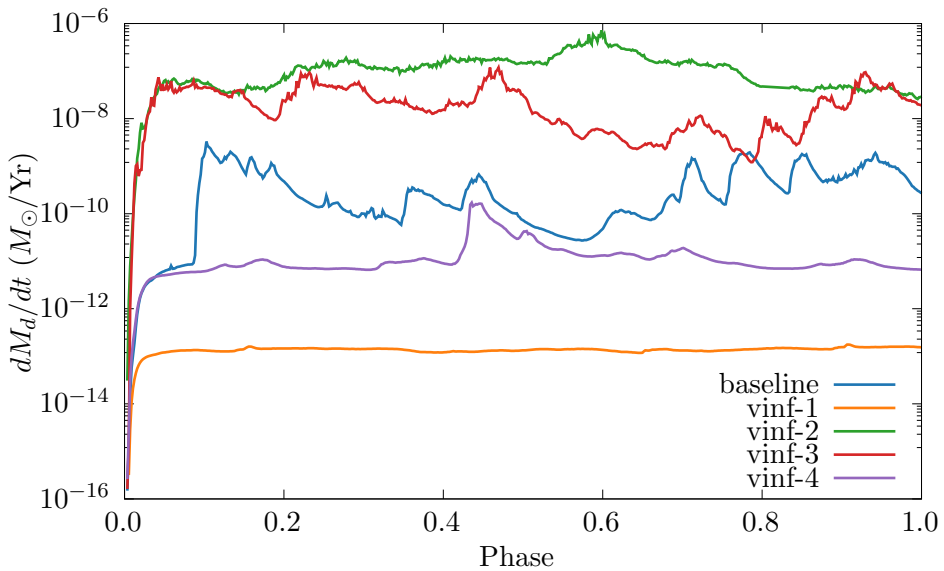


Figure 4.13: Comparison of the dust production rate for simulations varying the wind terminal velocity, v^{∞} . Simulations with a strong wind velocity imbalance produce significantly more dust than their counterparts.

4.4.2 Terminal velocity variation

Varying the wind terminal velocity also has an extremely strong effect on the dust formation (see Fig. 4.13 and Table 4.9). The dust production rate is exceptionally high in the case of $v_{\infty}-2$, which has an extremely slow wind velocity of 500 km s^{-1} , closer to that of a typical LBV star than that of a WC (Table 4.9). This very slow, dense wind experiences very strong radiative cooling in the post-shock environment ($\chi_{\text{WR}} = 0.07$), leading to high density pockets of cooled gas. This can be seen in Fig. 4.14, where $v_{\infty}-2$ produces large quantities of dust near the apex of the WCR on the WR side, which is then mixed throughout the WCR. The factor of 4 difference in the wind velocity between the WR and OB winds creates a very strong velocity shear, leading to the formation of Kelvin-Helmholtz instabilities.

It should be noted that the dust production in general increased *outside* of the WCR in the case of $v_{\infty}-2$ (i.e. in the unshocked WR wind). This is largely due to the significantly higher wind density within the WC wind, and the increase in the time for grain growth before the wind collision. Despite this, the dust production outside of the WCR does not dominate the total dust production rate, most of which occurs in the WCR still. In the numerical analysis (Fig. 4.13 and Table 4.9) of dust production we do not include dust produced outside of the wind collision region. In the case of a fast WC wind ($v_{\infty}-1$) with a largely adiabatic WCR, dust production effectively ceases, with an average dust production rate of $9 \times 10^{-14} M_{\odot} \text{ yr}^{-1}$, two orders of magnitude less than $v_{\infty}-4$, despite the latter having a similar wind momentum ratio.

Simulations $v_{\infty}-3$ and $v_{\infty}-4$ show that when the secondary wind velocity is altered, drastic changes to the dust formation rate again occur, which is partially due to the prevalence and strength of instabilities. A greater velocity shear along the discontinuity results in strong Kelvin-Helmholtz instabilities in $v_{\infty}-3$, whereas these are missing in $v_{\infty}-4$ which has equal wind speeds. Both $v_{\infty}-2$ and $v_{\infty}-3$ exhibit very strong KH instabilities, and both have a terminal velocity ratio, $v_{\text{OB}}^{\infty}/v_{\text{WR}}^{\infty} = 4$. This augments the already present thermal instabilities due to radiative cooling, leading to a less ordered, clumpy post-shock environment. In Fig. 4.15 where $v_{\infty}-3$ and $v_{\infty}-4$ are directly compared, the presence of a much faster secondary wind results in a velocity shear that produces a much broader WCR, with high density pockets formed within instabilities, which appear to produce the bulk of the dust, despite both simulations having an adiabatic second wind. This suggests that prolific dust formation occurs in a post-shock primary wind shaped by instabilities, produced either from strong radiative cooling, or through a strong velocity shear, leading to K-H instabilities. We note also that the dust formation rates

4. AN EXPLORATION OF DUST FORMATION WITHIN WCD SYSTEMS

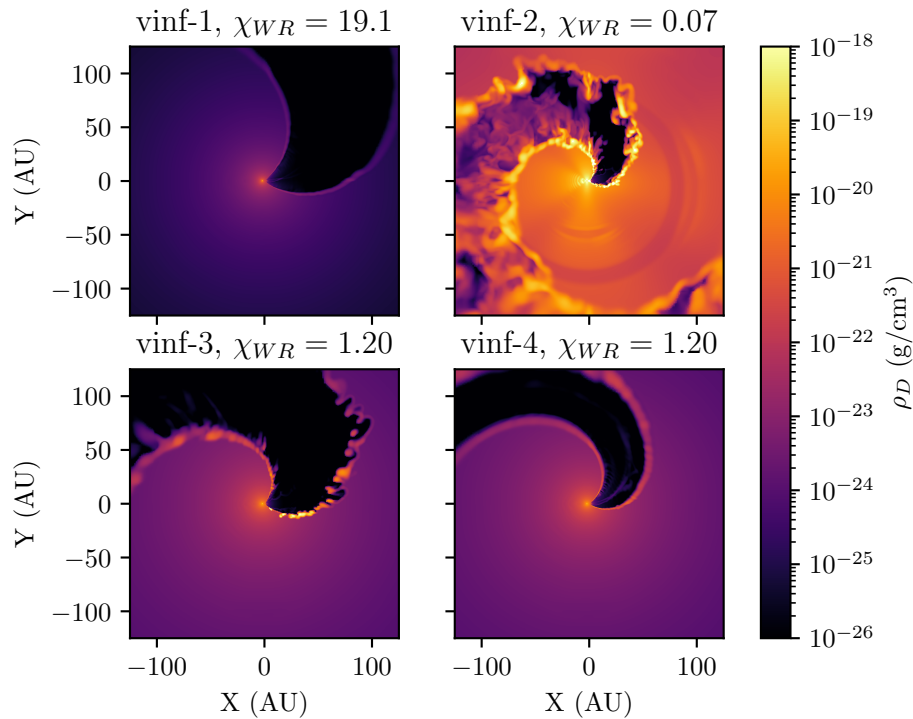


Figure 4.14: Comparison of the dust density in the simulations that vary v^∞ . Simulations with either a high OB wind velocity or low WC wind velocity produce large quantities of dust. Simulation **vinf-1**, which has a high velocity WC wind with $\chi_{WR} = 19.1$, does not produce any appreciable dust within the WCR. **vinf-1** and **vinf-4** have a smoother WCR with less instabilities as both winds have identical terminal speeds, resulting in no velocity shear.

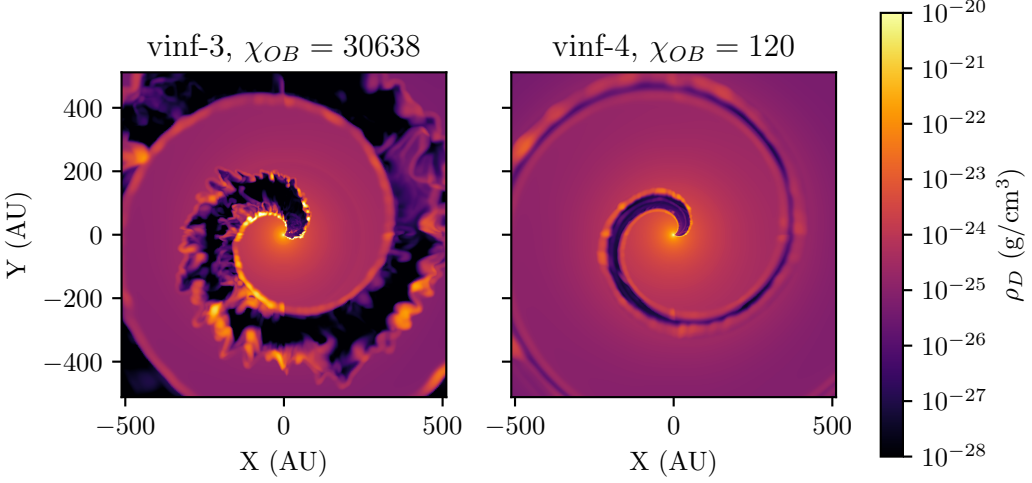


Figure 4.15: Comparison of the dust density in simulations with modified OB wind terminal velocities. The simulations are fully advected with 3 orbits calculated. Dust formation and instabilities are far more pronounced in vinf-3, which has an OB wind velocity a factor of 4 larger than vinf-4.

Model	η	χ_{WR}	χ_{OB}	$\dot{M}_{\text{d},\text{avg}}$ $M_{\odot} \text{ yr}^{-1}$	$\dot{M}_{\text{d},\text{max}}$ $M_{\odot} \text{ yr}^{-1}$
baseline	0.02	1.20	1915	5.38×10^{-10}	9.06×10^{-7}
vinf-1	0.01	19.1	1915	8.88×10^{-13}	7.11×10^{-7}
vinf-2	0.04	0.07	1915	1.17×10^{-7}	1.17×10^{-6}
vinf-3	0.04	1.20	30638	6.30×10^{-11}	1.17×10^{-6}
vinf-4	0.01	1.20	120	1.94×10^{-8}	7.11×10^{-7}

Table 4.9: Average rates of dust production for the terminal velocity simulation set.

appear to be stratified somewhat in terms of η . Simulations where $\eta = 0.04$ produce significantly more dust than simulations with more imbalanced winds (Fig. 4.13).

By directly comparing two prolific dust producing models with $\eta = 0.04$, models vinf-3 and mdot-3, we can see that both WCRs are dominated by instabilities. However, of the two, vinf-3 is more thoroughly mixed (Fig. 4.16). In particular, it has a much larger trailing edge that produces large quantities of dust (Fig. 4.17). These simulations produce approximately the same amount of dust, with vinf-3 also consistently producing dust in the trailing edge of the WCR. From these results it is clear that the dust production rate is increased if there is a highly imbalanced wind velocity (with a slow WC and fast OB wind), as this leads to a post-shock environment governed by thin-shell and Kelvin-Helmholtz instabilities.

4. AN EXPLORATION OF DUST FORMATION WITHIN WCD SYSTEMS

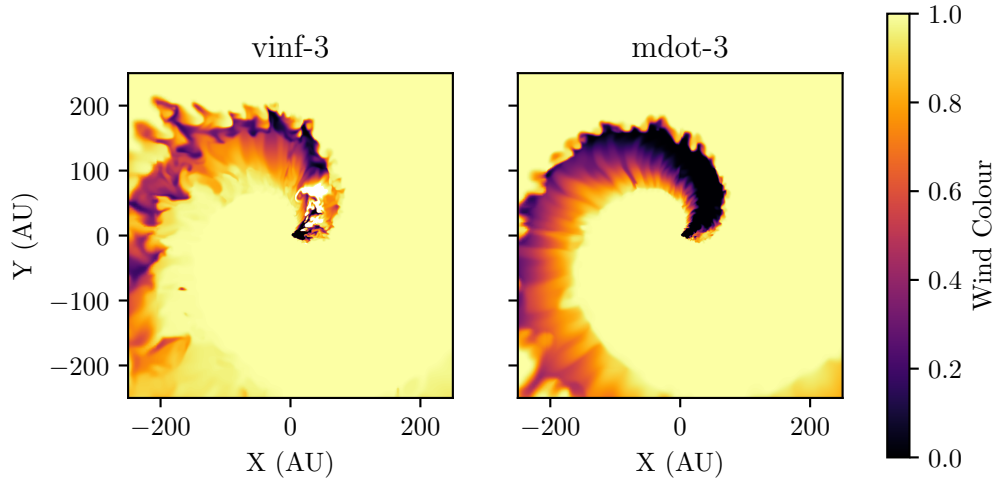


Figure 4.16: Comparison of the wind colour in simulations `vinf-3` and `mdot-3`. The WR wind has a colour of 1.0 while the OB wind has a colour of 0.0. Wind mixing is significantly more pronounced in `vinf-3` than in `mdot-3`, with a post-shock WR wind that is strongly influenced by Kelvin-Helmholtz instabilities, due to the increased wind velocity imbalance and lower degree of cooling.

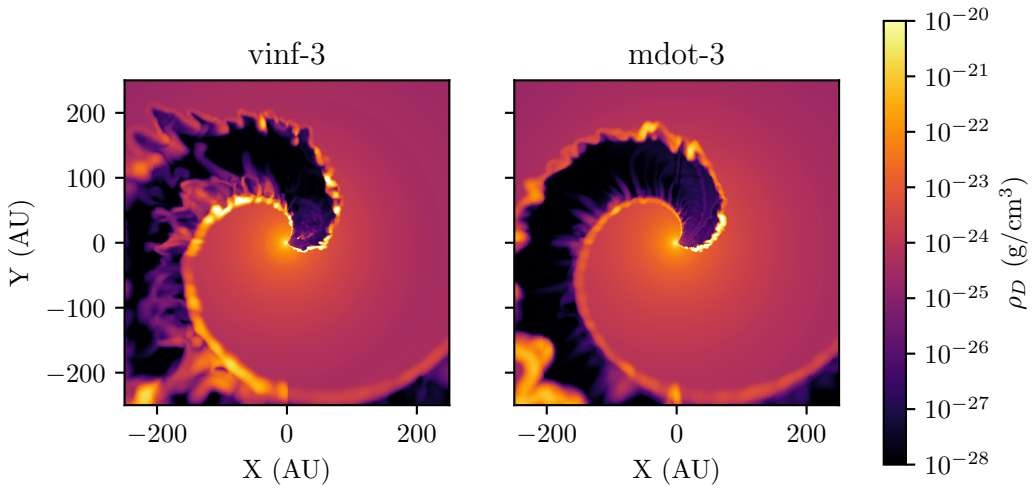


Figure 4.17: Comparison of the dust density in simulations with a strong secondary wind, models `vinf-3` and `mdot-3`. Dust in `vinf-3` is produced to a much higher degree in the trailing edge of the wind rather than on the leading edge of the simulation as in `mdot-3`. The increased mixing of the wind in `vinf-3` due to Kelvin-Helmholtz instabilities has led to dust forming throughout the WCR, rather than being concentrated near the apex of the WCR.

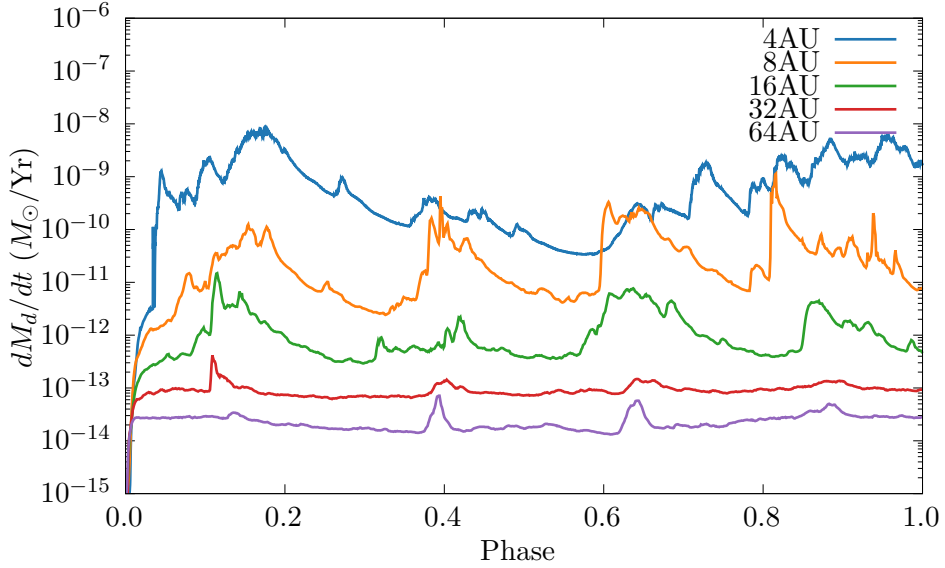


Figure 4.18: A comparison of dust formation rates versus orbital phase for a set of simulations that vary the separation of the stars, d_{sep} . A clear inverse relationship between separation distance and dust production rate exists, due to a WCR that behaves more adiabatically.

4.4.3 Separation variation

There is a clear correlation between the separation distance of the stars and the dust formation rate, with dust production drastically increasing as the orbital separation is decreased (Fig. 4.18 and Table 4.10). This influence on the dust formation rate is non-linear, with a doubling of the separation distance decreasing the dust production rate by approximately one order of magnitude. Clearly, dust formation is strongly influenced by the wind density at collision and the strength of the post-shock cooling. The variability of the dust production rate also appears to increase as the separation distance is reduced, leading to instances where a simulation may temporarily produce more dust than a simulation with a tighter orbit, such as the case with $d_{\text{sep}}=4\text{AU}$ and $d_{\text{sep}}=8\text{AU}$ at an orbital phase of $0.6 < \Phi < 0.65$. As we have previously discussed, instabilities drive slightly intermittent, but highly efficient dust formation, which cause these fluctuations (Fig. 4.19). Our results are consistent with observations of episodic dust forming systems, where infrared emission due to dust is maximised at or shortly after periastron passage.

4. AN EXPLORATION OF DUST FORMATION WITHIN WCD SYSTEMS

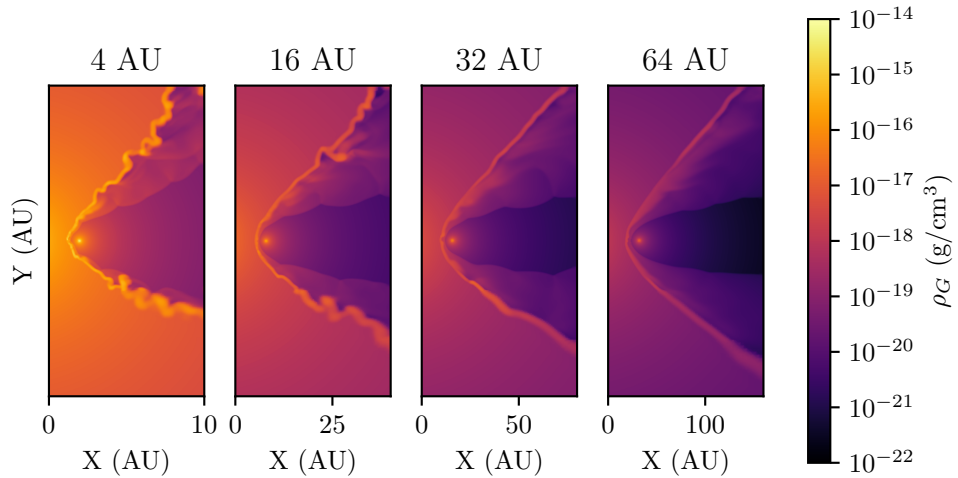


Figure 4.19: A comparison of the structures of simulations varying d_{sep} . The scale of each plot has been changed to allow for a similar feature size. Simulations with a closer stellar separation have collision regions whose structure is more strongly influenced by instabilities. In particular by thin-shell instabilities brought on by the radiative behaviour in the WCR.

Model	η	χ_{OB}	$\dot{M}_{\text{d,avg}}$ $M_{\odot} \text{ yr}^{-1}$	$\dot{M}_{\text{d,max}}$ $M_{\odot} \text{ yr}^{-1}$
baseline	1.20	1915	5.38×10^{-10}	9.06×10^{-7}
dsep-8AU	2.39	3830	4.39×10^{-11}	9.06×10^{-7}
dsep-16AU	4.79	7659	1.77×10^{-12}	9.06×10^{-7}
dsep-32AU	9.57	15319	8.83×10^{-14}	9.06×10^{-7}
dsep-64AU	19.1	30638	2.41×10^{-14}	9.06×10^{-7}

Table 4.10: Average rates of dust production for the separation distance simulation set. The stellar parameters are the same as in the **baseline** model, which has a $d_{\text{sep}} = 4.0 \text{ AU}$

4.5 Conclusions

The simulations in this paper were conducted over a fairly limited parameter space of mass loss rates and wind terminal velocities. Despite this, the dust production rate varied by up to 6 orders of magnitude. Dust formation was found to be extremely sensitive to the wind properties of both stars, which imposes a limited range of wind parameters for dust to form efficiently. This would explain why these dust forming systems are comparatively rare, compared to the total number of systems with massive binary stars and interacting winds, and also why periodic dust forming systems have eccentric orbits. The baseline system, which is representative of WR98a, has a significantly lower stellar mass loss rate than other well-characterised WCd systems, such as WR140 and WR104. Future simulations will focus on these other systems to explore how closely they match observations.

4.5.1 Wind mixing within the WCR

While interaction between hydrogen and dust grains is not simulated by the dust model, elements such as hydrogen are crucial for forming complex organic molecules. As the WC wind is extremely hydrogen-poor, significant wind mixing would need to occur (Herbst & van Dishoeck, 2009). Figure 4.10 shows that the wind is far more effectively mixed by instabilities if it is sufficiently radiative. An improved dust model which can calculate grain yields from chemical reactions could be used to investigate this further. Conveniently, implementation of a chemical model into Athena++ through passive scalars is a future feature in the projects roadmap. Additionally, a multi-fluid model could be used to model the dynamics of grains, as larger grains may not necessarily be co-moving in a turbulent wind environment.

4.6 Summary

Our parameter space exploration of colliding wind binary systems undergoing dust formation yields new insights into how dust forms within the WCR. Dust production within these systems is poorly understood, and with direct observations of the WCR rendered difficult by the extreme conditions of these systems, it falls on numerical simulation to elucidate the nature of dust production in CWBs. Our simulations reveal how sensitive to changing wind conditions this dust production is. This parameter space exploration, whilst quite conservative, resulted in a

4. AN EXPLORATION OF DUST FORMATION WITHIN WCD SYSTEMS

change in dust formation rates of up to 6 orders of magnitude. In all simulations, the bulk of dust formation was found to occur within high-density pockets formed through thin-shell or Kelvin-Helmholtz instabilities, suggesting that strong cooling and a fast secondary wind are both important factors for dust production. For high levels of dust formation, an ideal system should have a slow, dense primary wind and a fast, dense secondary wind, with a close orbit. This combination of properties ensures the formation of dense pockets of cool post-shock gas in which dust formation proceeds.

There is significant potential for additional research in this field. Parameter mixing was not performed, due to the simulation time required for producing many more simulations, but performing examples on more extreme systems, such as those with a LBV primary star or a WR+WR system is a potential avenue of research. Future work could introduce additional dust formation and destruction mechanisms, such as grain-grain collision or photodissociation. Modelling effects such as radiative line driving or use of a multi-fluid model could also prove fruitful. Another interesting avenue of research is the simulation of eccentric, periodic dust forming systems; simulating either an entire or a partial orbit of a system such as WR140 would be a logical next step for this work.

4.7 Acknowledgements

This work was undertaken on ARC4, part of the High Performance Computing facilities at the University of Leeds, UK. We would also like to thank P. A. Crowther for his work on the [Galactic Wolf-Rayet Catalogue¹](#).

¹pacrowther.staff.shef.ac.uk/WRcat

CHAPTER 5

Exploring dust formation in the episodic WCd system
WR140

5. EXPLORING DUST FORMATION IN WR140

5.1 Introduction

The dynamics of massive stars in binary systems is a particularly fascinating subject. These incredibly violent phenomena are obscured behind vast clouds of outflowing stellar wind, the result of the most massive stars we know slowly tearing themselves asunder. Colliding wind binary (CWB) systems were first hypothesised to explain highly luminous and variable x-ray emission in systems such as V444 Cyg and γ^2 Vel (Prilutskii & Usov, 1976). These extremely bright emissions were found to be due to stellar wind collision with shock velocities in the order of 10^3 km s^{-1} . The variability in x-ray emission can be explained if the phenomena occurs due to the orbit of a binary system, such as the Wind Collision Region (WCR) being occluded by the outflowing stellar wind, being occluded by the stars themselves. The system can also have an eccentric orbit, reducing the shock strength as the orbital separation, d_{sep} , varies. Despite this dust-hostile environment, CWB systems containing a Wolf-Rayet carbon phase star (WC) have been observed producing copious quantities of dust (so-called WCd systems). These systems typically convert around 1% of the stellar wind into dust a short time after wind collision; in more prolific systems such as WR104 up to 36% of the Wolf-Rayet (WR) outflow is converted into dust (Lau et al., 2020). This corresponds to dust production rates on the order of $10^{-6} M_{\odot} \text{ yr}^{-1}$, rivalling other profuse dust producing phenomena such as AGB stars.

WCd systems can sub-categorised further, into persistent, variable and episodic dust forming systems. Persistent systems, such as WR104 (Tuthill et al., 1999), produce dust at a constant rate, and as such produce extreme quantities of dust, as well as well-defined pinwheel patterns if the system is viewed face-on. Episodic systems, meanwhile, only produce dust for a limited period before entering a period of dormancy; this pattern is cyclical, and is predictably periodic. A good example of such an episodic system is WR140, the subject of this paper (P. M. Williams, van der Hucht, Pollock et al., 1990). Variable systems have some characteristics of these two sub-types, having a distinct variability without a period of dust producing dormancy, such as WR98a (Monnier et al., 1999). Whether a system is persistent, variable or episodic is based on the systems orbital eccentricity, highly eccentric systems appear to form episodic systems, with the “active” dust production period occurring immediately after periastron passage, and a relatively short time thereafter. Meanwhile, persistent and variable systems have been observed to have more circular orbits, suggesting that the effect of a change in system separation distance, d_{sep} , has a role in dust formation. The initial mechanism behind dust formation is not well understood, whilst nascent amorphous carbon dust grain cores can form condense within the photosphere of

	Persistent		Variable		Episodic	
	Total	Example	Total	Example	Total	Example
WC4	1	WR19	0	—	0	—
WC5	0	—	0	—	1	WR47C
WC6	1	WR124-10	0	—	0	—
WC7	3	WR102-22	0	—	4	WR140
WC8	6	WR13	1	WR48a	3	WR122-14
WC9	45	WR104	6	WR98a	1	WR75-11
Total	56		7		9	

Table 5.1: Number of WCd systems with a known spectral type and dust formation type from the Galactic Wolf Rayet Catalogue (Rosslowe & Crowther, 2015). Systems with uncertain spectral types not included, while systems labelled “d” are included within the “persistent” category for their associated spectral type.

WC7-9 stars, these grain cores would be vaporised by UV flux of both stars. However, within the WCR these grains appear to flourish, observations of these systems show that infrared excess in wavelengths associated with amorphous grains is detected almost exclusively within the post-shock WCR (Soulain et al., 2018). Observations also indicate that dust formation occurs rapidly and close to the system, this requires strong radiative cooling for the immediate-post shock temperature to reduce from $\sim 10^8$ K to $\sim 10^4$ K (P. M. Williams, van der Hucht, Pollock et al., 1990; P. M. Williams et al., 1987). As such, dust formation appears to be encouraged in the WCR through a multitude of factors:

- The high density of the post-shock WCR results in a high collision rate between carbon atoms and dust grains.
- The WCR shields nascent dust grains from the bulk of the UV emission from the stars.
- The rapid cooling in the immediate post-shock environment reduces gas-grain sputtering.
- Strong radiative cooling drives the formation of thermal instabilities, which produces clumps of cool, high density gas where dust can rapidly grow.

This dust formation can also be influenced by orbital separation, velocity shear and momentum ratio imbalance between the winds, producing variability on the timescale of a single orbit, or $t_{\text{dyn}} \ll P$.

WCd systems are comparatively rare, out of 106 confirmed systems with a WR binary, only 9 are categorised as episodic WCd systems (Table 5.1). As these systems have a typical distance on the order of 1 – 10 kpc, this makes observation of WCds difficult. Whilst these systems

5. EXPLORING DUST FORMATION IN WR140

can be observed and the dusty WCR can be resolved, observation of the innermost, immediate post-shock dust forming region is not possible at this distance. As such, numerical simulation is necessary to determine dust formation in WCd systems, a contemporary example of such simulations is Hendrix et al. (2016), though simulation of the evolution of dust grains through cooling, growth and sputtering was not performed. In this paper we present a numerical simulation of the archetypical episodic WCd system WR140 with a co-moving dust model simulating grain growth and sputtering through gas-grain collisions. This simulation covers a temporal slice of the orbit of WR140 from phase $\Phi = 0.95$ to $\Phi = 1.10$, or the period immediately prior to and after periastron passage. We will discuss our methodology in Section 5.2, with a particular emphasis on our dust model in Subsection 5.2.2. Afterwards we will discuss the simulation and WR140 system parameters, as well as our data collection techniques in Section 5.3. Finally, we will discuss our results and conclude in Sections 5.4 and 5.5.

5.2 Methodology

The periodic dust forming system WR140 was simulated using a fork of the Athena++ hydrodynamical code (Stone et al., 2020), a series of modifications were implemented to simulate binary system orbits, stellar wind outflows and dust evolution. These simulations were conducted in 3D in a Cartesian co-ordinate system. The code solves a Riemann problem at each cell interface to determine the time-averaged values at the zone interfaces, and then solves the equations of hydrodynamics:

$$\frac{\partial \rho}{\partial t} + \nabla \cdot (\rho \mathbf{u}) = 0, \quad (5.1a)$$

$$\frac{\partial \rho \mathbf{u}}{\partial t} + \nabla \cdot (\rho \mathbf{u} \mathbf{u} + P) = 0, \quad (5.1b)$$

$$\frac{\partial \rho \varepsilon}{\partial t} + \nabla \cdot [\mathbf{u} (\rho \varepsilon + P)] = \frac{dE_{\text{cool}}}{dt}, \quad (5.1c)$$

where ε is the total specific energy ($\varepsilon = \mathbf{u}^2/2 + e/\rho$), ρ is the gas density, e is the internal energy density, P is the gas pressure and \mathbf{u} is the gas velocity. In order to simulate radiative losses, the parameter dE_{cool}/dt is included, which is the rate of energy loss rate per unit volume from the fluid due to gas and dust cooling.

Spatial reconstruction using a piecewise linear method was performed, while two strong

5.2 Methodology

stability Runge-Kutta methods were used for numerical integration, depending on the simulation stability. Several passive scalars are utilised to model wind mixing and dust evolution, the scalar values are transported by the fluid. For a given scalar species i , the scalar is advected through the scalar through the following equation:

$$\rho \frac{dC_i}{dt} = \frac{\partial}{\partial t} (\rho C_i) + \nabla \cdot (C_i \rho \mathbf{u}) = -\nabla \cdot \mathbf{Q}_i, \quad (5.2)$$

where \mathbf{Q}_i is the diffusive flux density ($\mathbf{Q}_i = -\nu_{ps}\rho\nabla C_i$) and ν is the passive scalar diffusion coefficient (Stone et al., 2020).

Stellar winds are simulated by modifying the density, ρ_R , momentum, p_R , and energy, E_R in a small region around both stars. Winds flow from this “remap” region at the stars wind terminal velocity, v^∞ . Remap zone parameters are calculated with the formulae

$$\rho_R = \frac{\dot{M}}{4\pi r^2 v_\infty}, \quad (5.3a)$$

$$p_R = \rho_R v_r, \quad (5.3b)$$

$$E_R = \frac{P_R}{\gamma - 1} + \frac{1}{2} \rho_R v_\infty^2, \quad (5.3c)$$

where P_R is the cell pressure ($P_R = \rho_R k_B T_w / \mu m_H$), T_w is the wind temperature, μ is the mean molecular mass, m_H is the mass of a hydrogen atom, v_R is the wind velocity as it flows radially from the center of the “remap zone” and r is the distance from the current cell to the centre of the remap zone. This method produces radially out-flowing winds from the star with an expected density and velocity. This method is stable against numerical instability, while also allowing us to precisely control the winds.

Line driving and wind acceleration effects are not simulated; instead, winds are instantaneously accelerated to their terminal velocity. Additionally, influence on the fluid from either gravitational self-interaction or interaction with the stars gravity wells are not simulated, with the stellar winds assumed to be travelling far in excess of the system escape velocity.

Athena++ utilises Message Passing Interface (MPI) parallelism. The numerical problem is broken into blocks, which are distributed between processing nodes on a High Performance Compute (HPC) cluster. The block size is variable, but for this simulation a block size of $40 \times 40 \times 10$ cells in XYZ was found to be optimal. Adaptive Mesh Refinement was considered for this simulation, however a known issue with the Athena++ code prevented this from being possible.

5. EXPLORING DUST FORMATION IN WR140

Passive scalars incorporated into the simulation were found to not be conserved along the interfaces between mesh blocks undergoing refinement, this meant that the simulation would rapidly exhibit unphysical behaviour (this bug is recorded as issue #365 on the Athena++ Github repository¹). A ring of refined cells across the orbital path was considered, but the performance improvements of this method were found to be negligible and not worth pursuing, as the block based refinement method of Athena++ would result in significant redundant refinement. Instead, a static mesh is used, where the stars predicted orbit over the simulation is refined to the maximum level, with a gradual de-refinement away from this refinement region.

5.2.1 Radiative cooling

Cooling is simulated via the removal of energy from a cell at each time-step. A cooling rate, for radiative emission from the stellar wind, dE_g/dt , is calculated and integrated using a sub-stepping Euler method. The number of sub-steps is determined by the estimated cooling timescale of the cell. Cooling due to gas and plasma emission in the stellar winds are calculated via individual lookup tables from each wind. These lookup tables contain the normalised emissivity, $\Lambda_w(T)$ at a logarithmically spaced series of temperatures from 10^4 K to 10^9 K. The cooling rate is determined for a cell by calculating the cell temperature and estimating $\Lambda_w(T)$ using linear interpolation between the nearest emissivity values in the lookup table. The energy loss is then calculated through the equation:

$$\frac{dE_g}{dt} = \left(\frac{\rho_g}{m_H} \right)^2 \Lambda_w(T), \quad (5.4)$$

where ρ_g is the gas density and m_H is the mass of hydrogen. The lookup table was generated by mixing a series of cooling curves from MEKAL simulations of elemental gasses. These curves were combined based on the elemental abundances in the WC and OB winds. To save calculation time, temperatures between 10^4 K $< T \leq 1.1 \times 10^4$ K are set to 10^4 K as they are assumed to be either rapidly cooling or a part of the stellar wind outside of the WCR. A minimum temperature of 10^4 K is defined by the simulation, as it is assumed that a radiating post-shock wind will tend to the temperature of the pre-shock wind, $T_{\text{final}} \rightarrow T_{\text{pre-shock}}$.

¹<https://github.com/PrincetonUniversity/athena/issues/365>

5.2.2 Dust model

In order to simulate dust evolution in WR140 a passive scalar dust model that simulates dust growth and destruction is included in the simulation. The dust model operates on passive scalars, and as such simulates dust that is co-moving with the stellar wind. Two scalars are used to describe dust in a cell, a , the grain radius in microns, and z , the grain dust-to-gas mass ratio

$$z = \frac{\rho_d}{\rho_g}, \quad (5.5)$$

where ρ_d is the dust density in the cell. A number of assumptions are made in this dust model; for instance, the dust grains in the model are spherical, with a uniform density. Dust grains are also assumed to have a single size in a region, as well as a constant number density. As such, this model does not simulate grain fracturing. Additional mechanisms for dust formation and destruction could also be implemented such as grain-grain agglomeration and photoevaporation. A multi-fluid model with drag force coupling could also be implemented, however this is beyond the scope of this paper.

Dust is grown through grain accretion using formulae described by (Spitzer, 2008) where dust grains grow via low-velocity collisions with surrounding carbon atoms, causing them to accrete onto the surface of the dust grain. Carbon is removed from the gas, reducing the cell density, while the corresponding dust density increases. This ensures that mass is preserved in the simulation. Assuming a single average grain size the rate of change in the grain radius in a cell, da/dt , is given by the equation:

$$\frac{da}{dt} = \frac{\xi \rho_C w_C}{4 \rho_{gr}}, \quad (5.6)$$

where ξ is the grain sticking factor, ρ_C is the carbon density ($\rho_C = X_C \rho_g$), w_C is the Maxwell-Boltzmann RMS velocity for carbon ($w_C = \sqrt{3k_B T / 12m_H}$), k_B is the Boltzmann constant and ρ_{gr} is the grain bulk density. The rate of change in grain mass due to accretion, $dm_{gr,ac}/dt$, is calculated with the formulae:

$$\frac{dm_{gr,ac}}{dt} = 4\pi \rho_{gr} a^2 \frac{da}{dt} = \pi \xi \rho_C w_C a^2, \quad (5.7)$$

A bulk density approximating that of amorphous carbon grains ($\rho_{gr} = 3.0 \text{ g cm}^{-3}$) is used for this simulation.

5. EXPLORING DUST FORMATION IN WR140

Dust destruction through gas-grain sputtering is calculated using the Draine and Salpeter (1979b) prescription. Within a flow of number density n_g a dust grain of radius a has a grain lifespan, τ_{gr} of:

$$\tau_{\text{gr}} = \frac{a}{\dot{a}} \approx 3 \times 10^6 \frac{a}{n_g} \text{ yr.} \quad (5.8)$$

This value is based on an average lifetime of carbon grains in an interstellar shock with a temperature of $10^6 \text{ K} \leq T \leq 3 \times 10^8 \text{ K}$ (Dwek et al., 1996; Tielens et al., 1994). The rate of change in the dust grain mass due to sputtering, $dm_{\text{gr,sp}}/dt$, can then be calculated with a similar formulae to the rate of change in grain mass due to accretion:

$$\frac{dm_{\text{gr,sp}}}{dt} = 4\pi\rho_{\text{gr}}a^2\frac{da}{dt} = -4\pi\tau_{\text{gr}}n_ga^2. \quad (5.9)$$

Finally, the total rate of change in grain mass is calculated, the overall change in dust density is then calculated through the equation:

$$\frac{d\rho_d}{dt} = \left(\frac{dm_{\text{gr,acc}}}{dt} + \frac{dm_{\text{gr,sp}}}{dt} \right) n_d, \quad (5.10)$$

where n_d is the dust grain number density.

Cooling via emission of photons from dust grains is also included in this model. The rate of cooling is calculated using the uncharged grain case of the prescription described in Dwek and Werner (1981). Grains are collisionally excited by collisions with ions and electrons, causing them to radiate. Similarly to the gas/plasma emission model used, the emitted photons are not re-adsorbed by the WCR medium, causing energy to be removed from the simulation. This therefore makes the assumption that the WCR is optically thin to far-infrared photons, which is observationally correct (Callingham et al., 2019; Monnier et al., 2007; Soulain et al., 2018). The grain heating rate, H_{coll} , in erg s^{-1} for a dust grain is calculated with the formulae:

$$H = 1.26 \times 10^{-19} \frac{n_g}{A^{1/2}} a^2 (\mu\text{m}) T^{3/2} h(a, T), \quad (5.11)$$

where n_g is the gas number density, A is the mass of the incident particle in AMU, $a(\mu\text{m})$ is the grain radius in microns, T is the temperature of the ambient gas, and $h(a, T)$ is the effective grain heating factor. Individual heating rates for hydrogen, helium, carbon, nitrogen and oxygen are calculated, in order to calculate the total ion collisional heating, H_{coll} :

5.2 Methodology

$$H_{\text{coll}} = H_{\text{H}} + H_{\text{He}} + H_{\text{C}} + H_{\text{N}} + H_{\text{O}}. \quad (5.12)$$

The effective grain heating factor for each element is calculated via the equation:

$$h(a, T) = 1 - \left(1 + \frac{E^*}{2k_{\text{B}}T}\right) e^{-E^*/k_{\text{B}}T}, \quad (5.13)$$

where E^* is the critical energy required for the particle to penetrate the dust grain (Table 5.2). The rate of heating due to electron-grain collisions, H_{el} , is similar to Eq. 5.11. The grain heating factor for electron collisions, h_e , is calculated via an approximation rather than the exact calculation in the case of baryonic matter. This approximation is performed as a complex integration for every cell and cooling step would need to be performed instead, which was found to take up $> 90\%$ of the processing time per cell. h_e is estimated through the following conditions:

$$\begin{aligned} h_e(x^*) &= 1, & x^* &> 4.5, \\ &= 0.37x^{*0.62}, & x^* &> 1.5, \\ &= 0.27x^{*1.50}, & \text{otherwise,} \end{aligned} \quad (5.14)$$

where $x^* = 2.71 \times 10^8 a^{2/3} (\mu\text{m})/T$. This approximation differs from the integration method by less than 8% while being 3 orders of magnitude faster. Excitation due to grain-grain collisions were not modelled, due to the limitations of the passive scalar model. In order to calculate the change in energy due to dust cooling, we find the radiative emissivity for dust, $\Lambda_d(T, a)$, to be

$$\Lambda(T, a) = \frac{H_{\text{coll}} + H_{\text{el}}}{n_{\text{H}}}, \quad (5.15)$$

where n_{H} is the number density of hydrogen in the gas. The energy loss rate from dust cooling, dE_{d}/dt , then calculated with the equation:

$$\frac{dE_{\text{d}}}{dt} = n_{\text{T}} n_{\text{d}} \Lambda_d(T, a), \quad (5.16)$$

and added to the gas/plasma energy loss rate, such that the total energy loss rate is:

$$\frac{dE_{\text{cool}}}{dt} = \frac{dE_{\text{g}}}{dt} + \frac{dE_{\text{d}}}{dt}. \quad (5.17)$$

5. EXPLORING DUST FORMATION IN WR140

Particle	E^*
e^-	$23 a^{2/3} (\mu\text{m})$
H	$133 a (\mu\text{m})$
He	$222 a (\mu\text{m})$
C	$665 a (\mu\text{m})$
N	$665 a (\mu\text{m})$
O	$665 a (\mu\text{m})$

Table 5.2: Grain critical energy, E^* , for a dust grain of a in μm for electrons, e^- , as well as the elements considered for grain cooling. The values for carbon, oxygen and nitrogen are identical.

5.3 System parameters

The authors of this paper have previously simulated WCd systems in the form of a parameter space exploration, in order to discern which wind and orbital parameters are influential on these systems dust formation rates. It was determined that the primary factors of dust formation in a WCd system were the mass loss rates, \dot{M} , and wind terminal velocities, v^∞ , for each star, as well as the orbital separation, d_{sep} . In particular, it was found that imbalances between the wind velocity produced Kelvin-Helmholtz (KH) instabilities due to a shear in the winds. Slower winds were found to be more radiative in the post-shock WCR flow, cooling to temperatures suitable for dust formation, this was found to influence the dust formation rate by as much as six orders magnitude through a factor of four variation of the WR wind terminal velocity. The authors also found that increasing d_{sep} significantly reduced the dust production rate, due to less intensive shocks as the out-flowing winds became less dense with distance. In the case of WCd systems with eccentric orbits, the separation distance can vary significantly. In the case of WR140, d_{sep} varies by a factor of 18 from apastron to periastron, which was hypothesised to be the primary cause of dust production variability within episodic systems. As \dot{M} does not vary significantly on the orbital timescale of these systems, this is not expected to impact the dust formation rate in episodic systems, while the wind velocity can diverge somewhat due to radiative inhibition and orbital motion.

In order to understand the structure and dynamics of the CWB system we must define some important parameters, such as the wind momentum ratio, η , which is defined as:

$$\eta = \frac{\dot{M}_{\text{OB}} v_{\text{OB}}^\infty}{\dot{M}_{\text{WR}} v_{\text{WR}}^\infty}. \quad (5.18)$$

As η decreases we find that the wind becomes more imbalanced, in the case of WR+OB CWB

5.3 System parameters

systems we find that the WR stars wind typically dominates the WCR. Assuming that there is no radiative inhibition (Stevens & Pollock, 1994) or radiative braking (Gayley et al., 1997), we can approximate the WCR to a conical region with an opening angle:

$$\theta_c \simeq 2.1 \left(1 - \frac{\eta^{2/5}}{4} \right) \eta^{-1/3} \quad \text{for } 10^{-4} \leq \eta \leq 1, \quad (5.19)$$

to a relatively high degree of accuracy (Eichler & Usov, 1993). Another important value for determining the evolution of a CWB system is the cooling parameter, χ , which is the ratio of the time taken for the shocked wind to completely cool to the time taken for the wind to escape the shock region:

$$\chi = \frac{t_{\text{cool}}}{t_{\text{esc}}} \approx \frac{v_8^4 d_{12}}{\dot{M}_{-7}}, \quad (5.20)$$

where v_8 is the wind terminal velocity in units of 10^8 cm s^{-1} , d_{12} is the separation distance in units of 10^{12} cm and \dot{M}_{-7} is the wind mass loss rate in units of $10^{-7} M_\odot \text{ yr}^{-1}$ (Stevens et al., 1992). As χ decreases, the structure of the WCR becomes more influenced by radiative instabilities, and has a post-shock temperature approaching the initial wind temperature. If $\chi < 1$, the WCR is completely dominated by instabilities, while if $\chi \gg 1$, the system behaves adiabatically. If the WCR is highly radiative the post-shock compression can be significantly greater than the adiabatic limit of $\rho_{\text{post-shock}} = 4\rho_{\text{pre-shock}}$, which facilitates dust production. Finally, we define a maximum dust production rate of the system, $\dot{M}_{d,\text{max}}$, assuming a 100% conversion rate of WR wind in the WCR into dust. The fraction of the WR wind that is passed through the WCR is given by the equation:

$$f_{\text{WR}} = \frac{1 - \cos(\theta_{\text{WR}})}{2}, \quad (5.21)$$

where θ_{WR} is the opening angle of the WR shock front ($\theta_{\text{WR}} \approx 2 \tan^{-1}(\eta^{1/3}) + \pi/9$). $\dot{M}_{d,\text{max}}$ is then calculated with the formulae:

$$\dot{M}_{d,\text{max}} = \dot{M}_{\text{WR}} X_{\text{C,WR}} f_{\text{WR}}, \quad (5.22)$$

where X_{C} is the carbon mass fraction in the WR star (Pittard & Dawson, 2018).

5. EXPLORING DUST FORMATION IN WR140

Parameter	Value	Citation
M_{WR}	$10.31 M_{\odot}$	Thomas et al. (2021)
M_{OB}	$29.27 M_{\odot}$	Thomas et al. (2021)
P	7.926 yr	Thomas et al. (2021)
e	0.8993	Thomas et al. (2021)
\dot{M}_{WR}	$5.6 \times 10^{-5} M_{\odot} \text{ yr}^{-1}$	P. M. Williams, van der Hucht, Pollock et al. (1990)
\dot{M}_{OB}	$1.6 \times 10^{-6} M_{\odot} \text{ yr}^{-1}$	P. M. Williams, van der Hucht, Pollock et al. (1990)
v_{WR}^{∞}	$2.86 \times 10^3 \text{ km s}^{-1}$	P. M. Williams, van der Hucht, Pollock et al. (1990)
v_{OB}^{∞}	$3.20 \times 10^3 \text{ km s}^{-1}$	P. M. Williams, van der Hucht, Pollock et al. (1990)
η	0.031	Calculated
χ_{\min}	2.69	Calculated

Table 5.3: The system parameters for the WR140 system as used in this paper. Citations for each parameter are provided.

Element	Solar	WC
X_{H}	0.705	0.000
X_{He}	0.275	0.546
X_{C}	0.003	0.400
X_{N}	0.001	0.000
X_{O}	0.010	0.050

Table 5.4: Abundances used for the OB and WR stars being simulated. Other elements are assumed to be trace when calculating dust emission (P. M. Williams et al., 2015).

5.3.1 WR140 parameters

WR140 was simulated in this paper as it is an archetypical example of an episodic WCd system. The system has an extremely eccentric orbit, which significantly effects the cooling parameter as the orbit progresses, and is also observed in detail and orbits face-on relative to the Earth. Though this simulation does not calculate wind acceleration due to radiative line driving, both stellar winds are expected to be accelerated to close to their terminal wind velocities (Lamers & Cassinelli, 1999). However, this discrepancy should be noted when considering the results of this paper.

Recent improved estimations of the orbital parameters of WR140 by Thomas et al. (2021) were used to calculate the orbital path for these simulations, while the mass loss rate, and the wind terminal velocity were derived from P. M. Williams, van der Hucht, Pollock et al. (1990) (Table 5.3). A typical wind composition for WC stars was assumed for the Wolf-Rayet star, while a solar abundance was assumed for the OB star (Table 5.4). The system orbit was calculated using a Keplerian orbital model with the two stars as point-masses.

5.3.2 Simulation parameters

A domain of $128 \times 128 \times 16$ AU was used for this simulation, with a coarse (0^{th} level) simulation resolution of $400 \times 400 \times 50$ in the XYZ domain. The simulation has 4 refinement levels, corresponding to an effective resolution of $6400 \times 6400 \times 800$ cells and a cell size of 0.02^3 AU. At periastron passage this results in ~ 80 cells separating the stars, which was found to be enough to adequately resolve the WCR. This simulation has an XYZ aspect ratio of 8:8:1 in order to reduce processing time, as the bulk of dust formation was expected to occur a short distance from the WCR. Due to computing limitations, a complete orbit could not be completed without AMR, instead, a section of the systems orbit, corresponding to an orbital phase of $0.95 \leq \Phi \leq 1.10$ was simulated (Fig. 5.1). This represents a period of approximately 1.2 years of the systems orbit, and the period where much of the dust forms, prior to and shortly after periastron passage (Crowther, 2003). Fig. 5.2 shows the orbital path overlaid onto the statically refined numerical grid, the area of maximum refinement is around the orbital paths of the stars from $0.94 \leq \Phi \leq 1.11$, in order to ensure that the stars are maximally refined. If the stars leave the regions that are refined to either the 3^{rd} or 4^{th} level unphysical behaviour with regards to wind mapping and dust formation occur, as such the simulation is halted when $\Phi = 1.10$. The simulation was run with two different numerical integrators, a 3^{rd} order accurate Runge-Kutta integrator, `rk3`, and a 4^{th} order accurate, 5-stage, 3 storage register strong stability preserving Runge-Kutta integrator, `ssprk5_4` (Ruuth & Spiteri, 2005). The `ssprk5_4` integrator was found to be approximately 60% slower, but markedly more stable. Prior to periastron passage the `rk3` integrator was used for its speed, but increasing numerical instability as the stars grew closer resulted in this proving untenable, and was switched to `ssprk5_4`.

Over periastron passage the average time-step was found to reduce by an order of magnitude, resulting in a corresponding increase to simulation time. At the most numerically complex portion of the simulation, a Courant number of $C = 0.04$ had to be used instead of the initial value of $C = 0.15$, in order to preserve numerical stability. As the simulation moved past periastron the Courant number was increased every 24 hours of wall time, until C returned to the initial value. The simulation was conducted on the ARC4 HPC cluster at the University of Leeds with 128 cores. The code was compiled using the Intel ICPC compiler using AVX512 optimisations and the Intel MPI library.

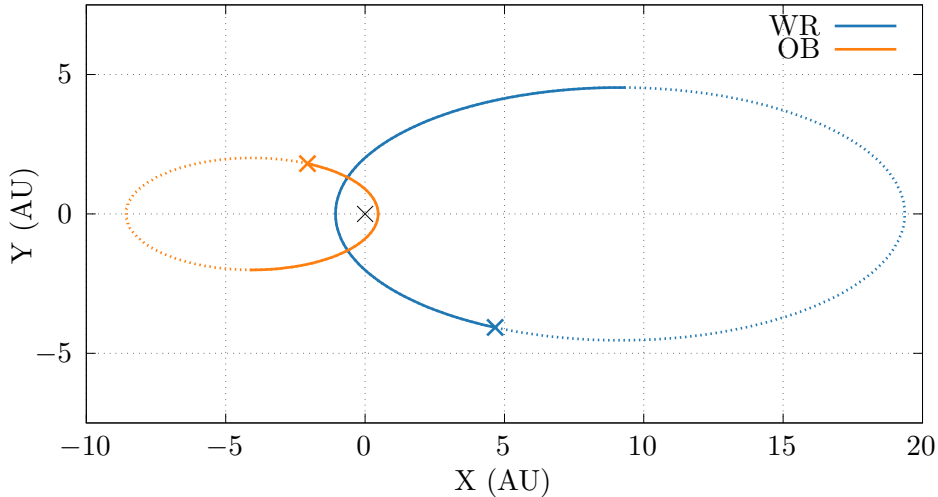


Figure 5.1: Simulation orbital trajectories of the WC7 and O5 stars in WR140. The solid lines represent the orbital phase being simulated, corresponding to $0.95 \leq \Phi \leq 1.10$, while the dashed lines represent the full orbital trajectory. The starting position for each star and the orbital barycentre at $(0,0)$ have been annotated.

5.3.3 Data collection

Simulation data was exported as HDF5 files at regular time intervals. 3D meshes were collected every increment of $\delta\Phi = 1.5 \times 10^{-3}$, while 2D slices in the XY plane were collected every increment of $\delta\Phi = 1.5 \times 10^{-4}$. These HDF5 files contain the primitive variables of the simulation: gas density, ρ , gas pressure, P , and wind velocity components, v_x , v_y and v_z . These variables were then used to derive other variables such as temperature and energy. The scalars governing the dust properties were also stored for each cell: the dust-to-gas mass ratio, z , and the dust grain radius, a . The wind “colour”, the proportion of gas from each star, was also stored. A value of 1.0 indicates a pure WR wind while 0.0 indicates a pure OB wind. The volume-weighted totals of all parameters of interest were also collected, such as the average values for z , a and the dust production rate within the WCR, \dot{M}_d . To calculate \dot{M}_d , a cell must be identified as being within the WCR, this was performed by comparing the cell density to the predicted density of a single wind with the wind parameters of the WC star in the system. Any cell with a density higher a certain threshold value was flagged as being within the WCR. the single-wind density, ρ_{SW} , was calculated using the equation:

5.3 System parameters

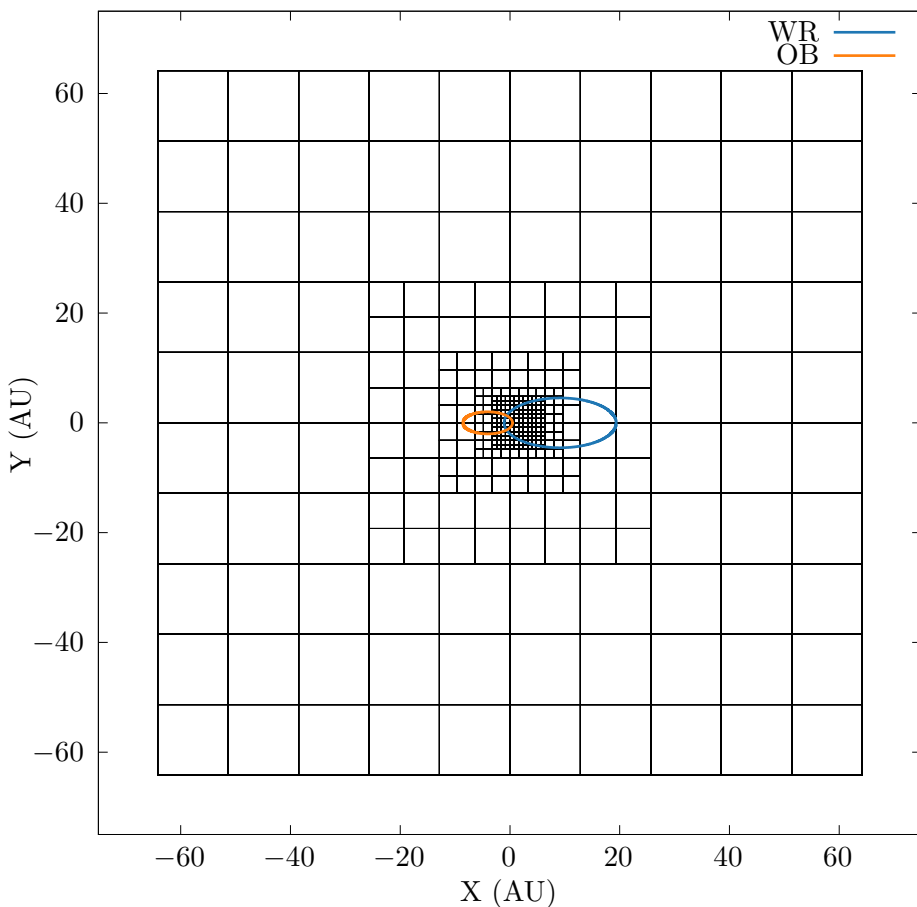


Figure 5.2: Numerical grid of the WR140 system simulation, static mesh refinement was used to increase the resolution around the orbital path from $0.95 \leq \Phi \leq 1.10$. The orbital path of both stars are overlaid onto this numerical grid. While the stars in the system can be within cells that are not fully refined, if there is insufficient resolution the stars begin to break down. As such the stars are typically in the 3rd or 4th level.

5. EXPLORING DUST FORMATION IN WR140

Parameter	Mean	Maximum
\dot{M}_d ($M_\odot \text{ yr}^{-1}$)	7.68×10^{-8}	1.24×10^{-6}
\bar{a} (μm)	1.32×10^{-2}	1.44×10^{-2}
\bar{z}	3.98×10^{-4}	3.32×10^{-3}

Table 5.5: Advected scalar yields from the WR140 simulation.

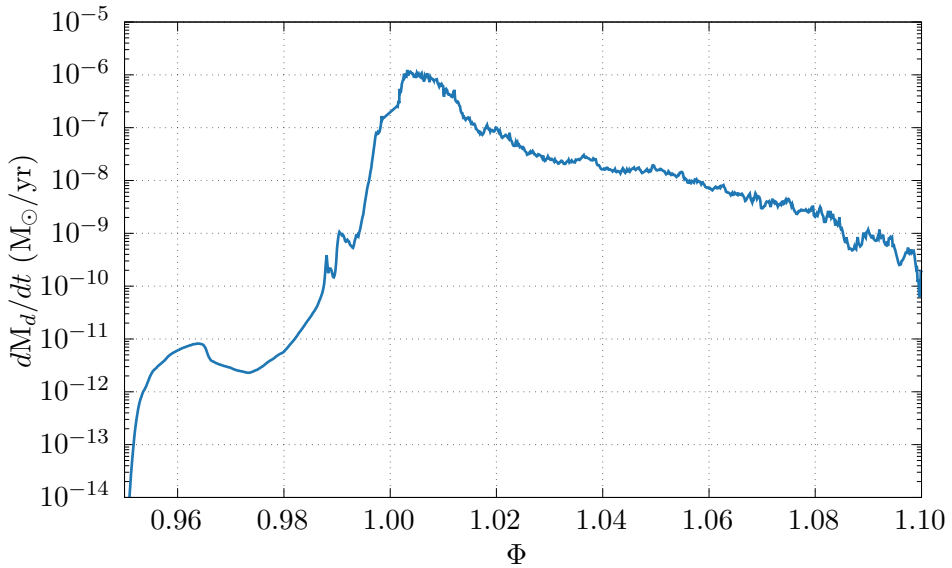


Figure 5.3: A graph of the dust production rate in the WCR over the orbital phase $0.95 \leq \Phi \leq 1.10$. The dust production rate sharply increases as the stars pass their closest approach. Afterwards, the dust production rate begins to falter and slow, due to weaker wind collision effects via the separation distance and radial velocity.

$$\rho_{\text{SW}} = \frac{\dot{M}_{\text{SW}}}{4\pi r^2 v_{\text{SW}}^\infty}, \quad (5.23)$$

where r is the distance from the barycentre. This threshold value was set to $\rho_{\text{thres}} = 1.25\rho_{\text{SW}}$, which was found to accurately identify the WCR through thorough prior testing.

5.4 Results and Conclusions

Dust production was found to be consistent with previous uses of this particular dust model. Dust production rates were found to be sensible, and significantly below the theoretical maximum dust formation rate, $\dot{M}_{d,\text{max}} \approx 4.8 \times 10^{-6} M_\odot \text{ yr}^{-1}$. After an initial advection period lasting until $\Phi \approx 0.96$, the dust production rate rapidly increased as the stars approached periastron passage, peaking at $\Phi \sim 1.01$ (Fig. 5.3). This maximum dust production rate of $1.24 \times 10^{-6} M_\odot \text{ yr}^{-1}$

5.4 Results and Conclusions

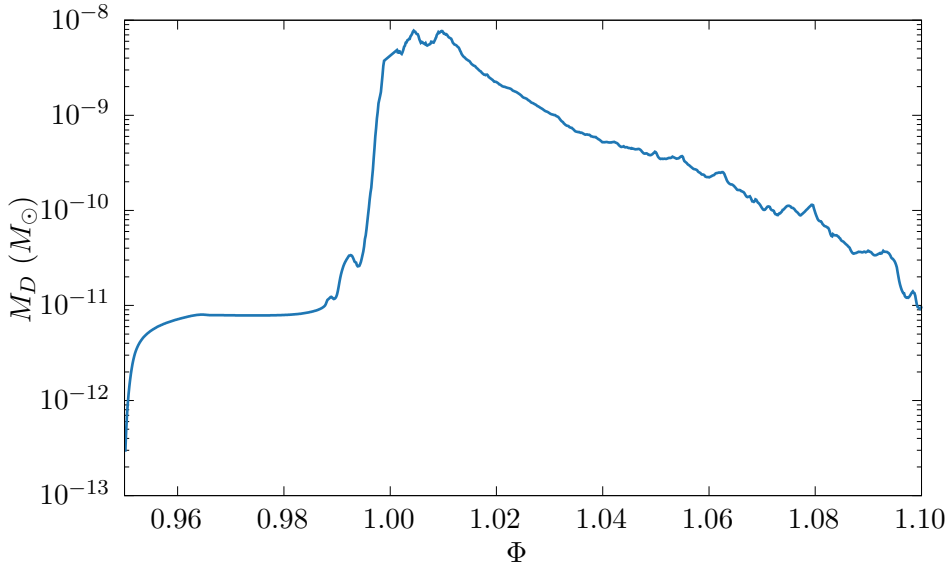


Figure 5.4: A graph of the overall dust mass in the simulation of WR140 over the orbital phase $0.95 \leq \Phi \leq 1.10$. The amount of dust quickly reduces after periastron due to a decreased dust formation rate (Fig. 5.3), as well as dust advecting off of the numerical grid.

is sensible, but incredibly prodigious, demonstrating a peak conversion efficiency of gas into dust of $\sim 26\%$ in the WCR and a total conversion efficiency of $\sim 2.2\%$ throughout the entire system. After reaching this maximum value, the dust production rate steadily decreases as the stars recede from each other. This is reflected in the overall dust mass of the simulation (Fig. 5.4), as well as in infrared observations of WR140, where the infrared emission from dust formation rapidly reaches a maximum value after periastron passage, and slowly relaxes to a minimum value. This asymmetry in the time-dependent change in infrared luminosity implies the existence of several factors for suppression and encouragement of dust formation than just the change in orbital separation distance. It should be noted that due to the small size of the simulation, the dust mass in the system will reduce quickly, as dust advects off of the numerical grid.

The evolution of dust in this system would result in the formation of an expanding cloud of dust every time the system passes periastron, with no contiguous spiral pattern forming, due to the lengthy “dormant” period occurring shortly after periastron passage. This is consistent with observations of WR140, where these disconnected clouds are observed (P. M. Williams et al., 2009). We find an average dust production rate of $\dot{M}_d = 7.68 \times 10^{-8} M_\odot \text{ yr}^{-1}$, and a change in the dust production rate by approximately five orders of magnitude over the course of

5. EXPLORING DUST FORMATION IN WR140

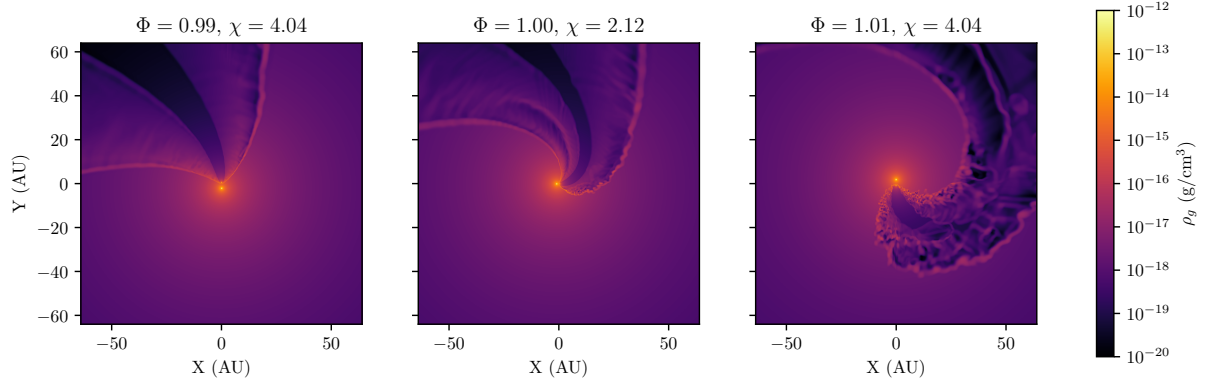


Figure 5.5: Gas density in a simulation of the WR140 system shortly before, during, and shortly after periastron. The simulation becomes rapidly dominated by instabilities a short while after periastron. However, these instabilities persist despite the system behaving adiabatically at a similar orbital separation distance prior to periastron. This suggests that the radiative behaviour of the post-shock WCR is due to multiple factors, other than dust at varying d_{sep} .

the simulation. This fits our understanding of an episodic dust forming WCd system, with an extremely clear “active” period followed by a slow tapering off of dust production as the system approaches the “dormant” period. We can compare our results to the estimated dust yields from Lau et al. (2020), which found an average dust production rate of $\dot{M}_d = 8.11 \times 10^{-10} M_\odot \text{ yr}^{-1}$. Our value for the dust-to-gas mass ratio within the system appears to be sensible, while our average dust production rate is significantly higher. This is due to the limited temporal sample of the simulation. We would find a significantly lower average dust production rate over the course of a full orbit due to more sampling of the system over the “dormant” period.

5.4.1 Instabilities

As can be seen in Fig. 5.5, after periastron passage the post-shock WCR region transitions from a smooth adiabatic wind to a highly radiative wind dominated by instabilities. As the WCR becomes increasingly dominated by instabilities, dust formation drastically increases, with the bulk of dust formation occurring within the high density regions produced by these instabilities. These clumpy pockets of gas do not exhibit significant dust formation beyond ~ 20 AU from the simulation barycentre, with concentrations of dust remaining approximately constant (Fig. 5.6). By the end of the simulation at $\Phi = 1.10$, the WCR is still somewhat dominated by instabilities, with an elevated dust production rate even though the cooling parameter has increased significantly to $\chi = 19.7$, which would imply adiabatic behaviour. Whilst the dust

5.4 Results and Conclusions

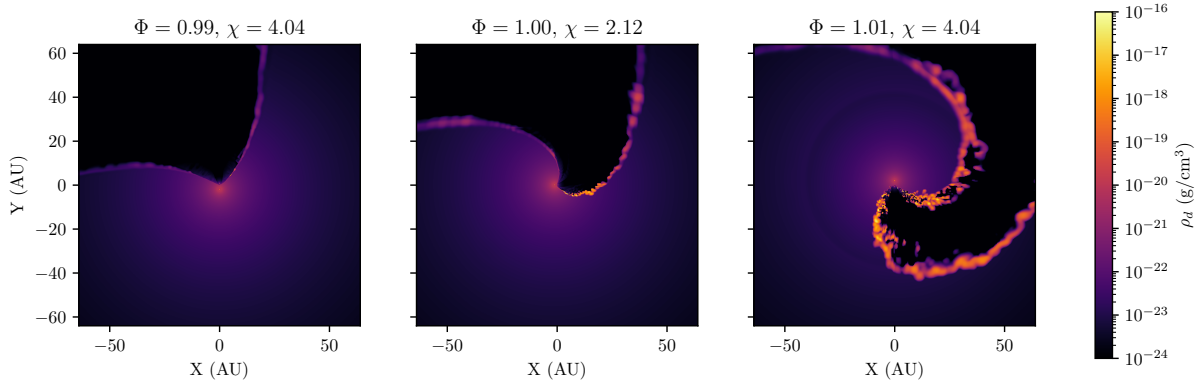


Figure 5.6: Dust density in a simulation of the WR140 system shortly before, during, and shortly after periastron. Dust formation occurs as a direct result of the formation of thermal and KH instabilities in the post-shock WCR.

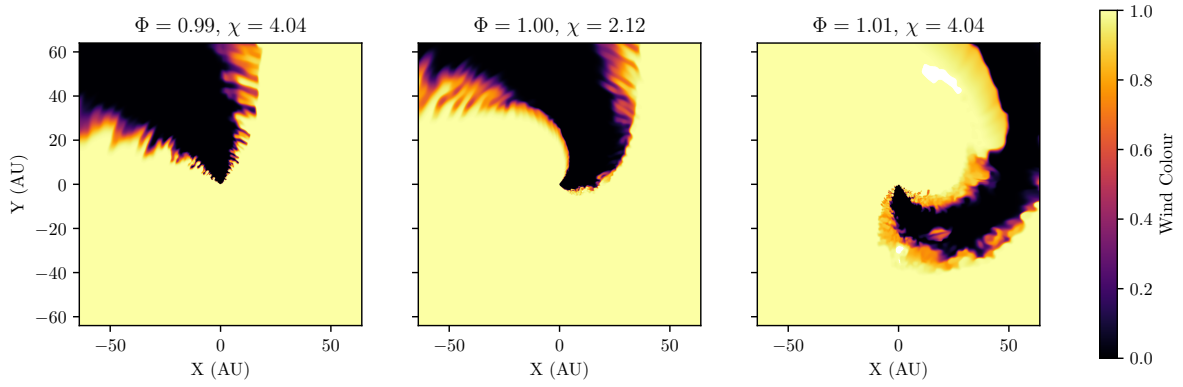


Figure 5.7: Wind “colour” in a simulation of the WR140 system shortly before, during, and shortly after periastron. With 1 representing a pure WR wind and 0 representing a pure OB wind. We find that the wind undergoes more mixing during and after periastron.

5. EXPLORING DUST FORMATION IN WR140

formation rate has reduced significantly, there is still a significantly greater formation rate than at the start of the simulation (after advection). This suggests that the transition from radiative to adiabatic behaviour has a degree of latency, with instabilities still driving the structure of the WCR long after adiabatic flow should have been re-established. The amount of wind being mixed in the system is also significantly increased after periastron passage, which would be conducive to the formation of complex organic molecules on the surface of the dust grains (Fig. 5.7). Whilst research into this is out of the scope of the project, evolution of dust grains from WCd systems on longer time and length scales would be an enlightening avenue of research.

5.4.2 Influence of varying wind velocity on dust production

As we have previously discussed, varying the wind terminal velocity for both stars in a simulation can result in exponential changes in the dust production rate. This is theorised to be due to the increased influence of thermal instabilities through increased cooling in slower post-shock winds, as well as through KH instabilities driven through a wind velocity shear (if the wind terminal velocities are significantly different, see Stevens et al., 1992). Previous work on this subject considered systems with circular orbits, hence the orbital motion between the stars was persistent, and did not contribute to a change in the wind velocities over the orbit of the system. However, in the case of a system with an eccentric orbit (such as WR140), we would find that both the outflow velocity for each wind - as well as the velocity ratio - would be markedly different over the systems orbit. As the stars approach periastron, the radial velocity, v_r for each star rapidly changes from a minimum value to a maximum, as the stars approach and then swing past one another. This sudden change in the stars radial velocity results in a rapid change in the velocity for both winds entering the collision region. This will influence the amount of radiative cooling in the post-shock wind, suppressing radiative cooling pre-periastron and inciting it post-periastron, altering the dust formation rates. While this change in wind velocity is relatively small, with the wind velocity varying by as much as 6% over the course of an orbit, this can still impact the cooling of the system. Due to χ being dependent on v^4 , this effect can vary χ by as much as a factor of 1.26 in the case of WR140.

The rate of dust formation is also strongly governed by the presence of a large wind velocity ratio, Υ , where:

$$\Upsilon = v_{\text{OB}}/v_{\text{WR}}, \quad (5.24)$$

As the mass of each star is different, the change in velocity differs, causing an increased velocity ratio and therefore a stronger velocity shear. Previous research with dust models suggests that a strong velocity shear drives an increased dust formation rate. We find that the maximum change in velocity shear occurs at $\Phi = 1.01$, around the same time where the dust formation rate is at a maximum; this is consistent with our previous work (Fig. 5.8). Whilst this change in velocity shear would not significantly alter the dynamics of dust formation on its own, it may be another factor in explaining the increased dust formation of WR140 post-periastron, and explain why the system is still dominated by instabilities even after the system should be behaving adiabatically. However, this effect may also be decreased somewhat by the effect of radiative inhibition and braking on the winds. We find using a model estimating wind velocities using the Castor et al. (1975) model for radiative driving that the OB wind in particular is affected. Fig. 5.9 shows the wind velocities resultant from this model with CAK parameters for the WR and OB stars in WR140. We find that the wind velocity is approximately 84% of the expected velocity. This would decrease the velocity shear before and after periastron passage. The effect of radiative line driving from the CAK model is not considered in this simulation, and simulations considering this effect would have to be performed in order to study this further. This represents another interesting avenue of future research.

5.5 Summary

Despite only simulating a limited section of the orbit of WR140, we have made a number of insights into the behaviour of the system. We find a significant degree of change in the dust formation rate as a direct consequence of the changing orbital separation of the system. This is related to the change in the behaviour of the post-shock WCR wind, which goes from a smooth adiabatic wind to a clumpy, high density wind dominated by instabilities ideal for dust formation. It is particularly interesting to note that the system does not revert to behaving adiabatically as quickly as it entered it. This suggests that the post-shock WCR condition of the system is dependent on additional factors, instead of being solely due to d_{sep} . One of the main factors on this delayed return to the adiabatic, “dormant” state is potentially due to the orbital motion of the stars themselves. As the stars approach each other at periastron, the radial velocity of the stars adds velocity to the wind beyond the outflow velocity, resulting in higher wind collision velocities, which encourages adiabatic behaviour in the post-shock flow. The inverse is true as the stars recede from one another, the effective wind velocity for both

5. EXPLORING DUST FORMATION IN WR140

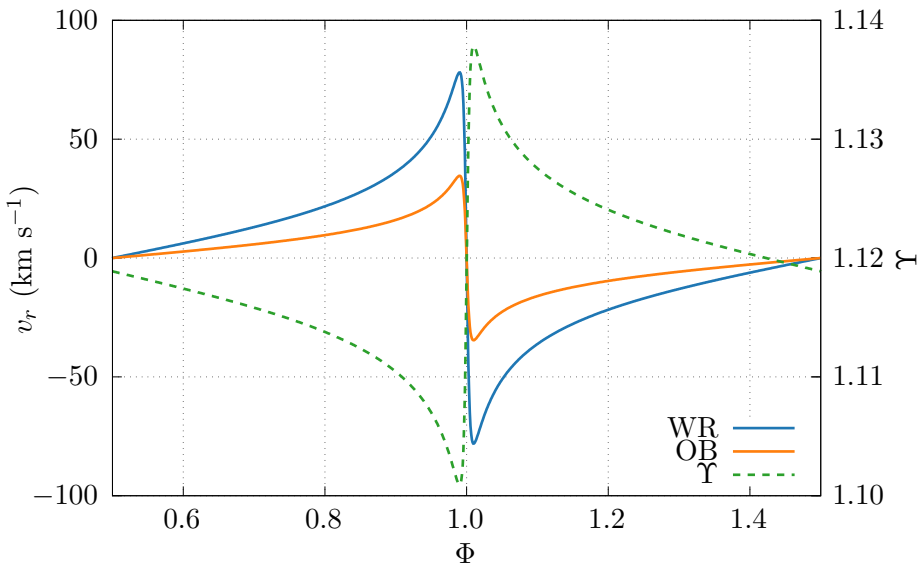


Figure 5.8: Radial velocity as a function of the orbital phase for the WR and OB stars in the WR140 system relative to the barycentre. As periastron passage occurs, the sudden inversion from approaching to receding can alter the wind velocity of the WR star by as much as 160 km s^{-1} . Whilst this discrepancy is $\sim 6\%$ of the WR wind velocity, this can significantly increase dust production if the stars are receding from each other. The velocity shear, $v_{\text{OB}}/v_{\text{WR}}$, also sharply increases during periastron passage, peaking at the point of maximum dust formation.

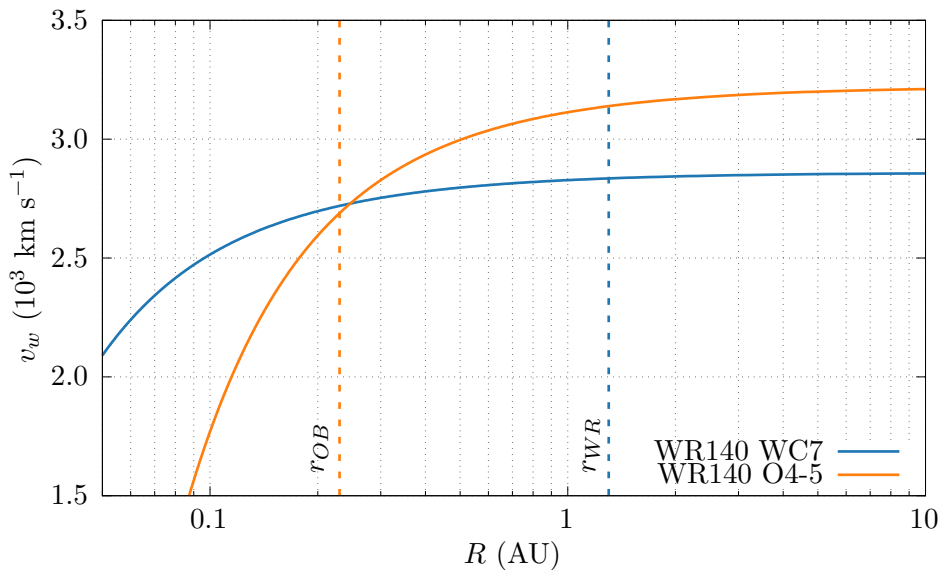


Figure 5.9: Graph of the wind velocity of the WC7 and O4-5 stars in the WR140 system as a function of distance from the stellar surface due to radiative line driving. The dashed lines represent the distance to the WCR at periastron for each star. During periastron passage the WC7 wind is travelling at approximately its terminal velocity before collision, while the O4-5 companions wind is travelling at $\sim 84\%$ of terminal velocity before coming into contact with the WCR. CAK parameters were estimated to be $k = 0.37$, $\alpha = 0.60$ for the O4-5 star and $k = 0.48$, $\alpha = 0.57$ for the WC7 star.

5. EXPLORING DUST FORMATION IN WR140

stars is reduced, which encourages the formation of thermal instabilities. Furthermore, as the OB star dominates the orbital dynamics of the system, the effective WR wind velocity is even further reduced, leading to an increased wind velocity ratio, resulting in a velocity shear that can drive KH instabilities.

There is much additional research potential in simulating dust growth in episodic WCd systems. Further simulations of this system in particular would involve simulating a full orbit, through the use of AMR and increased computing time. Other avenues of research include the effect on dust formation due to the influence of radiative line driving and sudden braking, as well as a more complex, multi-fluid dust model where dust grains are not explicitly coupled to the stellar wind.

5.6 Acknowledgements

This work was undertaken on ARC4, part of the High Performance Computing facilities at the University of Leeds, UK. We would also like to thank P. A. Crowther for his work on the [Galactic Wolf-Rayet Catalogue¹](#).

¹pacrowther.staff.shef.ac.uk/WRcat

CHAPTER 6

Final Notes and Conclusions

6. FINAL NOTES AND CONCLUSIONS

6.1 Conclusions

6.1.1 Causes of dust formation in WCd systems

6.1.2 The role of eccentricity in dust formation

6.2 Future Study

6.2.1 More complex models

6.2.2 Further simulations of observed systems

6.2.3 Radiative transfer

6.2.4 WR+WR systems

6.2.5 Next generation telescopes

6.3 Other Observations

6.3.1 *Doctorate Strangelove or: How I Learned to Stop Worrying and Love Numerics*

6.3.2 Join the physics department, see the world

6.3.3 Paul Erdős was probably onto something

6.3.4 Carinae Strain: PhD research in a time of pandemic

6.3.5 WR 104 as a local GRB candidate

6.4 Research software acknowledgements

This work was undertaken on ARC4 and ARC3, part of the High Performance Computing facilities at the University of Leeds, UK.

A good deal of the data reduction of this thesis was conducted using the Python 3 program-

6.4 Research software acknowledgements

ming language (Van Rossum & Drake, 2009), in particular, the following open source modules were used extensively:

- [NumPy¹](#) (Harris et al., 2020)
- [Astropy²](#) (Astropy Collaboration et al., 2018; Astropy Collaboration et al., 2013)
- [Matplotlib³](#) (Hunter, 2007)

[Athena++](#) (Stone et al., 2021) was also used extensively throughout the work in this thesis.

GNU Parallel (Tange, 2021) was used to speed up the batch processing of data within this project, if parallel programming is difficult, sometimes the only option is to run many, *many* serial programmes at once. Finally, this thesis was typeset with L^AT_EX, using the T_EXlive distribution and `latexmk` for compilation. It is abundantly clear that scientists the world over owe an enormous debt of gratitude to Donald Knuth and Leslie Lamport for their work on the T_EX and L^AT_EX projects. Let's hope that the version π update isn't coming too soon.

¹<https://numpy.org/>

²<https://www.astropy.org/>

³<https://matplotlib.org/>

6. FINAL NOTES AND CONCLUSIONS

APPENDIX A

Astrophysical Shocks

A. ASTROPHYSICAL SHOCKS

APPENDIX B

Software Carpentry

B. SOFTWARE CARPENTRY

B.1 Amdahl's Law

B.2 Version Control

BIBLIOGRAPHY

Book Citations

- Apai, D. & Lauretta, D. S. (Eds.). (2010). *Protoplanetary Dust: Astrophysical and Cosmochemical Perspectives*. Cambridge University Press.
DOI: [10.1017/CBO9780511674662](https://doi.org/10.1017/CBO9780511674662). (Cit. p. 22)
- Bodenheimer, P. H. (2011, January 1). *Principles of Star Formation*.
DOI: [10.1007/978-3-642-15063-0](https://doi.org/10.1007/978-3-642-15063-0). (Cit. p. 5, 6)
- Carroll, B. W. & Ostlie, D. A. (2014). *An Introduction to Modern Astrophysics* (Second international). Pearson. (Cit. p. 4).
- Cherchneff, I. (2015, January 1). *Dust formation in carbon-rich Wolf-Rayet colliding winds*. (Cit. p. 79).
- Dyson, J. E. (2021). *The physics of the interstellar medium* (Third edition.). CRC Press. (Cit. p. 27, 28).
- Lamers, H. J. & Cassinelli, J. P. (1999). *Introduction to stellar winds*. Cambridge University Press. (Cit. p. 8, 10, 11, 120).
- Maciel, W. J. (2014). *Hydrodynamics and Stellar Winds: An Introduction*. Springer International Publishing. (Cit. p. 12).
- Oswalt, T. D. & Barstow, M. A. (Eds.). (2013). *Planets, Stars and Stellar Systems*. Springer Netherlands.
DOI: [10.1007/978-94-007-5615-1](https://doi.org/10.1007/978-94-007-5615-1). (Cit. p. 15)
- Ryan, S. G. & Norton, A. J. (2010). *Stellar evolution and nucleosynthesis*. Cambridge University Press. (Cit. p. 14).
- Rybicki, G. B. & Lightman, A. P. (2004). *Radiative processes in astrophysics*. Wiley. (Cit. p. 29).
- Salaris, M. & Cassisi, S. (2005). *Evolution of Stars and Stellar Populations*. (Cit. p. 7).

BIBLIOGRAPHY

- Spitzer, L. (2008, November 20). *Physical Processes in the Interstellar Medium*. John Wiley & Sons. (Cit. p. 17, 19, 88, 115).
- Vink, J. S. (Ed.). (2015). *Very Massive Stars in the Local Universe* (Vol. 412). Springer International Publishing.
- DOI: [10.1007/978-3-319-09596-7](https://doi.org/10.1007/978-3-319-09596-7). (Cit. p. 15)
- Ward-Thompson, D. & Whitworth, A. P. (2011). *An Introduction to Star Formation*. Cambridge University Press.
- DOI: [10.1017/CBO9780511974021](https://doi.org/10.1017/CBO9780511974021). (Cit. p. 5, 6, 14, 21)
- Whittet, D. C. B. (2002, October 21). *Dust in the Galactic Environment*. CRC Press.
- DOI: [10.1201/9781482268645](https://doi.org/10.1201/9781482268645). (Cit. p. 17, 20)
- Williams, D. A. & Cecchi-Pestellini, C. (2015, November 18). *The Chemistry of Cosmic Dust*.
- DOI: [10.1039/C5TA03694A](https://doi.org/10.1039/C5TA03694A). (Cit. p. 21)
- Wong, S. S. M. (1998, August 1). *Introductory Nuclear Physics, 2nd Edition*. (Cit. p. 7).

Journal Citations

- Abbott, D. C. (1982). The theory of radiatively driven stellar winds. II. The line acceleration. *The Astrophysical Journal*, 259, 282–301.
- DOI: [10.1086/160166](https://doi.org/10.1086/160166) (cit. p. 12)
- Allen, D. A., Swings, J. P. & Harvey, P. M. (1972). Infrared photometry of northern Wolf-Rayet stars. *Astronomy and Astrophysics*, 20, 333–336 (cit. p. 78).
- Beals, C. S. (1929). On the nature of Wolf-Rayet emission. *Monthly Notices of the Royal Astronomical Society*, 90, 202–212.
- DOI: [10.1093/mnras/90.2.202](https://doi.org/10.1093/mnras/90.2.202) (cit. p. 8)
- Berger, M. J. & Colella, P. (1989). Local adaptive mesh refinement for shock hydrodynamics. *Journal of Computational Physics*, 82(1), 64–84.
- DOI: [10.1016/0021-9991\(89\)90035-1](https://doi.org/10.1016/0021-9991(89)90035-1) (cit. p. 52)
- Berger, M. J. & Oliger, J. (1984). Adaptive mesh refinement for hyperbolic partial differential equations. *Journal of Computational Physics*, 53(3), 484–512.
- DOI: [10.1016/0021-9991\(84\)90073-1](https://doi.org/10.1016/0021-9991(84)90073-1) (cit. p. 52)
- Bethe, H. A. (1939). Energy Production in Stars. *Phys. Rev.*, 55(5), 434–456.
- DOI: [10.1103/PhysRev.55.434](https://doi.org/10.1103/PhysRev.55.434) (cit. p. 6, 7)

JOURNAL CITATIONS

- Birnstiel, T., Fang, M. & Johansen, A. (2016). Dust Evolution and the Formation of Planetesimals. *Space Sci Rev*, 205(1), 41–75.
DOI: [10.1007/s11214-016-0256-1](https://doi.org/10.1007/s11214-016-0256-1) (cit. p. 22)
- Callingham, J. R., Crowther, P. A., Williams, P. M., Tuthill, P. G., Han, Y., Pope, B. J. S. & Marcote, B. (2020). Two Wolf-Rayet stars at the heart of colliding-wind binary Apep. *Mon Not R Astron Soc*, 495(3), 3323–3331.
DOI: [10.1093/mnras/staa1244](https://doi.org/10.1093/mnras/staa1244) (cit. p. 40)
- Callingham, J. R., Tuthill, P. G., Pope, B. J. S., Williams, P. M., Crowther, P. A., Edwards, M., Norris, B. & Kedziora-Chudczer, L. (2019). Anisotropic winds in a Wolf-Rayet binary identify a potential gamma-ray burst progenitor. *Nature Astronomy*, 3(1), 82–87.
DOI: [10.1038/s41550-018-0617-7](https://doi.org/10.1038/s41550-018-0617-7) (cit. p. 40, 41, 47, 116)
- Cassinelli, J. P. (1979). Stellar Winds. *Annual Review of Astronomy and Astrophysics*, 17(1), 275–308.
DOI: [10.1146/annurev.aa.17.090179.001423](https://doi.org/10.1146/annurev.aa.17.090179.001423) (cit. p. 10)
- Castor, J. I., Abbott, D. C. & Klein, R. I. (1975). Radiation-driven winds in Of stars. *The Astrophysical Journal*, 195, 157.
DOI: [10.1086/153315](https://doi.org/10.1086/153315) (cit. p. xvii, 12, 129)
- Cherepashchuk, A. M. (1976). Detectability of Wolf-Rayet binaries from X-rays. *Soviet Astronomy Letters*, 2, 138 (cit. p. 22).
- Chini, R., Hoffmeister, V. H., Nasser, A., Stahl, O. & Zinnecker, H. (2012). A spectroscopic survey on the multiplicity of high-mass stars. *Monthly Notices of the Royal Astronomical Society*, 424, 1925–1929.
DOI: [10.1111/j.1365-2966.2012.21317.x](https://doi.org/10.1111/j.1365-2966.2012.21317.x) (cit. p. 6)
- Chokshi, A., Tielens, A. G. G. M. & Hollenbach, D. (1993). Dust Coagulation. *The Astrophysical Journal*, 407, 806.
DOI: [10.1086/172562](https://doi.org/10.1086/172562) (cit. p. 17)
- Colella, P. & Woodward, P. R. (1984). The piecewise parabolic method (PPM) for gas-dynamical simulations. *Journal of computational physics*, 54(1), 174–201 (cit. p. 46).
- Crowther, P. A. (2003). Dust Formation around Wolf-Rayet Stars. *Astrophysics and Space Science*, 285(3), 677–685.
DOI: [10.1023/A:1026157126395](https://doi.org/10.1023/A:1026157126395) (cit. p. 35, 79, 121)

BIBLIOGRAPHY

- Crowther, P. A. (2007). Physical Properties of Wolf-Rayet Stars. *Annual Review of Astronomy and Astrophysics*, 45(1), 177–219.
DOI: [10.1146/annurev.astro.45.051806.110615](https://doi.org/10.1146/annurev.astro.45.051806.110615) (cit. p. 14, 15)
- Danks, A. C., Dennefeld, M., Wamsteker, W. & Shaver, P. A. (1983). Near infrared spectroscopy and infrared photometry of a new WC9 star. *Astronomy and Astrophysics*, 118, 301–305 (cit. p. 40).
- del Palacio, S., Benaglia, P., De Becker, M., Bosch-Ramon, V. & Romero, G. E. (2021). The non-thermal emission from the colliding-wind binary Apep. *arXiv e-prints* (cit. p. 41).
- Draine, B. T. & Salpeter, E. E. (1979a). Destruction mechanisms for interstellar dust. *The Astrophysical Journal*, 231, 438–455.
DOI: [10.1086/157206](https://doi.org/10.1086/157206) (cit. p. 20, 33)
- Draine, B. T. & Salpeter, E. E. (1979b). On the physics of dust grains in hot gas. *The Astrophysical Journal*, 231, 77–94.
DOI: [10.1086/157165](https://doi.org/10.1086/157165) (cit. p. 18, 89, 116)
- Draine, B. (2003). Interstellar Dust Grains. *Annual Review of Astronomy and Astrophysics*, 41(1), 241–289.
DOI: [10.1146/annurev.astro.41.011802.094840](https://doi.org/10.1146/annurev.astro.41.011802.094840) (cit. p. 20)
- Dwek, E. & Werner, M. W. (1981). The Infrared Emission From Supernova Condensates. *The Astrophysical Journal*, 248, 138.
DOI: [10.1086/159138](https://doi.org/10.1086/159138) (cit. p. 31, 32, 62–64, 85, 86, 116)
- Dwek, E., Foster, S. M. & Vancura, O. (1996). Cooling, Sputtering, and Infrared Emission from Dust Grains in Fast Nonradiative Shocks. *The Astrophysical Journal*, 457, 244.
DOI: [10.1086/176725](https://doi.org/10.1086/176725) (cit. p. 18, 20, 71, 89, 116)
- Eddington, A. S. (1920). The Internal Constitution of the Stars. *The Scientific Monthly*, 11(4), 297–303 (cit. p. 6).
- Eichler, D. & Usov, V. (1993). Particle acceleration and nonthermal radio emission in binaries of early-type stars. *The Astrophysical Journal*, 402, 271–279.
DOI: [10.1086/172130](https://doi.org/10.1086/172130) (cit. p. 23, 24, 27, 81, 119)
- Friend, D. B. & Abbott, D. C. (1986). The theory of radiatively driven stellar winds. III - Wind models with finite disk correction and rotation. *The Astrophysical Journal*, 311, 701.
DOI: [10.1086/164809](https://doi.org/10.1086/164809) (cit. p. 13)

JOURNAL CITATIONS

- Gayley, K. G., Owocki, S. P. & Cranmer, S. R. (1997). Sudden Radiative Braking in Colliding Hot-Star Winds. *ApJ*, 475(2), 786.
DOI: [10.1086/303573](https://doi.org/10.1086/303573) (cit. p. 39, 56, 80, 119)
- Godunov, S. K. (1959). A difference scheme for numerical solution of discontinuous solution of hydrodynamic equations. *Math. Sbornik*, 47, 271–306 (cit. p. 45).
- Grimaldo, E., Reimer, A., Kissmann, R., Niederwanger, F. & Reitberger, K. (2019). Proton Acceleration in Colliding Stellar Wind Binaries. *The Astrophysical Journal*, 871, 55.
DOI: [10.3847/1538-4357/aaf6ee](https://doi.org/10.3847/1538-4357/aaf6ee) (cit. p. 23)
- Han, Y., Tuthill, P. G., Lau, R. M., Soulain, A., Callingham, J. R., Williams, P. M., Crowther, P. A., Pope, B. J. S. & Marcote, B. (2020). The extreme colliding-wind system Apep: Resolved imagery of the central binary and dust plume in the infrared. *Monthly Notices of the Royal Astronomical Society*, 498(4), 5604–5619.
DOI: [10.1093/mnras/staa2349](https://doi.org/10.1093/mnras/staa2349) (cit. p. 41, 42)
- Harries, T. J., Monnier, J. D., Symington, N. H. & Kurosawa, R. (2004a). Three-dimensional dust radiative-transfer models: The Pinwheel Nebula of WR 104. *Monthly Notices of the Royal Astronomical Society*, 350(2), 565–574.
DOI: [10.1111/j.1365-2966.2004.07668.x](https://doi.org/10.1111/j.1365-2966.2004.07668.x) (cit. p. 38)
- Harries, T. J., Monnier, J. D., Symington, N. H. & Kurosawa, R. (2004b). Three-dimensional dust radiative-transfer models: The Pinwheel Nebula of WR 104. *Monthly Notices of the Royal Astronomical Society*, 350(2), 565–574.
DOI: [10.1111/j.1365-2966.2004.07668.x](https://doi.org/10.1111/j.1365-2966.2004.07668.x) (cit. p. 90, 96)
- Hendrix, T., Keppens, R., van Marle, A. J., Camps, P., Baes, M. & Meliani, Z. (2016). Pinwheels in the sky, with dust: 3D modelling of the Wolf-Rayet 98a environment. *Monthly Notices of the Royal Astronomical Society*, 460(4), 3975–3991.
DOI: [10.1093/mnras/stw1289](https://doi.org/10.1093/mnras/stw1289) (cit. p. 37, 72, 74, 75, 87, 96, 97, 112)
- Herbst, E. & van Dishoeck, E. F. (2009). Complex Organic Interstellar Molecules. *Annual Review of Astronomy and Astrophysics*, 47(1), 427–480.
DOI: [10.1146/annurev-astro-082708-101654](https://doi.org/10.1146/annurev-astro-082708-101654) (cit. p. 20, 21, 107)
- Ishihara, D., Kaneda, H., Onaka, T., Ita, Y., Matsuura, M. & Matsunaga, N. (2011). Galactic distributions of carbon- and oxygen-rich AGB stars revealed by the AKARI mid-infrared all-sky survey. *A&A*, 534, A79.
DOI: [10.1051/0004-6361/201117626](https://doi.org/10.1051/0004-6361/201117626) (cit. p. 34, 79)
- Jones, A. P. (2004). Dust Destruction Processes. 309, 347 (cit. p. 17, 19).

BIBLIOGRAPHY

- Jones, A. P., Tielens, A. G. G. M. & Hollenbach, D. J. (1996). Grain Shattering in Shocks: The Interstellar Grain Size Distribution. *The Astrophysical Journal*, *469*, 740.
DOI: [10.1086/177823](https://doi.org/10.1086/177823) (cit. p. 17)
- Kapteyn, J. C. (1909). On the Absorption of Light in Space. *The Astrophysical Journal*, *29*, 46.
DOI: [10.1086/141618](https://doi.org/10.1086/141618) (cit. p. 16)
- Lamberts, A., Dubus, G., Fromang, S. & Lesur, G. (2012). Colliding wind binaries and γ -ray binaries: Relativistic version of the RAMSES code, 406–409.
DOI: [10.1063/1.4772283](https://doi.org/10.1063/1.4772283) (cit. p. 38)
- Lau, R. M., Eldridge, J. J., Hankins, M. J., Lamberts, A., Sakon, I. & Williams, P. M. (2020). Revisiting the Impact of Dust Production from Carbon-rich Wolf-Rayet Binaries. *ApJ*, *898*(1), 74.
DOI: [10.3847/1538-4357/ab9cb5](https://doi.org/10.3847/1538-4357/ab9cb5) (cit. p. 37, 39, 42, 79, 110, 126)
- Lucy, L. B. & Solomon, P. M. (1970). Mass Loss by Hot Stars. *The Astrophysical Journal*, *159*, 879.
DOI: [10.1086/150365](https://doi.org/10.1086/150365) (cit. p. 11, 12)
- Marchenko, S. V., Moffat, A. F. J. & Crowther, P. A. (2010). Population I Wolf-Rayet Runaway Stars: The Case of WR124 and its Expanding Nebula M1-67. *The Astrophysical Journal*, *724*, L90–L94.
DOI: [10.1088/2041-8205/724/1/L90](https://doi.org/10.1088/2041-8205/724/1/L90) (cit. p. 15)
- Marcote, B., Callingham, J. R., De Becker, M., Edwards, P. G., Han, Y., Schulz, R., Stevens, J. & Tuthill, P. G. (2021). AU-scale radio imaging of the wind collision region in the brightest and most luminous non-thermal colliding wind binary Apep. *Monthly Notices of the Royal Astronomical Society*, *501*(2), 2478–2486.
DOI: [10.1093/mnras/staa3863](https://doi.org/10.1093/mnras/staa3863) (cit. p. 41)
- Medina, E. M., Richardson, N. & Chené, A. (2021). Are all WCd stars binaries? An IGRINS search for companion stars. *53*, 215.07 (cit. p. 33).
- Meyer, C. D., Balsara, D. S. & Aslam, T. D. (2014). A stabilized Runge-Kutta-Legendre method for explicit super-time-stepping of parabolic and mixed equations. *Journal of Computational Physics*, *257*, 594–626.
DOI: [10.1016/j.jcp.2013.08.021](https://doi.org/10.1016/j.jcp.2013.08.021) (cit. p. 50)
- Milne, E. A. (1926). On the possibility of the emission of high-speed atoms from the sun and stars. *Monthly Notices of the Royal Astronomical Society*, *86*, 459–473.
DOI: [10.1093/mnras/86.7.459](https://doi.org/10.1093/mnras/86.7.459) (cit. p. 12)

JOURNAL CITATIONS

- Monnier, J. D., Tuthill, P. G. & Danchi, W. C. (1999). Pinwheel Nebula around WR 98a. *ApJ*, 525(2), L97.
DOI: [10.1086/312352](https://doi.org/10.1086/312352) (cit. p. 37, 79, 110)
- Monnier, J. D., Tuthill, P. G., Danchi, W. C., Murphy, N. & Harries, T. J. (2007). The Keck Aperture-masking Experiment: Near-Infrared Sizes of Dusty Wolf-Rayet Stars. *ApJ*, 655(2), 1033.
DOI: [10.1086/509873](https://doi.org/10.1086/509873) (cit. p. 36, 116)
- Neugent, K. & Massey, P. (2019). The Wolf-Rayet Content of the Galaxies of the Local Group and Beyond. *Galaxies*, 7(3), 74.
DOI: [10.3390/galaxies7030074](https://doi.org/10.3390/galaxies7030074) (cit. p. 15)
- Niedzielski, A. & Skorzynski, W. (2002). Kinematical Structure of Wolf-Rayet Winds. I. Terminal Wind Velocity. *Acta Astronomica*, 52, 81–104 (cit. p. 34).
- Pauldrach, A., Puls, J. & Kudritzki, R. P. (1986). Radiation-driven winds of hot luminous stars. Improvements of the theory and first results. *Astronomy and Astrophysics*, Vol. 164, p. 86-100 (1986), 164, 86 (cit. p. 13).
- Pittard, J. M. (2009). 3D models of radiatively driven colliding winds in massive O+O star binaries - I. Hydrodynamics. *Monthly Notices of the Royal Astronomical Society*, 396(3), 1743–1763.
DOI: [10.1111/j.1365-2966.2009.14857.x](https://doi.org/10.1111/j.1365-2966.2009.14857.x) (cit. p. 96)
- Pittard, J. M. & Dawson, B. (2018). Colliding stellar winds structure and X-ray emission. *Mon Not R Astron Soc*, 477(4), 5640–5645.
DOI: [10.1093/mnras/sty1025](https://doi.org/10.1093/mnras/sty1025) (cit. p. 26, 81, 90, 119)
- Pollock, A. M. T. (1987). The Einstein View of the Wolf-Rayet Stars. *The Astrophysical Journal*, 320, 283.
DOI: [10.1086/165539](https://doi.org/10.1086/165539) (cit. p. 23)
- Prilutskii, O. F. & Usov, V. V. (1976). X rays from Wolf-Rayet binaries. *Soviet Astronomy*, 20, 2 (cit. p. 22, 23, 110).
- Rosslowe, C. K. & Crowther, P. A. (2015). Spatial distribution of Galactic Wolf-Rayet stars and implications for the global population. *Monthly Notices of the Royal Astronomical Society*, 447(3), 2322–2347.
DOI: [10.1093/mnras/stu2525](https://doi.org/10.1093/mnras/stu2525) (cit. p. 33, 34, 78–80, 111)

BIBLIOGRAPHY

- Ruuth, S. J. & Spiteri, R. J. (2005). High-Order Strong-Stability-Preserving Runge-Kutta Methods with Downwind-Biased Spatial Discretizations. *SIAM Journal on Numerical Analysis*, 42(3), 974–996 (cit. p. 50, 121).
- Saha, M. N. (1919). On Radiation-Pressure and the Quantum Theory. *The Astrophysical Journal*, 50, 220.
DOI: [10.1086/142497](https://doi.org/10.1086/142497) (cit. p. 12)
- Salpeter, E. E. (1977). Formation and Destruction of Dust Grains. *Annual Review of Astronomy and Astrophysics*, 15(1), 267–293 (cit. p. 33).
- Schure, K. M., Kosenko, D., Kaastra, J. S., Keppens, R. & Vink, J. (2009). A New Radiative Cooling Curve Based on an Up-To-Date Plasma Emission Code. *A&A*, 508(2), 751–757.
DOI: [10.1051/0004-6361/200912495](https://doi.org/10.1051/0004-6361/200912495) (cit. p. 29)
- Seward, F. D., Forman, W. R., Giacconi, R., Griffiths, R. E., Harnden, F. R., Jr., Jones, C. & Pye, J. P. (1979). X-rays from Eta Carinae and the surrounding nebula. *The Astrophysical Journal*, 234, L55–L58.
DOI: [10.1086/183108](https://doi.org/10.1086/183108) (cit. p. 22)
- Shenar, T., Sablowski, D. P., Hainich, R., Todt, H., Moffat, A. F. J., Oskinova, L. M., Ramachandran, V., Sana, H., Sander, A. A. C., Schnurr, O., St-Louis, N., Vanbeveren, D., Götberg, Y. & Hamann, W.-R. (2019). The Wolf-Rayet binaries of the nitrogen sequence in the Large Magellanic Cloud: Spectroscopy, orbital analysis, formation, and evolution. *A&A*, 627, A151.
DOI: [10.1051/0004-6361/201935684](https://doi.org/10.1051/0004-6361/201935684) (cit. p. 42)
- Soulain, A., Millour, F., Lopez, B., Matter, A., Lagadec, E., Carbillet, M., Camera, A. L., Lamberts, A., Langlois, M., Milli, J., Avenhaus, H., Magnard, Y., Roux, A., Moulin, T., Carle, M., Sevin, A., Martinez, P., Abe, L. & Ramos, J. (2018). SPHERE view of Wolf-Rayet 104 - Direct detection of the Pinwheel and the link with the nearby star. *A&A*, 618, A108.
DOI: [10.1051/0004-6361/201832817](https://doi.org/10.1051/0004-6361/201832817) (cit. p. 38, 39, 79, 111, 116)
- Spiteri, R. J. & Ruuth, S. J. (2002). A New Class of Optimal High-Order Strong-Stability-Preserving Time Discretization Methods. *SIAM J. Numer. Anal.*, 40(2), 469–491.
DOI: [10.1137/S0036142901389025](https://doi.org/10.1137/S0036142901389025) (cit. p. 82)
- Stevens, I. R. & Pollock, A. M. T. (1994). Stagnation-point flow in colliding-wind binary systems. *Mon Not R Astron Soc*, 269(2), 226–234.
DOI: [10.1093/mnras/269.2.226](https://doi.org/10.1093/mnras/269.2.226) (cit. p. 80, 119)

JOURNAL CITATIONS

- Stevens, I. R., Blondin, J. M. & Pollock, A. M. T. (1992). Colliding winds from early-type stars in binary systems. *The Astrophysical Journal*, *386*, 265–287.
DOI: [10.1086/171013](https://doi.org/10.1086/171013) (cit. p. 25, 31, 81, 119, 128)
- Stone, J. M., Tomida, K., White, C. J. & Felker, K. G. (2020). The Athena++ Adaptive Mesh Refinement Framework: Design and Magnetohydrodynamic Solvers. *ApJS*, *249*(1), 4.
DOI: [10.3847/1538-4365/ab929b](https://doi.org/10.3847/1538-4365/ab929b) (cit. p. 49, 50, 81, 112, 113)
- Thomas, J. D., Richardson, N. D., Eldridge, J. J., Schaefer, G. H., Monnier, J. D., Sana, H., Moffat, A. F. J., Williams, P., Corcoran, M. F., Stevens, I. R., Weigelt, G., Zainol, F. D., Anugu, N., Le Bouquin, J.-B., ten Brummelaar, T., Campos, F., Couperus, A., Davies, C. L., Ennis, J., ... Zurmühl, U. (2021). The orbit and stellar masses of the archetype colliding-wind binary WR 140. *Monthly Notices of the Royal Astronomical Society*, *504*(4), 5221–5230.
DOI: [10.1093/mnras/stab1181](https://doi.org/10.1093/mnras/stab1181) (cit. p. 79, 120)
- Tielens, A. G. G. M., McKee, C. F., Seab, C. G. & Hollenbach, D. J. (1994). The physics of grain-grain collisions and gas-grain sputtering in interstellar shocks. *The Astrophysical Journal*, *431*, 321.
DOI: [10.1086/174488](https://doi.org/10.1086/174488) (cit. p. 18, 89, 116)
- Toro, E. F., Spruce, M. & Speares, W. (1994). Restoration of the contact surface in the HLL-Riemann solver. *Shock Waves*, *4*(1), 25–34.
DOI: [10.1007/BF01414629](https://doi.org/10.1007/BF01414629) (cit. p. 46, 50)
- Townsend, R. H. D. (2009). An Exact Integration Scheme for Radiative Cooling in Hydrodynamical Simulations. *ApJS*, *181*(2), 391–397.
DOI: [10.1088/0067-0049/181/2/391](https://doi.org/10.1088/0067-0049/181/2/391) (cit. p. 59, 69, 70)
- Tuthill, P. G., Monnier, J. D. & Danchi, W. C. (1999). A dusty pinwheel nebula around the massive star WR 104. *Nature*, *398*(6727), 487–489.
DOI: [10.1038/19033](https://doi.org/10.1038/19033) (cit. p. 79, 110)
- Usov, V. V. (1991). Stellar wind collision and dust formation in long-period, heavily interacting Wolf-Rayet binaries. *Monthly Notices of the Royal Astronomical Society*, *252*(1), 49–52.
DOI: [10.1093/mnras/252.1.49](https://doi.org/10.1093/mnras/252.1.49) (cit. p. 25)
- van der Hucht, K. A., Koenigsberger, G. & Eenens, P. R. (1999). Wolf-rayet phenomena in massive stars and starburst galaxies. *Wolf-Rayet Phenomena in Massive Stars and Starburst Galaxies*, *193* (cit. p. 79).

BIBLIOGRAPHY

- van Leer, B. (1979). Towards the ultimate conservative difference scheme. V. A second-order sequel to Godunov's method. *Journal of Computational Physics*, 32(1), 101–136.
DOI: [10.1016/0021-9991\(79\)90145-1](https://doi.org/10.1016/0021-9991(79)90145-1) (cit. p. 46, 50)
- Watson, W. D. & Salpeter, E. E. (1972). On the Abundances of Interstellar Molecules. *The Astrophysical Journal*, 175, 659.
DOI: [10.1086/151587](https://doi.org/10.1086/151587) (cit. p. 19)
- Williams, P. M. (2019). Variable dust emission by WC type Wolf-Rayet stars observed in the NEOWISE-R survey. *Monthly Notices of the Royal Astronomical Society*, 488(1), 1282–1300.
DOI: [10.1093/mnras/stz1784](https://doi.org/10.1093/mnras/stz1784) (cit. p. 40, 42, 79)
- Williams, P. M., Beattie, D. H., Lee, T. J., Stewart, J. M. & Antonopoulou, E. (1978). Condensation of a shell around HD 193793. *Monthly Notices of the Royal Astronomical Society*, 185, 467–472.
DOI: [10.1093/mnras/185.3.467](https://doi.org/10.1093/mnras/185.3.467) (cit. p. 37)
- Williams, P. M., Crowther, P. A. & van der Hucht, K. A. (2015). The spectra of WC9 stars: Evolution and dust formation. *Monthly Notices of the Royal Astronomical Society*, 449(2), 1834–1844.
DOI: [10.1093/mnras/stv409](https://doi.org/10.1093/mnras/stv409) (cit. p. 84, 120)
- Williams, P. M., Marchenko, S. V., Marston, A. P., Moffat, A. F. J., Varricatt, W. P., Dougherty, S. M., Kidger, M. R., Morbidelli, L. & Tapia, M. (2009). Orbitally modulated dust formation by the WC7+O5 colliding-wind binary WR 140. *Monthly Notices of the Royal Astronomical Society*, 395(3), 1749–1767.
DOI: [10.1111/j.1365-2966.2009.14664.x](https://doi.org/10.1111/j.1365-2966.2009.14664.x) (cit. p. 125)
- Williams, P. M. & van der Hucht, K. A. (2000). Spectroscopy of WC9 Wolf-Rayet stars: A search for companions. *Monthly Notices of the Royal Astronomical Society*, 314(1), 23–32.
DOI: [10.1046/j.1365-8711.2000.03332.x](https://doi.org/10.1046/j.1365-8711.2000.03332.x) (cit. p. 38)
- Williams, P. M., van der Hucht, K. A., Pollock, A. M. T., Florkowski, D. R., van der Woerd, H. & Wamsteker, W. M. (1990). Multi-frequency variations of the Wolf-rayet system HD 193793 - I. Infrared, X-ray and radio observations. *Monthly Notices of the Royal Astronomical Society*, 243, 662–684 (cit. p. 79, 110, 111, 120).
- Williams, P. M., van der Hucht, K. A. & Thé, P. S. (1987). Infrared photometry of late-type Wolf-Rayet stars. *Astronomy and Astrophysics*, 182, 91–106 (cit. p. 23, 111).

- Williams, P. M., van der Hucht, K. A., Thé, P. S. & Bouchet, P. (1990). A Dust Shell around the Early Type Wolf-Rayet Star WR:19. *Monthly Notices of the Royal Astronomical Society*, 247, 18P (cit. p. 97).
- Wolfire, M. G., Hollenbach, D., McKee, C. F., Tielens, A. G. G. M. & Bakes, E. L. O. (1995). The Neutral Atomic Phases of the Interstellar Medium. *The Astrophysical Journal*, 443, 152.
- DOI: [10.1086/175510](https://doi.org/10.1086/175510) (cit. p. 20)
- Zhekov, S. A., Gagné, M. & Skinner, S. L. (2022). Chandra revisits WR 48a: Testing colliding wind models in massive binaries. *Monthly Notices of the Royal Astronomical Society*, 510(1), 1278–1288.
- DOI: [10.1093/mnras/stab3469](https://doi.org/10.1093/mnras/stab3469) (cit. p. 42)
- Zhekov, S. A., Tomov, T., Gawronski, M. P., Georgiev, L. N., Borissova, J., Kurtev, R., Gagné, M. & Hajduk, M. (2014). A multiwavelength view on the dusty Wolf-Rayet star WR 48a. *Monthly Notices of the Royal Astronomical Society*, 445(2), 1663–1678.
- DOI: [10.1093/mnras/stu1880](https://doi.org/10.1093/mnras/stu1880) (cit. p. 42)
- Zubko, V. G. (1998). On the physical model of dust around Wolf-Rayet stars. *Monthly Notices of the Royal Astronomical Society*, 295(1), 109–118.
- DOI: [10.1046/j.1365-8711.1998.29511348.x](https://doi.org/10.1046/j.1365-8711.1998.29511348.x) (cit. p. 17, 80, 90)

Software Citations

- Astropy Collaboration, Price-Whelan, A. M., Sipőcz, B. M., Günther, H. M., Lim, P. L., Crawford, S. M., Conseil, S., Shupe, D. L., Craig, M. W., Dencheva, N., Ginsburg, A., VanderPlas, J. T., Bradley, L. D., Pérez-Suárez, D., de Val-Borro, M., Aldcroft, T. L., Cruz, K. L., Robitaille, T. P., Tollerud, E. J., ... Astropy Contributors. (2018, September). *The astropy project: Building an open-science project and status of the v2.0 core package*. arXiv: [1801.02634 \[astro-ph.IM\]](https://arxiv.org/abs/1801.02634).
- DOI: [10.3847/1538-3881/aabc4f](https://doi.org/10.3847/1538-3881/aabc4f). (Cit. p. 135)
- Astropy Collaboration, Robitaille, T. P., Tollerud, E. J., Greenfield, P., Droettboom, M., Bray, E., Aldcroft, T., Davis, M., Ginsburg, A., Price-Whelan, A. M., Kerzendorf, W. E., Conley, A., Crighton, N., Barbary, K., Muna, D., Ferguson, H., Grollier, F., Parikh, M. M., Nair, P. H., ... Streicher, O. (2013, October). *Astropy: A community Python*

BIBLIOGRAPHY

- package for astronomy.* arXiv: 1307.6212 [astro-ph.IM].
DOI: [10.1051/0004-6361/201322068](https://doi.org/10.1051/0004-6361/201322068). (Cit. p. 135)
- Childs, H., Brugger, E., Whitlock, B., Meredith, J., Ahern, S., Pugmire, D., Biagas, K., Miller, M., Harrison, C., Weber, G. H., Krishnan, H., Fogal, T., Sanderson, A., Garth, C., Bethel, E. W., Camp, D., Rübel, O., Durant, M., Favre, J. M. & Navrátil, P. (2012, October). VisIt: An end-user tool for visualizing and analyzing very large data. *High performance Visualization—Enabling extreme-scale scientific insight* (pp. 357–372). (Cit. p. 55).
- Harris, C. R., Millman, K. J., van der Walt, S. J., Gommers, R., Virtanen, P., Cournapeau, D., Wieser, E., Taylor, J., Berg, S., Smith, N. J., Kern, R., Picus, M., Hoyer, S., van Kerkwijk, M. H., Brett, M., Haldane, A., del Río, J. F., Wiebe, M., Peterson, P., ... Oliphant, T. E. (2020). Array programming with NumPy. *Nature*, 585(7825), 357–362.
DOI: [10.1038/s41586-020-2649-2](https://doi.org/10.1038/s41586-020-2649-2) (cit. p. 55, 135)
- Hunter, J. D. (2007). Matplotlib: A 2D graphics environment. *Computing in Science & Engineering*, 9(3), 90–95.
DOI: [10.1109/MCSE.2007.55](https://doi.org/10.1109/MCSE.2007.55) (cit. p. 54, 135)
- Lam, S. K., Pitrou, A. & Seibert, S. (2015). Numba: A llvm-based python jit compiler. *Proceedings of the Second Workshop on the LLVM Compiler Infrastructure in HPC*, 1–6 (cit. p. 55).
- Schroeder, W., Martin, K. & Lorensen, B. (2006). *The visualization Toolkit—An object-oriented approach to 3D graphics* (4th ed.). Kitware, Inc. (Cit. p. 54).
- Stone, J. M., Tomida, K., White, C. J. & Felker, K. G. (2021, January). *PrincetonUniversity/athena-public-version: Athena++ v21.0* (Version 21.0).
DOI: [10.5281/zenodo.4455880](https://doi.org/10.5281/zenodo.4455880). (Cit. p. 135)
- Tange, O. (2021, September). *GNU parallel 20210922 ('vindelev')*.
DOI: [10.5281/zenodo.5523272](https://doi.org/10.5281/zenodo.5523272). (Cit. p. 54, 135)
- The HDF Group. (1997–2022). *Hierarchical data format, version 5*. (Cit. p. 54).
- Tomar, S. (2006). Converting video formats with FFmpeg. *Linux Journal*, 2006(146), 10 (cit. p. 55).
- Van Rossum, G. & Drake, F. L. (2009). *Python 3 reference manual*. CreateSpace. (Cit. p. 54, 135).
- Williams, T., Kelley, C. & many others. (2020, July). Gnuplot 5.4: An interactive plotting program. (Cit. p. 55).

OTHER CITATIONS

Other Citations

Grete, P., Glines, F. W. & O'Shea, B. W. (2020, July 15). *K-Athena: A performance portable structured grid finite volume magnetohydrodynamics code*. arXiv: [1905.04341 \[astro-ph, physics:physics\]](https://arxiv.org/abs/1905.04341). Retrieved September 28, 2020, from <http://arxiv.org/abs/1905.04341>. (Cit. p. 51)

Pittard, J. M. (1999). *X-ray emission from colliding stellar winds: Theoretical modelling and observations*. (Doctoral dissertation). University of Birmingham. (Cit. p. 23).